A numerically efficient computational model of a flapping micro aerial vehicle based on Hamiltonian geometric reductions

Pandža, Viktor

Doctoral thesis / Disertacija

2022

Degree Grantor / Ustanova koja je dodijelila akademski / stručni stupanj: **University of Zagreb, Faculty of Mechanical Engineering and Naval Architecture / Sveučilište u Zagrebu, Fakultet strojarstva i brodogradnje**

Permanent link / Trajna poveznica: https://urn.nsk.hr/urn:nbn:hr:235:271648

Rights / Prava: In copyright/Zaštićeno autorskim pravom.

Download date / Datum preuzimanja: **2024-05-08**

University of Zagreb

FACULTY OF MECHANICAL ENGINEERING AND NAVAL ARCHITECTURE

Viktor Pandža

A numerically efficient computational model of a flapping micro aerial vehicle based on Hamiltonian geometric reductions

DOCTORAL THESIS

Zagreb, 2022

Sveučilište u Zagrebu

FAKULTET STROJARSTVA I BRODOGRADNJE

Viktor Pandža

Numerički efikasan računalni model male mahokrilne letjelice temeljen na Hamiltonovim geometrijskim redukcijama

DOKTORSKI RAD

Zagreb, 2022

University of Zagreb

FACULTY OF MECHANICAL ENGINEERING AND NAVAL ARCHITECTURE

Viktor Pandža

A numerically efficient computational model of a flapping micro aerial vehicle based on Hamiltonian geometric reductions

DOCTORAL THESIS

Supervisor:

prof. dr. sc. Zdravko Terze

Zagreb, 2022

Sveučilište u Zagrebu

FAKULTET STROJARSTVA I BRODOGRADNJE

Viktor Pandža

Numerički efikasan računalni model male mahokrilne letjelice temeljen na Hamiltonovim geometrijskim redukcijama

DOKTORSKI RAD

Mentor:
prof. dr. sc. Zdravko Terze
Zagreb, 2022

Bibliographic data

Abstract

Insect flight capabilities provide fascination for humans and fuel aspirations for development and manufacturing of insect-type flapping wing aerial vehicles. However, complex underlying aerodynamic phenomena limit our abilities in understanding insect flight and producing aerial vehicle exploiting same phenomena. To this end, a novel mid-fidelity approach to insect-type flapping vehicles modeling is proposed. Computational model includes Helmholtz-Hodge decompositon of fluid velocity into curl-free and divergence-free parts. Coupled multibody-fluid system equations of motion are derived, including added inertia effects of the environmental fluid and viscous effects arising as an additional aerodynamic load on a multibody system. Curl-free vector field is utilized to accurately model added inertia effects, while expressing coupled system dynamics by using multibody system variables only, after employing symplectic reduction of the coupled multibody-fluid system. On the other hand, unsteady viscous effects included in the divergence-free vector field are modeled by a wake of irrotational point vortices, shed from both leading (important for insect-type flapping flight) and trailing edges of the flapping wing. A proposed computational model is evaluated on two numerical examples involving insect-type flapping flight. The first test case involves standstill hovering of fruit fly in Earth atmospheric environment, propelled by flapping pattern characterized with smooth flapping angle functions. Second test case involves insect-type flapping wing aerial vehicle performing hovering in Mars atmospheric environment, with flapping pattern input in discrete form, resulting from optimization algorithm. It is concluded from results analysis that the proposed computational model exhibited near real time properties with high load prediction accuracy.

Keywords: Flapping wing aerial vehicle; Insect-type flapping; Symplectic reduction; Added inertia; Vortex wake; Coupled multibody-fluid system; Flapping flight on Mars;

Prošireni sažetak

Let insekata predstavlja inspiraciju za istraživanje u tehničkim i prirodnim znanostima, zbog njihovih izvrsnih performansi letenja, koje se temelje na naglašenom korištenju nestacionarnih 'fluid-solid' utjecaja. Mahokrila insektnog tipa omogućuju energetski efikasan let i brze manevre, zadržavajući male dimenzije te predstavljajući letne performanse s kojima se ne mogu usporediti performanse konstruiranih letjelica (tek su nedavno dizajnirane prve letjelice koje u određenoj mjeri oponašaju let insekta). Razlog tomu jest složena nestacionarna aerodinamika karakteristična za let insekata koja se počela razumijevati tek u protekla tri desetljeća. Između ostalog, otkriveno je da insekti koriste vrtlog otpušten s napadnog ruba krila kako bi dodatno povećali uzgon u usporedbi s istim krilom pri istom napadnom kutu u stacionarnom strujanju bez vrtloga.

Fokus istraživača u posljednja dva desetljaća usmjeren je na razvoj i izradu mahokrilne letjelice koja bi koristila iste nestacionarne aerodinamičke fenomene karakteristične za let insekata. Složenost nestacionarnih i izrazito nelinearnih aerodinamičkih fenomena otežava zadaću konstruiranja i optimiranja takve letjelice bez odgovarajućih računalnih alata. Zbog visokih frekvencija mahanja i velike amplitude rotacije krila karakterističnih za let insekata računalni modeli spregnutih zadaća temeljeni na metodi konačnih volumena za modeliranje fluida i posebnih (odvojenih) numeričkih rješavača dinamike uronjenog kinematičkog lanca pokazuju neoptimalne performanse i mogućnost pojava računalnih nestabilnosti. Osim toga, računalno vrijeme potrebno za njihovo izvršavanje čini takve pristupe modeliranja neupotrebljivima unutar konstrukcijskih petlji te unutar petlji za optimalno upravljanje. Iz tog razloga javlja se potreba za računalnim modelom mahokrilne letjelice insektnog tipa koji bi omogućio pouzdano modeliranje signifikantnih aerodinamičkih fenomena uz zadržavanje računalne efikasnosti koja omogućuje primjenu unutar konstrukcijskih petlji te unutar petlji optimalnog upravljanja.

U tu svrhu spregnuti sustav krilo-fluid promatra se iz perspektive geometrijske mehanike koja omogućava redukcije spregnutog modela na zajedničkoj mognostrukosti, odnosno

Lievoj grupi diskretnog mehaničkog sustava i ambijentalnog fluida. Brzina fluida se dekomponira u vektorsko polje bez vrtložnosti te vektorsko polje bez divergencije korištenjem Helmholtz-Hodge dekompozicije. Značajke vektorskog polja bez vrtložnosti se zatim koriste pri simplektičkoj redukciji multi-fizikalnog sustava za modeliranje dodane inercije krila uronjenog u fluid - važan fenomen za mahokrila insektnog tipa zbog velikih vrijednosti ubrzanja i složene kinematike krila insektnog tipa. Vektorsko polje bez divergencije koristi se za modeliranje viskoznih utjecaja vrtložnim tragom.

I. Izvod jednadžbi gibanja spregnutog sustava

Za potrebe izvoda jednadžbi gibanja spregnutog sustava, konfiguracijski prostori diskretnog sustava više tijela te idealnog fluida opisani su koristeći matematičke formulacije na Lievim grupama polazeći od k tijela koji zajedno s fluidom pripadaju otvorenom Euklidskom prostoru $\mathcal{M}$. Pritom diskretni sustav pripada uniji individualnih domena krutih tijela, tj. domena diskretnog sustava tijela može se opisati kao $\mathcal{B} = \bigcup_{i=1}^{k} \mathcal{B}_i \subset \mathcal{M}$. Ako se osim toga domena fluida označi s $\mathcal{F}$, domena spregnutog sustava može se opisati kao $\mathcal{M} = \mathcal{B} \bigcup \mathcal{F} = \bigcup_{i=1}^{k} \mathcal{B}_i \bigcup \mathcal{F}$.

Konfiguracijski prostor spregnutog sustava $\mathcal{Q}$ može se definirati kao skup svih dovoljno glatkih preslikavanja $\mathcal{M} \to \mathcal{M}$, a sastoji se od konfiguracijskog prostora diskretnog sustava više tijela $\mathcal{Q}_\mathcal{B}$ te konfiguracijskog prostora idealnog fluida $\mathcal{Q}_\mathcal{F}$.

Konfiguracijski prostor sustava k krutih tijela povezanih kinematičkim ograničenjima predstavlja Lievu grupu $G_\mathcal{B} = \prod_{i=1}^{k} G_{\mathcal{B}_i} = \mathbb{R}^3 \times SO(3) \times \cdots \times \mathbb{R}^3 \times SO(3)$ s elementima $q_\mathcal{B} = (\boldsymbol{x_1}, \boldsymbol{R_1}, \ldots, \boldsymbol{x_k}, \boldsymbol{R_k}) \in G_\mathcal{B}$. Pritom $\boldsymbol{x_i} \in \mathbb{R}^3$ odgovara pomaku središta mase tijela i, dok $\boldsymbol{R_i} \in SO(3)$ predstavlja matricu rotacije u obliku 3×3 ortogonalne matrice, koja pripada Lievoj grupi specijalnih ortogonalnih matrica. Lieva algebra grupe $G_\mathcal{B}$ može se definirati kao $g_\mathcal{B} = \prod_{i=1}^{k} g_{\mathcal{B}_i} = \mathbb{R}^3 \times so(3) \times \cdots \times \mathbb{R}^3 \times so(3)$ s elementima $v = (\boldsymbol{v_1}, \tilde{\boldsymbol{\omega_1}}, \ldots, \boldsymbol{v_k}, \tilde{\boldsymbol{\omega_k}}) \in g_\mathcal{B}$, pri čemu $\boldsymbol{v_i} \in \mathbb{R}^3$ predstavlja vektor brzine središta mase tijela i iskazan u inercijskom koordinatnom sustavu, dok $\tilde{\boldsymbol{\omega_i}} \in so(3)$ predstavlja kutnu brzinu tijela i iskazanu u koordinatnom sustavu vezanom za tijelo, a u obliku antisimetrične matrice.

S druge strane, konfiguracijski prostor idealnog fluida može se definirati kao Lieva grupa u obliku difeomorfizma s očuvanjem volumena fluida $\text{Diff}_{\text{vol}}(\mathcal{F})$. Preslikavanje povezano s momentnom mapom $J_\mathcal{F}$ je sačuvano (invarijantno) s obzirom na djelovanje

$\text{Diff}_{\text{vol}}(\mathcal{F})$ na konfiguracijski prostor $\mathcal{Q}$ pri čemu je i Lagrangian fluida invarijantan na djelovanje Lieve grupe $\text{Diff}_{\text{vol}}(\mathcal{F})$ (posljedica simetrije 'preimenovanja čestica'), odnosno konačnim rezultatom postiže se simplektička redukcija spregnutog multi-fizikalnog 'fluid-solid' sustava. U reduciranoj konačnoj formulaciji ukupna dinamika sustava izražava se na kotangentnom svežnju diskretnog sustava uronjenih tijela $T^*G_{\mathcal{B}}$ dok eksplicitne fluidne varijable iščezavaju iz spregnutog reduciranog modela (dinamičko djelovanje ambijentalnog fluida na gibanje diskretnog sustava izražava se utjecajem dodane inercije uronjenih tijela u gibanju). Osim fluidnog utjecaja dodane inercije, viskozni utjecaji strujanja fluida modeliraju se odvojeno te se uključuju u jednadžbe gibanja kao dodatni vektor opterećenja.

Jednadžbe gibanja spregnutog sustava izvedene su u obliku diferencijalno-algebarskog sustava jednadžbi indeksa 1, pri čemu vektor opterećenja uključuje konvencionalno vanjsko opterećenje u obliku sila i momenata koji djeluju na tijela, vektor "opterećenja" uslijed izvoda jednadžbi u rotirajućem koordinatnom sustavu, vektor "opterećenja" uslijed promjenjivosti matrice dodane inercije u vremenu te vektor aerodinamičkog opterećenja uslijed viskoznih utjecaja obuhvaćenih modeliranjem vrtložnog traga. Kinematička rekonstrukcija orijentacije tijela izračunava se numeričkim algoritmom integracije u vremenskoj domeni sintetiziranim izravno na odgovarajućoj Lievoj grupi i pripadajućoj Lievoj algebri.

II. Računanje dodane inercije i viskoznih utjecaja

Kako bi se izračunao fluidni utjecaj dodane inercije na tijela uronjena u ambijentalan fluid, kinetička energija fluida može se zapisati u ovisnosti o potencijalu brzine idealnog nestlačivog fluida ϕ, pri čemu vrijedi da je $\Delta\phi = 0$. U izrazu za izračunavanje kinetičke energije, integracija na domeni fluida $\mathcal{F}$ zamjenjuje se integracijom po površini diskretnog sustava više tijela $\partial\mathcal{B} = \sum_{i=1}^{k}\partial\mathcal{B}_i$ korištenjem poopćenog Stokesovog teorema.

Daljnjom procedurom potencijal fluida može se rastaviti na komponente potencijala vezane uz translacijsku i kutnu brzinu krutih tijela (šest komponenti za trodimenzionalni problem ili tri komponente za dvodimenzionalnu zadaću) te se matrice dodane inercije mogu izraziti u ovisnosti o komponentama potencijala te njihovim derivacijama u smjeru normale na površinu tijela. Također se može pokazati da svaka komponenta potencijala zadovoljava Laplaceovu jednadžbu. Uz primjenu rubnog uvjeta tangencijalnosti brzine fluida na konturu tijela, zadaća računanja matrica dodane inercije može se zapisati kao rubna zadaća (*eng. boundary value problem*). Za rješavanje formulirane rubne zadaće

koristi se kolokacijska metoda rubnih elementata s analitičkim rješenjima za singularne integrale. Primjenjena metoda je verificirana na geometrijskim oblicima s poznatim analitičkim rješenjem.

Kako je već ranije opisano, osim matrice dodane inercije važno je modelirati i viskozne utjecaje, koji se u ovom slučaju računaju modelom vrtložnog traga. Aeroprofili mahokrila su općenito izrazito tanki, s debljinom aeroprofila manjom of 5% tetive krila. Stoga se pretpostavlja besoknačno tanak aeroprofil, dok se u daljnjem istraživanju u slučaju potrebe lako može uključiti i diskretizacija pravog oblika presjeka krila. Aeroprofil se diskretizira pomoću vrtložnih elemenata, koji se sastoje od točkastog vrtloga pričvršćenog na $\frac{1}{4}$ elementa i koji se kreće zajedno s elementom te kolokacijske točke na $\frac{3}{4}$ vrtložnog elementa u kojoj se primjenjuju isti rubni uvjeti nepropusnosti površine kao i za računanje dodane inercije.

Kako je već spomenuto, točkasti vrtlozi se otpuštaju i s napadnog i s izlaznog ruba. Prednji vrtlog se ne otpušta u svakom vremenskom koraku, već samo kada je zadovoljen uvjet otpuštanja na temelju uvedenog kriterija. S druge strane, vrtlog s izlaznog ruba mahokrila otpušta se u svakom vremenskom koraku i to na način da su zadovoljeni uvjeti nepropusnosti u svim kolokacijskim točkama, kao i Kelvinov cirkulacijski teorem koji definira konstantni iznos ukupne cirkulacije (zbroj iznosa cirkulacije za pričvršćene vrtloge te vrtloge u vrtložnom tragu) u svakom vremenskom koraku.

Točkasti vrtlozi u vrtložnom tragu smatraju se "slobodnima" i bez inercije. tj. kreću se u skladu s brzinom fluida na položaju vrtloga, koja se računa kao inducirana brzina od strane svih "pričvršćenih" vrtloga te vrtloga iz vrtložnog traga.

Aerodinamičko opterećnje uslijed vrtložnog traga se u svakom vremenskom trenutku računa pomoću Kutta-Joukowski teorema, pri čemu se odgovarajuća sila računa za svaki vrtložni element zasebno.

III. Numerički eksperimenti i zaključak

Provedena su dva numerička eksperimenta na letjelicama s morfologijom vinske mušice (lat. *Drosophila melanogaster*), zbog dostupnih eksperimentalnih rezultata te aerodinamičkih modela s validiranim parametrima za primjer vinske mušice u određenom rasponu Reynoldsovog broja. Prvi numerički primjer uključuje modeliranje nepomičnog lebdenja vinske mušice na Zemlji s glatkim funkcijama koje opisuju kuteve mahanja tijekom jednog

ciklusa. Funkcije kuteva preuzete su iz literature gdje su određene na temelju eksperimenata s krilom koje morfološki odgovara krilu promatranog biološkog sustava. Drugi numerički primjer uključuje letjelicu s krilima koja morfološki odgovaraju krilima *Drosophila melanogaster*, uz povećane geometrijske karakteristike u skladu sa zakonitostima energetski efikasne fizike leta u bitno rjeđoj atmosferi planete Mars. Faktor skaliranja krila te funkcije kuteva temelje se na rezultatima prethodnog istraživanja koje je uključivalo optimiranje letjelice za nepomično lebdenje u atmosferi Marsa te su u ovom slučaju implementirane izravno u diskretnom obliku.

Rezultati oba numerička eksperimenta uspoređeni su s rezultatima kvazistacionarnog aerodinamičkog modela s eksperimentalno validiranim parametrima te su ostvarene izvrsne korelacije s vrijednostima sila uzgona i otpora, čime je uspješno validiran predloženi računalni model.

Na temelju ostvarenih rezultata doneseni su glavni zaključci disertacije:

- Aerodinamika mahorkila insektnog tipa može se pouzdano i efikasno modelirati korištenjem računalnog modela temeljenog na dekompoziciji brzine fluida na vektorsko polje bez vrtložnosti (koje se koristi za modeliranje fluidnog utjecaja dodane inercije) te vektorsko polje bez divergencije, koje se koristi za modeliranje viskoznih utjecaja vrtložnim tragom. U skladu s prethodnim zaključcima iz literature, potvrđeno je da zanemarivanje utjecaja rubnog sloja ne vodi do značajnih gubitaka na točnosti.

- Predloženi računalni model izvršava se na računalu u gotovo pa stvarnom vremenu s pouzdanim računanjem aerodinamičkog opterećenja na mahokrilu. Pritom predloženi računalni model ne zahtijeva određivanje nikakvih parametara modela na temelju prijašnjih rezultata ili iskustva, za razliku od često korištenog numerički efikasnog kvazistacionarnog aerodinamičkog modela. Ova svojstva čine predloženi računalni model prikladnim za korištenje unutar konstrukcijskih petlji te unutar petlji optimalnog upravljanja.

- Ispravno izvođenje jednadžbi gibanja spregnutog sustava koji se sastoji od sustava više tijela te ambijentalnog fluida rezultira dodatnim članom u 'aerodinamičkom opterećenju' zbog promjenjivosti dodane inercije u vremenu, za razliku od konstantne matrice inercije krutog tijela. Ovaj član se često greškom ispušta i ne uključuje u analizu u dostupnoj literaturi.

- Utjecaji dodane inercije s modeliranjem međuzavisnosti između krutih tijela u kinematičkom lancu, točne geometrije tijela te vremenske zavisnosti matrice dodane inercije mogu se pouzdano modelirati preko skupa Laplaceovih rubnih zadaća. Kolokacijska metoda rubnih elemenata validirana je za rješavanje rezultirajućih rubnih problema, računanjem dodane inercije za jednostavne geometrijske oblike, za koje su poznata analitička rješenja.

- Viskozni utjecaji fluida na mahokrilo mogu se pouzdano i efikasno računati korištenjem predložene metode modeliranja vrtložnog traga, temeljene na metodi s vrtložnim elementima. Metoda je prilagođena za primjenu na mahokrilne letjelice insektnog tipa dodavanjem modela otpuštanja i razvoja vrtloga s napadnog ruba krila.

- Numerički eksperimenti u značajno različitim atmosferama Zemlje i Marsa upućuju da se predložena metoda može koristiti za modeliranje mahokrilnih letjelica insektnog tipa u nepoznatim okruženjima, bez izmjena u parametrima modela.

Zaključno, najvažniji ostvareni znanstveni doprinosi su:

- Razvoj novog računalnog modela dinamike leta mahokrilne letjelice insektnog tipa koji se može koristiti za pouzdano i efikasno modeliranje najvažnijih složenih aerodinamičkih fenomena fizike leta mahokrilnih sustava, temeljenog na Hamiltonovim geometrijskim redukcijama na zajedničkoj mnogostrukosti (Lievoj grupi) spregnutog sustava 'fluid-solid', uz dodatni numerički model opisivanja značajnih viskoznih utjecaja mahokrila u ambijentalnom fluidu.

- Razvoj i numerička implementacija modela za izračunavanje fluidnog utjecaja dodane inercije uronjenog mahokrila pri gibanju u ambijentalnom fluidu, temeljenog na simplektičkoj redukciji spregnutog sustava te numeričkoj metodi rubnih elemenata.

- Prilagodba konvencionalne nestacionarne metode vrtložnih elemenata za primjenu pri modeliranju mahokrila insektnog tipa, razvojem i implementacijom numeričkog modela otpuštanja vrtloga s napadnog i izlaznog ruba krila.

- Sinteza numerički efikasnog računalnog okruženja koje se može koristiti za multifizikalno optimiranje dinamike leta mahokrilne letjelice u različitim atmosferskim uvjetima, kao što su odabrani uvjeti fizike leta zemaljskog okruženja, ali također i naročito zahtjevni uvjeti leta u atmosferskim uvjetima planete Mars.

Ključne riječi: Mahokrilna letjelica; Mahokrilo insektnog tipa; Simplektička redukcija; Fluidni utjecaj dodane inercije; Vrtložni trag; Spregnut sustav dinamike fluida i sustava više tijela; Mahokrilni let na Marsu;

Contents

List of Figures

List of Tables

Nomenclature

Roman letters

$\boldsymbol{\lambda}$ Vector of Lagrange multipliers [-]

$\boldsymbol{A}$ Matrix on the left-hand side of boundary element method final equations [-]

$\boldsymbol{B}$ Matrix on the right-hand side of boundary element method final equations [-]

$\boldsymbol{C}$ Constraint Jacobian matrix [-]

$\boldsymbol{D}$ Vortex influence matrix [1/m]

$\boldsymbol{F}$ Force [N]

$\boldsymbol{J_i'}$ Inertia matrix of ith rigid body expressed in body-fixed coordinate frame [-]

$\boldsymbol{l}$ Angular momentum [kgm^2/s]

$\boldsymbol{M_B}$ Inertia block matrix of a multibody system [-]

$\boldsymbol{M_F}$ Added inertia block matrix [-]

$\boldsymbol{M_{ellipse}}$ Added inertia matrix for ellipse [-]

$\boldsymbol{M_{ij}^f}$ Block matrix representing added inertia contribution of body i on body j [-]

$\boldsymbol{M_{rectangle}}$ Added inertia matrix for rectangle [-]

$\boldsymbol{M_{unit\_circle}}$ Added inertia matrix for unit circle [-]

$\boldsymbol{M_{unit\_square}}$ Added inertia matrix for unit square [-]

$\boldsymbol{M}$ Overall inertia block matrix of a multibody system submerged in fluid [-]

$\boldsymbol{n_i}$ Unit normal pointing inward to ith body [-]

$\boldsymbol{p}$ Linear momentum [kgm/s]

$\boldsymbol{Q_{AM}}$ "Load" due to time-changing nature of added inertia [-]

$\boldsymbol{Q_{ext}}$ General external load acting on bodies [-]

$\boldsymbol{Q_{spatial}}$ Total applied load [-]

$\boldsymbol{Q_{vel}}$ "Load" resulting from expressing equations in rotating frame [-]

$\boldsymbol{Q_{vort}}$ Aerodynamic load due to vorticity effects [-]

$\boldsymbol{r_i^v}$ Distance vector from vortex center point to position where velocity is induced [m]

$\boldsymbol{r_i}$ Position of ith particle [m]

$\boldsymbol{R}$ Rotation matrix [-]

$\boldsymbol{T}$ Torque [Nm]

$\boldsymbol{u}$ Fluid velocity vector [m/s]

$\boldsymbol{v_i^{vor}}$ Overall velocity of ith vortex [m/s]

$\boldsymbol{v_b}$ Velocity in body-fixed reference frame [m/s]

$\boldsymbol{v_c}$ Velocity of mass center [m/s]

$\boldsymbol{v_{in}}$ Vortex-induced velocity [m/s]

$\boldsymbol{V}$ Lagrangian (material) velocity [m/s]

$\boldsymbol{v}$ Eulerian (spatial) velocity [m/s]

$\hat{x}_0$ Pitching axis position (in chord lengths) [-]

$\mathbb{R}^n$ n-dimensional Euclidean space [-]

$\bar{c}$ Mean chord length [m]

$\mathrm{Diff}_{\mathrm{vol}}(\mathcal{F})$ Group of volume-preserving diffeomorphisms [-]

Re Reynolds number [-]

b Wing thickness [m]

C_R Rotational force coefficient [-]

C_{DT} Translational drag coefficient [-]

C_{LT} Translational lift coefficient [-]

D^{KJ} Vortex wake-induced drag force [N]

D_A Added mass drag [N]

D_V Drag due to vorticity effects [N]

D_{QS} Drag force calculated by quasi steady aerodynamic model [N]

E_{rel} Relative error of numerically calculated value [-]

f Frequency [Hz]

F_A Added mass force [N]

F_R Rotational force [N]

F_{TD} Translational drag force [N]

F_{TL} Translational lift force [N]

G Lie group [-]

g Lie algebra [-]

G_L Green's function for Laplace problem [-]

$G_{\mathcal{B}_i}$ Lie group of a ith rigid body configuration space [-]

$g_{\mathcal{B}_i}$ Lie algebra of $G_{\mathcal{B}_i}$ [-]

$G_{\mathcal{B}}$ Lie group of a multibody system configuration space [-]

$g_{\mathcal{B}}$ Lie algebra of $G_{\mathcal{B}}$ [-]

g_{Mars} Gravitational acceleration on Mars [m/s^2]

I_w Wing inertia matrix [kgm^2]

J Boundary element Jacobian [-]

$J_{\mathcal{F}}$ Momentum map associated with action of $\text{Diff}_{\text{vol}}(\mathcal{F})$ [-]

K_α Stroking function shape parameter [-]

K_β Pitching function shape parameter [-]

L^{KJ} Vortex wake-induced lift force [N]

L_A Added mass lift [N]

L_V Lift due to vorticity effects [N]

L_{QS} Lift force calculated by quasi steady aerodynamic model [N]

L_{ref} Reference length [m]

m Mass [kg]

m_b Main body mass [kg]

m_w Wing mass [kg]

Q Generalized force [-]

q Generalized coordinate [-]

R Wing length [m]

S Multibody system state space [-]

S_i State space of ith rigid body [-]

$SO(3)$ Special orthogonal Lie group [-]

$so(3)$ Lie algebra of $SO(3)$ [-]

T Flapping period [-]

T Kinetic energy [J]

$T_{\mathcal{F}}$ Kinetic energy of the fluid [J]

T_A Added mass torque [Nm]

$T_{\mathcal{B}_i}$ Kinetic energy of ith body [J]

V Potential energy [J]

v_{ref} Reference velocity [m/s]

Greek letters

α Stroking angle [-]

α_m Stroking anfle amplitude [-]

β Pitching angle [-]

β_a Average pitching value offset [-]

β_m Pitching angle amplitude [-]

β_p Pitching phase offset [-]

$\boldsymbol{\eta_i}$ Rotational fluid velocity potential vector related to ith body [m^2]

$\boldsymbol{\Omega}$ Angular velocity in spatial reference frame [1/s]

$\boldsymbol{\omega}$ Angular velocity in body-fixed reference frame [1/s]

$\boldsymbol{\Pi}$ Total impulse of a coupled system [-]

$\boldsymbol{\theta_i}$ Translational fluid velocity potential vector related to ith body [m]

Δt Time step size [s]

δ Angle of attack [-]

Γ Circulation [m^2/s]

γ Deviation angle [-]

Γ_{LEV} Leading edge vortex circulation [m^2/s]

Γ_{TEV} Trailing edge vortex circulation [m^2/s]

μ Dynamic viscosity [kg/ms]

μ_{Mars} Mars atmoshpere dynamic viscosity [kg/ms]

ϕ Fluid velocity potential [m^2/s]

ψ_1 First shape function [-]

ψ_2 Second shape function [-]

ψ_v Stream function [m^2/s]

$\rho_{\mathcal{F}}$ Fluid density [kg/m^3]

ρ_{Mars} Mars atmospheric density [kg/m^3]

Callygraphy letters

$\mathcal{B}$ Rigid body domain [-]

$\mathcal{F}$ Ideal fluid domain [-]

$\mathcal{L}$ Lagrangian [J]

$\mathcal{L}_S$ Lagrangian of the coupled mutibody-fluid system [J]

$\mathcal{M}$ Manifold [-]

$\mathcal{Q}_{\mathcal{B}}$ Rigid body configuration space [-]

$\mathcal{Q}_{\mathcal{F}}$ Configuration space of ideal fluid [-]

$\mathcal{TM}$ Tangent bundle [-]

$\mathcal{T}_P\mathcal{M}$ Tangent space to manifold $\mathcal{M}$ in point P [-]

CHAPTER 1

Introduction

1.1 Motivation

Insect flight is a source of fascination for researchers in both aerospace and zoology fields. Their unmatched flight performance has generated an ever-growing interest in insect flight research. Their flapping wings enable them to efficiently hover, to perform relatively quiet quick agile maneuvers, while keeping a small size - the capabilities not nearly matched by any man-made aerial vehicle. Despite the fact that their capabilities are known for a very long time, one of the pioneering papers in unraveling insect flight physics [1] emerged relatively recently, starting with a famous quote "*Insects cannot fly, according to the conventional laws of aerodynamics...*". The paper includes description of a very important phenomenon in insect-type flapping flight - the leading edge vortex (LEV), discovered by experimenting with hawkmoth hovering in wind tunnel. It is found that the investigated hawkmoth uses intense LEV to generate extra lift, the phenomenon unknown to that time, and required for description of surprisingly high lift force values.

Since then, there is a persistent effort from many research groups to develop a flapping wing aerial vehicle (FWAV), utilizing the same aerodynamic phenomena pertinent to insect flight. However, the highly complex and unsteady aerodynamic phenomena involved significantly complicate the modeling and development of such vehicles. Complex, unsteady and highly nonlinear (and therefore sometimes counter-intuitive) phenomena render design of such aerial vehicles by hand almost impossible. On the other hand, high flapping frequencies and large amplitudes of wing rotation characteristic for insect flight render the fluid-structure modeling approaches based on conventional CFD methods, involving finite volume discretization, unstable and highly inefficient. In addition to this, high computational cost characteristic for finite volume-based CFD methods renders them

1

inapplicable for utilization within design optimization or optimal control loops [2]. This naturally leads to the requirement for an efficient and reliable (mid-fidelity) computational model of a flapping wing aerial vehicle, capable of capturing most important aerodynamic phenomena, while still being efficient enough to be used within both optimal control and design optimization loops.

1.2 Literature review

As already described, there are significant efforts invested in insect flight research, both from the fundamental perspective, trying to describe aerodynamic phenomena utilized within insect flight and from the application perspective, trying to develop computational tools for insect-type flapping aerial vehicle development.

The effect of petiolate wings on the LEV is investigated in [3] and it is shown that wing petiolation has positive effects on LEV size and intensity, which may be the reason why many insect species have petiolate wings. On the other hand, in [4] it is argued that it is better to consider LEV as a mechanism of preventing stall at high angles of attack than to consider it as a lift increasing mechanism. It can be concluded that the modeling and complete understanding of the LEV effects on insect flight is still an open topic.

In order to better understand underlying physical phenomena, it is crucial to develop a model that is capable of representing both the multibody system of the flapping wing aerial vehicle and the fluid flow around its wings with sufficient accuracy. Lift and drag coefficients and vortex distribution for flapping wing in 2D were analyzed in [5] using a CFD software FLUENT. An in-house developed CFD tool based on finite volumes method was used in [6] to model flapping wing aerial vehicle and it has been verified by experiment that the computational procedure can be used for a quantitative prediction of aerodynamic force production. Additionally, different in-house fluid-structure interaction (FSI) code based on coupling between solver for Navier-Stokes equations and structural solver was used in [7] to analyze wing flapping for different wing flexibilities and flapping frequencies.

Reduced-order model of the MAV was developed in [8] based on measured wing deformation. The importance of using a morphologically accurate insect-wing cross-section in aerodynamic simulations was studied in [9]. The importance of accurately describing added masses as well as importance of using 3D model are assessed in [10] by calculating added

masses of flapping wings for 2D and 3D case, and compared it with total aerodynamic force calculated by CFD method.

In order to obtain more numerically efficient MAV model, a number of researchers choose a different approach to fluid modeling. One of the most often used approaches is unsteady vortex-lattice (UVL) method. In [11] results of unsteady vortex-lattice method with different load estimation techniques were analyzed and it is concluded that none of the methods investigated represent flow physics successfully in all cases. However, this does not mean that the method is useless for flapping wing aerial vehicle modeling, especially if tailored for specific application, instead of using a general purpose method. For example, an UVL method was extended in [12] for simulating dynamics of insect flapping wing by adding models taking into account leading-edge suction and vortex-core growth. Also, a co-simulation strategy for flapping wing aerial vehicle in hovering flight, consisting of multiple flexible bodies on structural side of simulation, coupled with UVL method to calculate aerodynamic forces was developed in [13]. A numerically efficient computational framework for modeling flapping wing aerial vehicle based on multibody code coupled with unsteady vortex-lattice fluid model is developed in [14]. A different approach was taken in [15], where immersed boundary-lattice Boltzmann method was used to analyze aerodynamic performance of a butterfly-like wing flapping. One of the challenges in modeling flow around insects' flapping wings is description of LEV, and a closed form solution for a vortex shedding from a revolving plate at 90° angle of attack is derived in [16] with the goal of using that technique in flapping wing aerial vehicle modeling.

The main application of accurate and numerically efficient flapping wing aerial vehicle computational model is design optimization, since it is almost impossible to approach optimal design by hand-tuning flapping mechanism, mainly due to the fluid flow complexity. The results of using an inviscid lattice method and Navier-Stokes solver with accurate representation of flapping wing geometry were compared in [17] and it is concluded that the lattice method in many cases provides accurate prediction od aerodynamic forces and can therefore be used to aid design optimization. In [18] UVL method was used to optimize design of actively morphing flapping wings in forward flight with a goal of maximizing propulsive efficiency under lift and thrust constraints. Similar methodology was used in [19] to obtain maximum efficiency defined as ratio of propulsive power and aerodynamic

power. The method was also used for shape optimization of the flapping wings in [20]. In [21] UVL method coupled with plate finite element model was used to perform both shape and structural optimization of plate-like flapping wing. Unsteady blade element theory model for flapping wing aerodynamics modeling, developed in [22], was used in [23] to design and analyze six-bar flapping wing mechanism. On the other hand, wing optimization of a flapping MAV was performed in [24], by using a computational tool based on coupling between fluid and solid model described by finite volumes and finite elements.

In addition to UVL-based aerodynamic models, the quasi steady (QS) models, characterized by low computational costs, have also been extensively used for flapping wing applications. The examples of QS aerodynamic model utilization for flapping wing kinematics optimization for flight on Earth and Mars can be found in [25, 26]. Most of the QS models are based on model presented in [27, 28], developed by experimenting on a scaled model of fruit fly wing. The QS models provide a rapid estimation of aerodynamic load, but are not well suited to describe highly unsteady aerodynamic phenomena pertinent to flapping flight, and can therefore be used only to simulate flight regimes for which experiments were conducted (and for which the model parameters were fitted).

In the field of underwater bio-inspired robots, the geometric approach has proven to be an effective tool for obtaining numerically efficient FSI models. The two-stage geometric reduction on fluid-solid system was used in [29] to obtain boundary value model of multibody system for an ideal fluid with zero circulation. In [30], the similar reduced fluid-solid system was appended with vortex shedding mechanism on a trailing edge of free pitching hydrofoil with internal rotor. The various benefits of using geometric approach to modeling of locomotion dynamics of different animals are described in [31]. Although some of the tools for analyzing multibody system dynamics of bio-inspired robots developed in that paper are also suggested for flying animals, the real computational framework for geometric modeling of insect flying has yet to be developed.

1.3 Hypothesis and research objectives

The goal of this research was to develop a computational model of the flapping wing micro aerial vehicle (MAV), mimicking insect flight, based on the geometric reductions on manifolds and Lie groups of the fluid-solid system supplemented with vortex shedding

mechanism. The purpose of the model is to enable efficient and accurate computation of MAV performance, allowing for mechanism design optimization.

To this end research hypothesis has been formulated as: "Modeling of multi-physical dynamical system based on geometric reductions of the coupled Hamiltonian system, supplemented with mechanism for describing significant viscous effects, can be used for numerically more efficient computational modeling of the flapping wing MAV dynamics, while keeping the same level of accuracy as conventional approach, based on full discretization of the fluid domain."

1.4 Methodology

With the goal of developing efficient and reliable computational model of an insect-type flapping wing aerial vehicle, coupled wing fluid system is considered from a geometric mechanics framework, enabling important computational model reductions. However, in order to prepare the model suitable for performing reductions, certain assumptions have to be introduced. Although the insect-type flapping wing aerodynamics is characterized by low values of Reynolds number, the boundary layer effects are neglected. Although counter-intuitive at first glance, this is justifiable because, due to the high flapping frequencies involved (and consequently large values of Strouhal number), there is no time for thick boundary layer to form. To this end, fluid flow around flapping wings can be modeled as potential and incompressible, while viscous effects can effectively be captured by modeling vortex wake, shed from both leading and trailing edges [32].

By following this approach, fluid velocity can be decomposed by Helmholtz-Hodge decomposition into curl-free and divergence-free parts. The first, curl-free part, is then used to model added inertia "felt" by wing because of being sumberged in surrounding fluid - this is an important phenomenon in insect-type flapping flight, due to large values of wing accelerations and highly complex wing kinematics. The second, divergence-free, part is used to model viscous effects of the fluid, by means of modeling vortex wake shedding, evolution and influence on the flapping wing.

Based on these assumptions, reduced coupled multibody-fluid system equations of motion for a flapping wing aerial vehicle are derived, where added inertia effects are captured by performing Hamiltonian symplectic reduction, while viscous effects are accounted as an external load, modeled by the means of a vortex wake.

1.5 Thesis outline

The Introduction chapter, presenting motivation. literature review, hypothesis and research objectives, methodology and this thesis outline, is followed by six chapters.

Second chapter presents an introduction to the mathematical and physical concepts most important for development of reduced order coupled multibody system-fluid computational model of a flapping wing aerial vehicle. This includes a brief recap of the most important concepts of Lagrangian mechanics, while involved Lagrangian function is later utilized for modeling of a coupled wing-fluid system. Manifolds are introduced as a framework in which configuration spaces of both multibody system and ideal fluid evolve. This is followed by discussion on Lie group properties, with Lie group being a differentiable manifold, satisfying group properties. The chapter concludes with definitions of both rigid body and ideal fluid configuration spaces in Lie group frameworks.

Third chapter includes a derivation of the coupled multibody-fluid system equations of motion. Chapter starts with introduction of coupled multibody-fluid system configuration space in Lie group framework. This is followed by derivation of multibody system equations of motion in form of DAE index 1 system, together with kinematic reconstruction algorithm based on Munthe-Kaas type. The equations of motion are then finally derived for a coupled multibody-fluid system, taking into account the often neglected time-dependent nature of the added inertia matrix.

Fourth chapter introduces algorithm for added inertia calculation, based on symplectic reduction of coupled multibody-ideal fluid system, reducing out fluid variables by utilizing "particle relabeling" symmetry. By performing reduction, ideal fluid effects are captured solely by added inertia effects on the multibody system and the added inertia calculation problem is defined as exterior Laplace boundary value problem. This is followed by discussion of collocation boundary element method, with derivations of analytic solutions for singular integrals. The chapter concludes with validation of proposed added inertia effects calculation algorithm by comparison with analytical results for simple airfoil geometries.

Fifth chapter deals with modeling effects of divergence-free part of fluid velocity from Helmholtz-Hodge decomposition. To this end, discretization of infinitely thin airfoils with lumped vortex elements is introduced. This is followed with description of method for irrotational point vortex wake evolution, leading and trailing edge vortex shedding

techniques and vortex element circulation update. The chapter concludes with presentation of vortex wake-induced aerodynamic load calculation method, completing discussion of overall vortex effects modeling algorithm.

Sixth chapter presents numerical experiments for proposed insect-type flapping wing aerial vehicle computational model demonstration and validation. Due to the availability of benchmarking solutions, both numerical examples are based on fruit fly-like morphology. First test case includes analysis of smooth flapping pattern, leading to the fruit fly standstill hovering. Second test case involves an aerial vehicle with enlarged flapping wings of fruit fly morphology in Mars environmental conditions. The analyzed flapping pattern is characterized by non-smooth flapping angle functions, resulting from an earlier research and optimization of fruit fly-like aerial vehicle for standstill hovering flight on Mars.

Seventh and final chapter presents the most important thesis conclusions and possibilities for further research and improvements.

Theoretical framework

2.1 Introduction

This chapter includes discussion of mathematical and physical concepts, required for understanding and deriving mathematical models and algorithms presented in subsequent chapters. Lagrangian mechanics is briefly introduced as a framework from which the coupled multibody-ideal fluid system is considered, for formulating added inertia effects. This is followed by definitions of manifolds and Lie groups, very important concepts for this thesis, since configuration space of the coupled multibody-fluid system evolves on a Lie group. Finally, rigid body and ideal fluid configuration spaces in Lie group frameworks are described.

2.2 Lagrangian mechanics elementary concepts

In order to briefly introduce the framework of Lagrangian mechanics, equations of motion for a system of (many) particles are introduced as [33]

$$\dot{\boldsymbol{p}} = \sum_i \boldsymbol{F_i} = \boldsymbol{F}, \tag{2.1}$$

$$\dot{\boldsymbol{l}} = \sum_i \boldsymbol{T_i} = \boldsymbol{T}, \tag{2.2}$$

where $\boldsymbol{F_i}$ represents force acting on ith particle, $\boldsymbol{T_i}$ stands for torque acting on ith particle, while $\boldsymbol{p}$ and $\boldsymbol{l}$ represent linear and angular momentum.

Linear momentum for a system of particles is defined as

$$\boldsymbol{p} = m\boldsymbol{v_c}, \tag{2.3}$$

where $m = \sum_i m_i$ represents sum of all particles masses, while $\boldsymbol{v_c}$ represents velocity of mass center defined by

$$\boldsymbol{r_c} = \frac{\sum_i m_i \boldsymbol{r_i}}{\sum_i m_i}. \tag{2.4}$$

Angular momentum for a system of particles can be defined similarly as

$$\boldsymbol{l} = \boldsymbol{r_c} \times m\boldsymbol{v_c} + \sum_i \boldsymbol{r_i^c} \times m_i \boldsymbol{v_c}. \tag{2.5}$$

These equations govern the system of "free" particles motion under the influence of both externally applied and internal (acting between particles) forces. However, in order to capture wider range of applications, the constraints have to be introduced. At this point constraints are assumed to be holonomic, or in other words, constraint equation depends only on particles position and time

$$f\left(\boldsymbol{r_1}, \boldsymbol{r_2}, \ldots, \boldsymbol{r_N}, t\right) = 0. \tag{2.6}$$

Holonomic constraints allow the generalization from a system of particles to rigid bodies, by considering rigid body as consisting of infinitely many particles with fixed distances, leading to constraints

$$\|\boldsymbol{r_i} - \boldsymbol{r_j}\| - c_{ij} = 0, \tag{2.7}$$

where c_{ij} represents Euclidian distance between particles i and j.

If k constraints in the form (2.6) are introduced for N particles, the system variables can be reduced to $N - k$ generalized coordinates in addition to time variable, without explicit constraints as

$$\boldsymbol{r_1}\left(x_1, x_2, \ldots, x_N, t\right) \to \boldsymbol{r_1}\left(q_1, q_2, \ldots, q_{N-k}, t\right),$$
$$\vdots \tag{2.8}$$
$$\boldsymbol{r_N}\left(x_1, x_2, \ldots, x_N, t\right) \to \boldsymbol{r_N}\left(q_1, q_2, \ldots, q_{N-k}, t,\right),$$

where q_i represents ith generalized coordinate.

The overall work done by the constraint forces is assumed to be zero, since it is valid for rigid body constraint and for ideal kinematic constraints (without friction) due to the perpendicularity of constraint force to the allowed motion. Virtual infinitesimal

displacement for particle i is introduced as $\delta \boldsymbol{r_i}$, such that it is consistent with the constraints imposed on the system. D'Alembert's principle can now be defined as[33]

$$\sum_i \left(\boldsymbol{F_i} - \dot{\boldsymbol{p}}_i \right) \cdot \delta \boldsymbol{r_i} = 0. \tag{2.9}$$

However, in order to be useful, the equation needs to be transformed to generalized coordinates, based on constraint equations (2.8). Individual terms are transformed by using calculus rules as

$$\boldsymbol{v_i} = \frac{\mathrm{d}\boldsymbol{r_i}}{\mathrm{d}t} = \sum_{j=1}^{N-k} \frac{\partial \boldsymbol{r_i}}{\partial q_j} \cdot \frac{\mathrm{d}q_j}{\mathrm{d}t} + \frac{\partial \boldsymbol{r_i}}{\partial t}, \tag{2.10}$$

$$\delta \boldsymbol{r_i} = \sum_{j=1}^{N-k} \frac{\partial \boldsymbol{r_i}}{\partial q_j} \delta q_j, \tag{2.11}$$

$$\sum_{i=1}^{N} \boldsymbol{F_i} \cdot \delta \boldsymbol{r_i} = \sum_{i=1}^{N} \sum_{j=1}^{N-k} \boldsymbol{F_i} \cdot \frac{\partial \boldsymbol{r_i}}{\partial q_j} \delta q_j = \sum_{j=1}^{N-k} Q_j \delta q_j, \tag{2.12}$$

where $Q_j = \sum_{i=1}^{N} \boldsymbol{F_i} \cdot \frac{\partial \boldsymbol{r_i}}{\partial q_j}$ represents jth component of the generalized "force", i.e. the "force" acting in "direction" of jth generalized coordinate.

Utilizing expressions (2.10)-(2.12) and calculus identities, d'Alembert's principle (2.9) can be reformulated as

$$\sum_{i=1}^{N} m_i \dot{\boldsymbol{v}}_i \cdot \delta \boldsymbol{r_i} - \sum_{i=1}^{N} \boldsymbol{F_i} \cdot \delta \boldsymbol{r_i} = 0,$$

$$\sum_{i=1}^{N} \sum_{j=1}^{N-k} m_i \dot{\boldsymbol{v}}_i \cdot \frac{\partial \boldsymbol{r_i}}{\partial q_j} \delta q_j - \sum_{j=1}^{N-k} Q_j \delta q_j = 0,$$

$$\sum_{i=1}^{N} \sum_{j=1}^{N-k} \frac{\mathrm{d}}{\mathrm{d}t} \left(m_i \boldsymbol{v_i} \cdot \frac{\partial \boldsymbol{v_i}}{\partial \dot{q}_j} \right) \delta q_j - \sum_{i=1}^{N} \sum_{j=1}^{N-k} m_i \boldsymbol{v_i} \cdot \frac{\partial \boldsymbol{v_i}}{\partial q_j} \delta q_j - \sum_{j=1}^{N-k} Q_j \delta q_j = 0,$$

$$\sum_{j=1}^{N-k} \left(\frac{\mathrm{d}}{\mathrm{d}t} \left(\frac{\partial}{\partial \dot{q}_j} \left(\sum_{i=1}^{N} \frac{1}{2} m_i \boldsymbol{v_i} \cdot \boldsymbol{v_i} \right) \right) - \frac{\partial}{\partial q_j} \left(\sum_{i=1}^{N} \frac{1}{2} m_i \boldsymbol{v_i} \cdot \boldsymbol{v_i} \right) - Q_j \right) \delta q_j = 0, \tag{2.13}$$

where $T = \sum_{i=1}^{N} \frac{1}{2} m_i \boldsymbol{v_i} \cdot \boldsymbol{v_i}$ can be recognized as total kinetic energy of the system, leading to

$$\sum_{j=1}^{N-k} \left(\frac{\mathrm{d}}{\mathrm{d}t} \left(\frac{\partial T}{\partial \dot{q}_j} \right) - \frac{\partial T}{\partial q_j} - Q_j \right) \delta q_j = 0. \tag{2.14}$$

Since the constraints are assumed to be holonomic, leading to $N - k$ independent generalized coordinates and consequently independent virtual displacements δq_j, the only

way to enforce expression (2.14) is to enforce coefficients for each individual virtual displacement to vanish. This results in following $N - k$ Lagrange's equations (or generalized equations of motion)

$$\frac{\mathrm{d}}{\mathrm{d}t}\left(\frac{\partial T}{\partial \dot{q}_j}\right) - \frac{\partial T}{\partial q_j} - Q_j = 0, \qquad \text{for } j = 1, 2, \ldots, N - k. \tag{2.15}$$

In order to obtain what is usually known as Lagrange's equations of second kind (or Euler-Lagrange equations of motion), generalized forces are assumed to be conservative, and therefore defined by the scalar potential function V

$$Q_j = -\frac{\partial V}{\partial q_j}. \tag{2.16}$$

After noticing that the potential function is not the explicit function of generalized velocity (but only of generalized positions), leading to $\frac{\partial V}{\partial \dot{q}_j} = 0$, Lagrange's equations (2.15) can be rewritten as

$$\frac{\mathrm{d}}{\mathrm{d}t}\left(\frac{\partial (T - V)}{\partial \dot{q}_j}\right) - \frac{\partial (T - V)}{\partial q_j} = 0, \qquad \text{for } j = 1, 2, \ldots, N - k. \tag{2.17}$$

By definition, the Lagrangian is introduced as a difference between kinetic and potential energy $\mathcal{L} = T - V$, leading to the final expression for Lagrange's equations of second kind

$$\frac{\mathrm{d}}{\mathrm{d}t}\left(\frac{\partial \mathcal{L}}{\partial \dot{q}_j}\right) - \frac{\partial \mathcal{L}}{\partial q_j} = 0, \qquad \text{for } j = 1, 2, \ldots, N - k. \tag{2.18}$$

2.3 Manifolds

2.3.1 Definition

The conventional approach in describing motion is to utilize Euclidean vector space (n-dimensional space of real numbers $\mathbb{R}^n$, equipped with dot product), as also used in section 2.2. However, many physical phenomena evolve on more complicated structure, while the Euclidean space is only a locally valid assumption. Probably the most intuitive phenomenon to consider is a particle motion constrained to a sphere surface of two dimensions $\mathbb{S}^2$, which cannot be described with single two-dimensional Cartesian-like coordinate system, but can be covered with a number of overlapping two-dimensional

local Cartesian coordinate systems [34]. To this end, n-dimensional manifold $\mathcal{M}$ can be modeled by n-dimensional hypersurface in p-dimensional Euclidean vector space $\mathbb{E}^p$, with $n \leq p$.

To be more mathematically rigorous in manifold definition, a set $(x_1, x_2, \ldots, x_n)$ describing all points in $\mathbb{R}^n$ is considered. The set is a manifold $\mathcal{M}$ if each point $P \in \mathcal{M}$ has a continuous one-to-one mapping on open set in $\mathbb{R}^n$[35]. Definition requires only the open set, therefore leading to local mappings on $\mathbb{R}^n$ and not requiring one global mapping of $\mathcal{M}$ to $\mathbb{R}^n$. The continuous one-to-one mapping requirement ensures continuity of both the function describing mapping from open neighborhood of point in $\mathcal{M}$ to open region in $\mathbb{R}^n$, and the function inverse - mathematical concept named homeomorphism. Therefore, manifold is by definition locally homeomorphic to vector space.
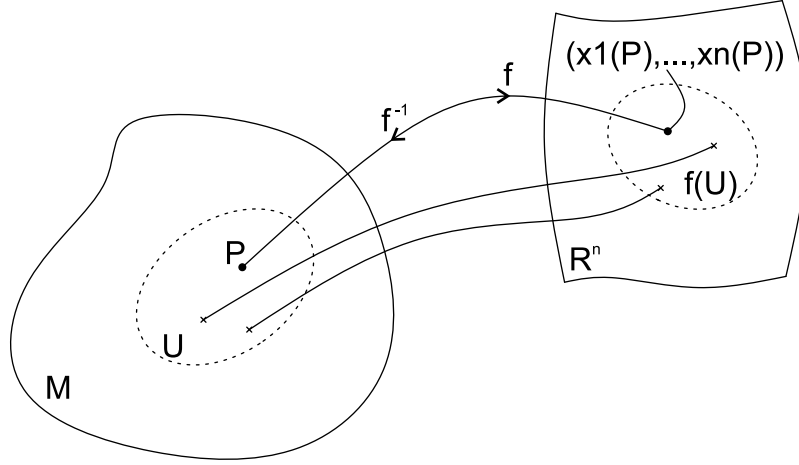
Figure 2.1: Illustration of the mapping from open neighborhood $U \in \mathcal{M}$ to local Euclidean space $f(U) \in \mathbb{R}^n$ or in other words, illustration of the (U, f) chart.

As shown in Fig. 2.1 illustrating mapping f from an open neighborhood $U \in \mathcal{M}$ to $f(U) \in \mathbb{R}^n$, map is used to associate point $P \in U$ with n-tuple $(x_1(P), \ldots, x_n(P)) \in f(U)$ [35]. The neighborhood and its map together are usually called chart.

2.3.2 Coordinate transformations

Naturally, there are overlaps between different neighborhoods, since each point in $\mathcal{M}$ is included in at least one open region. The overlaps between neighborhoods provide important insights on manifold properties. Suppose U_1 and U_2 are overlapping neighborhoods, with respective mappings f_1 and f_2 to open regions of $\mathbb{R}^n$. As illustrated in Fig. 2.2, the regions $f_1(U_1), f_2(U_2) \in \mathbb{R}^n$ can be completely distinct, with f_1 and f_2 mapping to two
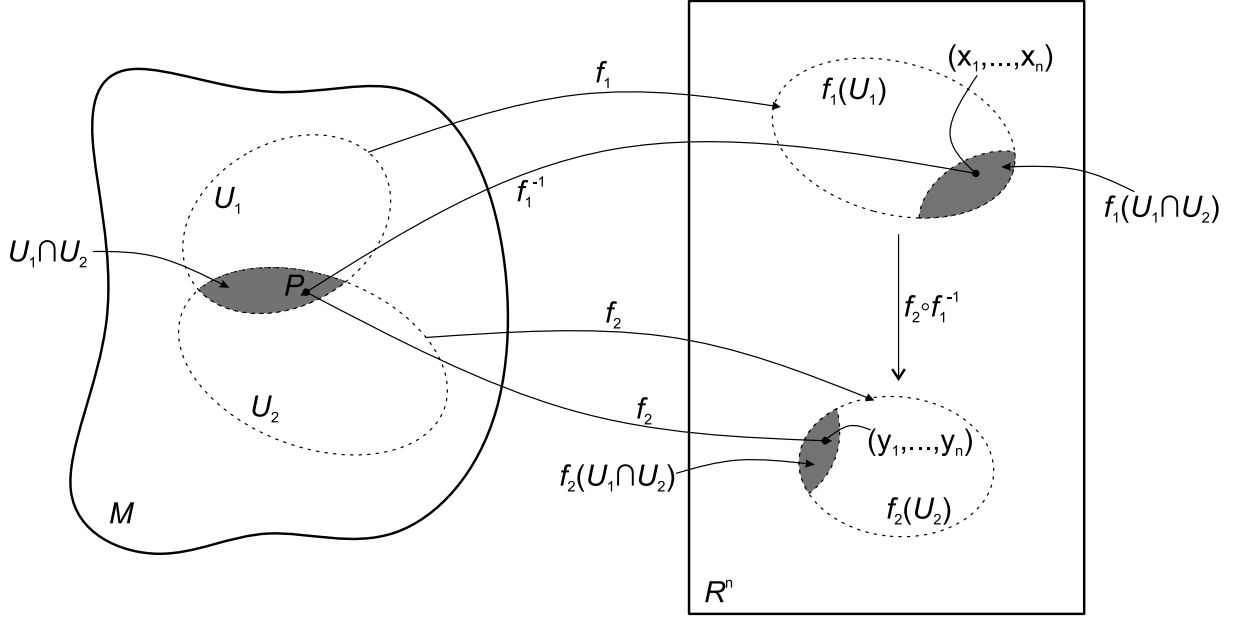
Figure 2.2: Illustration of two overlapping charts (U_1, f_1) and (U_2, f_2) and relation for coordinate transformation from one to another.

different coordinate systems [35]. However, because of overlaps, there is an expression relating these coordinate systems. If the point $P \in U_1 \cap U_2$ in the intersection is considered, it obviously maps to a point in both coordinate systems. In order to derive the expression for transformation from $f_1(U_1)$ to $f_2(U_2)$, the point $(x_1, x_2 \ldots, x_n) \in f_1(U_1)$ is introduced as mapping of point P by f_1. As illustrated in Fig. 2.2, the point $(x_1, x_2 \ldots, x_n)$ can then be transformed by inverse function f_1^{-1} to point P, and subsequently mapped by function f_2 to point $(y_1, y_2 \ldots, y_n) \in f_2(U_2)$. The expression for transformation between charts $(\mathbb{R}^n \to \mathbb{R}^n)$ is therefore a composite map $f_2 \circ f_1^{-1}$, providing functional relationship for coordinate transformation in the form

$$y_1 = y_1 \left(x_1, x_2, \ldots, x_n\right)$$
$$y_2 = y_2 \left(x_1, x_2, \ldots, x_n\right)$$
$$\vdots$$
$$y_n = y_n \left(x_1, x_2, \ldots, x_n\right). \tag{2.19}$$

If all functions y_i have continuous partial derivatives up to order k, with respect to all variables x_i, then the charts (U_1, f_1) and (U_2, f_2) are by definition C^k related. If an atlas (set of all charts) can be constructed such that every point in manifold $\mathcal{M}$ is included in at least one neighborhood and all overlapping charts are C^k related, the manifold $\mathcal{M}$ is

defined to be C^k related, while manifolds of class C^k, with $k \geq 1$ are called differentiable manifolds.

2.3.3 Curves and functions

Curve on the manifold is defined as a differentiable mapping $c : \mathbb{R} \to \mathcal{M}$ from open set in $\mathbb{R}$ to $\mathcal{M}$. As illustrated in Fig. 2.3, each point $\xi \in (a, b)$ is associated with a point $P \in \mathcal{M}$, therefore rendering a curve, parametrized by ξ [35]. Differentiability introduced in definition of curve in manifold ensures that the functions for image point coordinates $(x_1(\xi), x_2(\xi), \ldots, x_n(\xi))$ are differentiable with respect to parameter ξ.
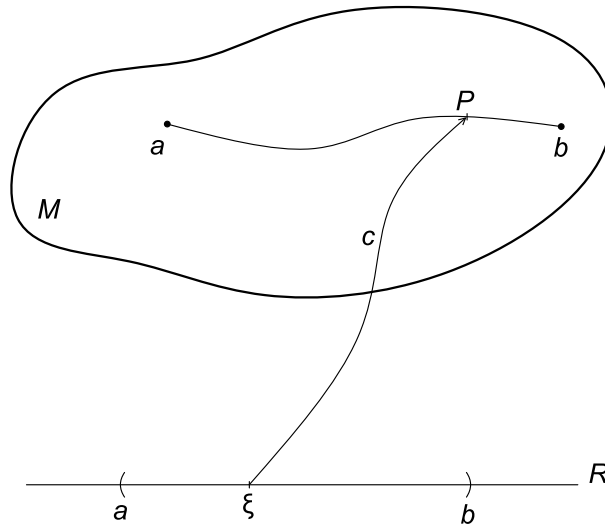
Figure 2.3: Illustration of the curve on manifold, mapping from the open region $\mathbb{R}$ to a curve in $\mathcal{M}$.

On the other hand, the function on manifold $f : \mathcal{M} \to \mathbb{R}$ associates a value to each point in manifold $P \in \mathcal{M}$. The function can be represented as $f(P) = f(x_1, x_2, \ldots, x_n)$ and if the expression is differentiable with respect to all its arguments, the function is differentiable.

2.3.4 Tangent vector spaces

First, the curve on manifold $\mathcal{M}$ is introduced, which passes trough a point $P \in \mathcal{M}$, which can be described by equations

$$x_i = x_i(\xi), \text{ for } i = 1, 2, \ldots, n. \tag{2.20}$$

In addition to this, a differentiable function $f(x_1, x_2, \ldots, x_n)$ is introduced for manifold

$\mathcal{M}$, associating a scalar value with each point on the curve. However, if the relations (2.20) are taken into account, the function f can also be parameterized by ξ and considered as giving the value of function f at point on the curve with parameter value ξ. The function f can now be differentiated with respect to parameter ξ, by using the chain rule as

$$\frac{\mathrm{d}f}{\mathrm{d}\xi} = \sum_{i=1}^{n} \frac{\mathrm{d}x_i}{\mathrm{d}\xi} \frac{\partial f}{\partial x_i}, \tag{2.21}$$

where terms $\frac{\mathrm{d}x_i}{\mathrm{d}\xi}$ can be considered as components of the vector in Euclidean space, that is tangent to the curve defined by (2.20).

Since each curve is parameterized by unique parameter ξ, there is also a unique set of components $\frac{\mathrm{d}x_i}{\mathrm{d}\xi}$ for each given curve, and therefore each curve has a unique tangent vector. On the other hand, each vector is obviously tangent to an infinite number of different curves, and is by no means unique to the given curve.

In order to demonstrate that directional derivatives along curves at $\mathcal{M}$ form vector space in point $P \in \mathcal{M}$, scalars a and b are introduced, together with another curve $x_i = x_i(\mu)$, for $i = 1, 2, \ldots, n$, going through P. Derivative along the curve, with respect to parameter μ, is then calculated as

$$\frac{\mathrm{d}}{\mathrm{d}\mu} = \sum_{i=1}^{n} \frac{\mathrm{d}x_i}{\mathrm{d}\mu} \frac{\partial}{\partial x_i}, \tag{2.22}$$

which together with (2.21) leads to

$$a\frac{\mathrm{d}}{\mathrm{d}\xi} + b\frac{\mathrm{d}}{\mathrm{d}\mu} = \sum_{i=1}^{n} \left(a\frac{\mathrm{d}x_i}{\mathrm{d}\xi} + b\frac{\mathrm{d}x_i}{\mathrm{d}\mu} \right) \frac{\partial}{\partial x_i}. \tag{2.23}$$

It can be noticed that the term $a\frac{\mathrm{d}x_i}{\mathrm{d}\xi} + b\frac{\mathrm{d}x_i}{\mathrm{d}\mu}$ represents components of a new vector, tangent to curve going through P. Therefore, there exists a parameter λ such that derivative along curve at P is equal to

$$\frac{\mathrm{d}}{\mathrm{d}\lambda} = \sum_{i=1}^{n} \left(a\frac{\mathrm{d}x_i}{\mathrm{d}\xi} + b\frac{\mathrm{d}x_i}{\mathrm{d}\mu} \right) \frac{\partial}{\partial x_i} = a\frac{\mathrm{d}}{\mathrm{d}\xi} + b\frac{\mathrm{d}}{\mathrm{d}\mu}, \tag{2.24}$$

therefore demonstrating closure under linear combination.

It follows from (2.21) that $\frac{\mathrm{d}}{\mathrm{d}\xi}$ can be written for any ξ as linear combination of terms $\frac{\partial}{\partial x_i}$, which therefore from a basis of the vector space, with $\frac{\mathrm{d}x_i}{\mathrm{d}\xi}$ as respective components.

This leads to the interesting conclusion that there is a one-to-one correspondence between space of tangent vectors and derivatives along curves at point P.

Since curve tangents are vectors, different vectors at P can be added together. However, it is very important to note that the vectors at two different points, in general, lie in different vector spaces and therefore cannot be added together. This is because vectors lie in tangent space to $\mathcal{M}$ in point P, usually denoted $\mathcal{T}_P\mathcal{M}$, as illustrated in Fig. 2.4 for tangent spaces with respective basis vectors at three different points on surface of the sphere representing manifold [34]. It is obvious from the basis vectors in figure that the summation of vectors at two different points is completely meaningless operation. The term vector is therefore used to denote a vector at specific point $P \in \mathcal{M}$, while the term vector field is introduced to denote a rule defining a vector at each point in $\mathcal{M}$.
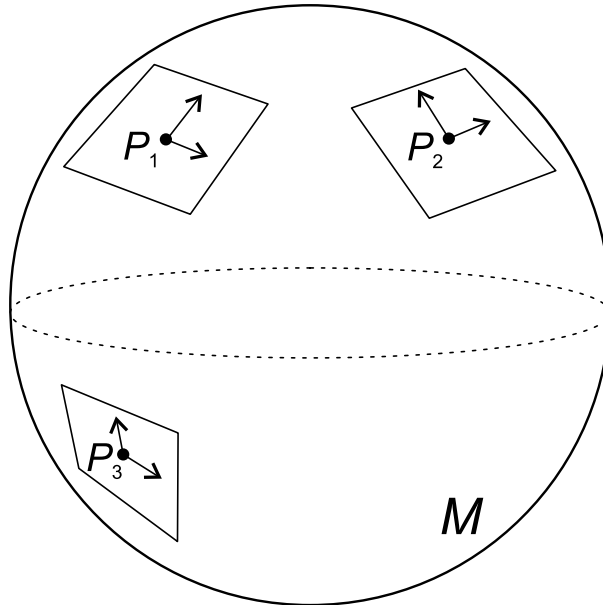
Figure 2.4: Illustration of tangent spaces with respective basis vectors at three different points on sphere surface (manifold $\mathcal{M}$).

2.3.5 Tangent bundles

A manifold $\mathcal{M}$, combined with all its tangent spaces $\mathcal{T}_P\mathcal{M}$, constitutes a tangent bundle (or fiber bundle) $\mathcal{T}\mathcal{M}$. The illustration of a one dimensional manifold (curve) $\mathcal{M}$, with three points P_1, P_2, P_3 and respective tangent spaces $\mathcal{T}_{P_1}\mathcal{M}, \mathcal{T}_{P_2}\mathcal{M}, \mathcal{T}_{P_3}\mathcal{M}$ is shown in Fig. 2.5. Tangent spaces in this particular case are lines, tangent to each point on the curve, and of infinite length to be capable of "accommodating" vector of any size. The tangent bundle is illustrated by two different representations, the representation in

Fig. 2.5(a) includes a natural tangent representation, while Fig. 2.5(b) represents vector spaces as vertical lines (not tangent to the curve) to illustrate the fact that individual tangent vector spaces do not intersect in mathematical sense, i.e. each vector space is "parallel" to another and intersects a manifold $\mathcal{M}$ only at the point of tangent space definition. The name fiber bundle, comes from this illustration, which includes "bundling" of all presented "fibers" (tangent vector spaces).

Let variable x be the coordinate of the one dimensional manifold $\mathcal{M}$, illustrated in Fig. 2.5. In order to find coordinates for tangent spaces $\mathcal{T}_{P_i}\mathcal{M}$ in open region $a < x < b$, for some scalars a and b, tangent vector $\boldsymbol{v}$ is defined as

$$\boldsymbol{v} = y\frac{\partial}{\partial x}, \tag{2.25}$$

where y is a coordinate for tangent space $\mathcal{T}_{P_i}\mathcal{M}$, while $\frac{\partial}{\partial x}$ represents basis vector as discussed in previous subsection.
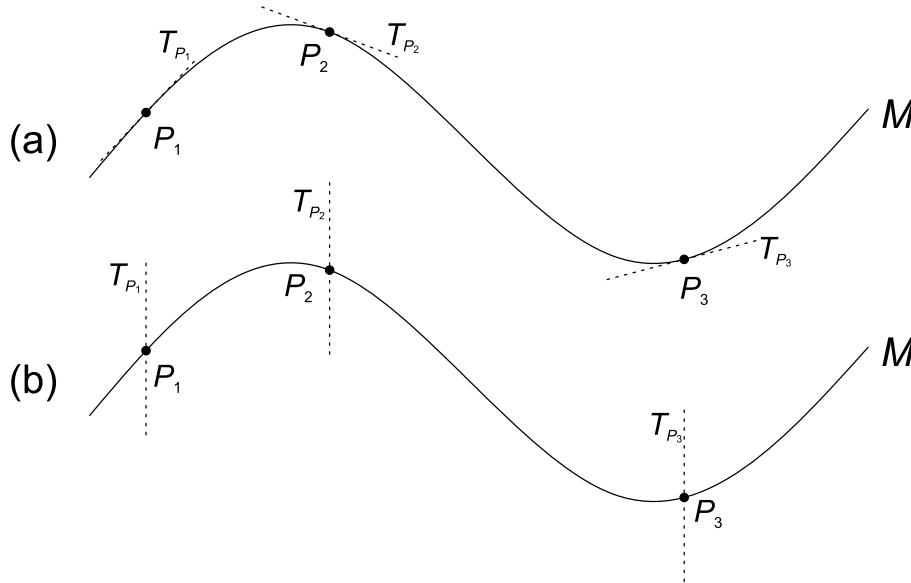
Figure 2.5: Illustration of one-dimensional manifold together with few tangent spaces, drawn tangent to the manifold (a) or parallel to each other (b).

Each fiber has a fixed (and unique) value of x since it is uniquely defined for only one point on manifold and x is manifold coordinate. In addition to variable x defining a point at which the tangent space is defined, variable y defines a particular vector in this tangent space. Since each vector can therefore be defined by coordinates (x, y), and since this is valid for any point on manifold, and any vector in tangent space, the tangent bundle $\mathcal{T}\mathcal{M}$ is also a manifold. In this case, the manifold dimension is two, while in the general case

it can be shown that the dimension of tangent bundle manifold $\mathcal{TM}$ will be $m + n$ if m represents dimensions of base manifold $\mathcal{M}$, while n represents dimension of tangent space $\mathcal{T}_{P_i}\mathcal{M}$ [35].

2.3.6 One-forms

A one-form is defined as a linear function associating a real value with each vector. To be more precise, one-form α at point $P \in \mathcal{M}$ associates a real number $\alpha(\boldsymbol{v}) \in \mathbb{R}$ with vector $\boldsymbol{v} \in \mathcal{T}_P$.

Because of the linearity assumption, any one-form operation on n-dimensional vector can be represented as

$$\alpha(\boldsymbol{v}) = \alpha_1 v_1 + \alpha_2 v_2 + \cdots + \alpha_n v_n \tag{2.26}$$

and therefore one-form obviously satisfies vector space axioms (this can be trivially proved from expression (2.26)). The one-form is therefore named dual vector, and the space of one-forms in point P is named cotangent bundle and denoted $\mathcal{T}_P^*\mathcal{M}$ (dual space to $\mathcal{T}_P\mathcal{M}$).

Probably one of the most well-known one-forms is a gradient of the function. Although gradient is often considered a vector, it is more correct to consider it a one-form in differential geometry sense [35]. Another way to look at the distinction between vectors and one-forms is in the context of linear algebra, where vectors are conventionally represented by column arrays, while in this framework one-forms (such as gradient) appear as row arrays.

2.4 Lie groups

Lie groups, introduced and described in this section, represent an important framework in which a configuration space, as well as phase state space, of a proposed coupled multibody-fluid computational model evolves.

2.4.1 Lie derivatives

It is necessary to introduce the concept of congruence before defining Lie derivatives. Vector fields has been defined as a rule for defining a vector in each point of the manifold. This can be reversed to define a problem of defining a curve through a point, for which a respective tangent vector always satisfies the given vector field. For this purpose, vector field is defined as a function of position P, as $\boldsymbol{v_i}(P) = \boldsymbol{v_i}(x_i)$, while tangent vector to

the curve parameterized by ξ is defined as $\frac{\mathrm{d}x_i}{\mathrm{d}\xi}$, leading to the set of first-order ordinary differential equations (ODEs)

$$\frac{\mathrm{d}x_i}{\mathrm{d}\xi} = \boldsymbol{v_i}(x_i). \tag{2.27}$$

A unique solution always exists for a given set of ODEs (2.27) in some neighborhood of point P [36], leading to the fact that the resulting integral curves cannot intersect each other. In addition to this, this also ensures that there exists an integral curve passing through any $P \in \mathcal{M}$, because set of ODEs can be solved with P as the initial solution. Therefore, for each n-dimensional manifold, there is a $(n-1)$-dimensional family of curves "filling" entire manifold, called congruence [35].

These curves provide a mapping of manifold onto itself, because at any ξ, there is a (sufficiently small) number $\Delta\xi$, defining a mapping from $P \in \mathcal{M}$ to the point on the manifold that is at $\Delta\xi$ distance along the curve. If such mapping exists for any $\Delta\xi$, then it can be said that there exists a one-dimensional family of mappings, with composition law allowing for addition of different $\Delta\xi$. This kind of mapping is usually called Lie dragging in literature, for the illustration of "dragging" something along congruence by $\Delta\xi$.

In the example of a function f defined on manifold, "dragging" along congruence defines new function $f_{\Delta\xi}$ such that if point P_1 with parameter along the curve ξ maps by "Lie dragging" to P_2 with parameter $\xi + \Delta\xi$, function values are

$$f(P_1) = f_{\Delta\xi}(P_2). \tag{2.28}$$

If the function f is constant along congruence $\left(\frac{\mathrm{d}f}{\mathrm{d}\xi} = 0\right)$, then it is also invariant under presented mapping.

Since the manifolds in general do not necessary include any metrics, it is difficult to define derivatives on manifolds. However, with congruence introduced, if there exists a curve between points "distance" can be represented by the difference in parameter value, therefore providing possibility of defining derivative with respect to curve parameter.

If the scalar function is evaluated at ξ_0 and then "dragged" (2.28) along the curve by $\Delta\xi$, derivative with respect to parameter ξ in point ξ_0 can then be defined as

$$\lim_{\Delta\xi\to 0} \frac{f_{\Delta\xi}(\xi_0) - f(\xi_0)}{\Delta\xi} = \lim_{\Delta\xi\to 0} \frac{f(\xi_0 + \Delta\xi) - f(\xi_0)}{\Delta\xi} = \frac{\mathrm{d}f}{\mathrm{d}\xi}(\xi_0). \tag{2.29}$$

In other words, Lie derivative of scalar function is equal to the conventional derivative of

the function with respect to curve parameter.

For the sake of clarity, Lie derivatives are usually expressed in L_Y notation, where Y in the subscript represents the vector field generating congruence (mapping). Therefore, Lie derivative of scalar function along the congruence (with curve parameters ξ) generated by vector field Y can be represented as

$$L_Y f = \frac{\mathrm{d}f}{\mathrm{d}\xi}. \tag{2.30}$$

In the similar procedure [35], Lie derivative of the vector field X along the congruence generated by vector field Y can be derived. The result is now expressed as

$$L_Y X = [Y, X], \tag{2.31}$$

where $[Y, X]$ represents Lie bracket of vector fields Y and X, which is here equal to

$$[Y, X] = \frac{\mathrm{d}}{\mathrm{d}\xi} X - \frac{\mathrm{d}}{\mathrm{d}\mu} Y, \tag{2.32}$$

where μ represents parameter of the curve generated by vector field X.

Lie derivative of vector field, along the congruence defined by other vector field is obviously antisymmetric, resulting in

$$L_Y X = L_X Y, \tag{2.33}$$

for any two vector fields X and Y.

Very important concept (and important use of Lie derivatives) in physics is the invariance of tensor under a vector field, or

$$L_Y T = 0, \tag{2.34}$$

where T represents tensor that is invariant with respect to vector field Y. Invariance of tensor representing physically meaningful quantity under a vector field leads to the conservation of this quantity in respective transformation (symmetry which can be exploited in mathematical modeling, as will be shown in later sections).

2.4.2 Lie group definition

In order to be a group, set (collection of elements) G, equipped with binary operation $\cdot$ combining two elements of the group and resulting with another element of group (closure under $\cdot$), must satisfy following axioms [37]:

- *Associativity*: For $a, b, c \in G$

$$a \cdot (b \cdot c) = (a \cdot b) \cdot c. \tag{2.35}$$

- *Identity element*: There is an identity element $e \in G$ such that for any $a \in G$

$$a \cdot e = e \cdot a = a. \tag{2.36}$$

- *Inverse element*: For any element $a \in G$, there exists an inverse element $a^{-1} \in G$ for which

$$a \cdot a^{-1} = a^{-1} \cdot a = e, \tag{2.37}$$

where $e \in G$ represents identity element.

Now that both differentiable manifolds and groups are introduced, the important concept of a Lie group G can be introduced as a group that is also a differentiable manifold, with the group operation generating a differentiable map of manifold onto itself. If element $a \in G$ is inducing a map of G onto itself, it maps any other element $b \in G$ as $b \mapsto ab$ (known as left translation of b by a) or $b \mapsto ba$ (known as right translation of b by a). The Lie group does not have to be Abelian, meaning that the left and right translation generally don't have the same result ($ab \neq ba$ in general).

Interesting properties can be revealed by considering the neighborhood of identity element $e \in G$. Since by definition of a group identity element is mapped with (left or right) translation by a into a itself (2.36), the neighborhood of e is mapped on a neighborhood of a, as illustrated in Fig. 2.6 for the case of left translation [35].

Since the map is differentiable, it can be used to map not only the elements but also curves and tangent vectors. Therefore, a specific map describing left translation of tangent vectors at e into tangent vectors at a denoted $L_a : T_e \to T_a$ can now be defined (original and mapped curve and tangent vector are also illustrated in Fig. 2.6). Any vector field V
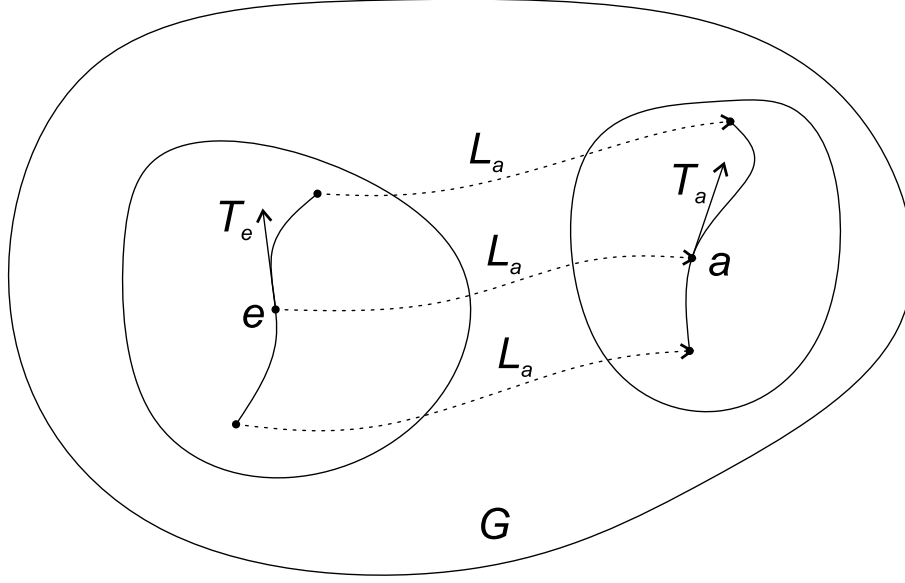
Figure 2.6: Illustration of left translation L_a mapping the neighborhood of e onto the neighborhood of a, with illustrations of point, curve and tangent vector mappings.

on Lie group G is left-invariant if previously defined L_a maps vector field V at identity e to same vector field V at a, i.e. $L_a : V(e) \mapsto V(a) \ \forall \ a$.

It can be shown that if V_1 and V_2 are two left-invariant vector fields, then their Lie bracket is also a left-invariant vector field, i.e. $L_a : [V_1, V_2] \mapsto [V_1, V_2]$ [35]. This is an important result, because it can be said that left-invariant vector fields form a Lie algebra, usually denoted g.

2.4.3 Lie algebras

A Lie algebra is only mentioned in previous subsection, without explanation or definition. Actually, every Lie group G has the associated Lie algebra g. Formally, Lie algebra is defined as a real vector space V, together with a binary operation denoted $[\cdot, \cdot]$, which for any two input vector produces result in g (i.e. operation with $g \times g \to g$), satisfying the following properties [38]:

- *Bilinearity*: For any scalars a, b, and vectors $x, y, z \in g$

$$
\begin{aligned}
[ax + by, z] &= a\,[x, z] + b\,[y, z], \\
[z, ax + by] &= a\,[z, x] + b\,[z, y].
\end{aligned}
\tag{2.38}
$$

- *Alternativity*: For any $x \in g$

$$[x, x] = 0. \tag{2.39}$$

- *Jacobi identity*: For any $x, y, z \in g$

$$[x\,[y, z]] + [y\,[z, x]] + [z\,[x, y]] = 0. \tag{2.40}$$

Presented properties also imply an important and not mentioned property of anticommutativity, which can be derived from bilinearity and alternativity properties, for any $x, y \in g$ as

$$[x + y, x + y] = 0,$$
$$[x, x] + [y, x] + [x, y] + [y, y] = 0,$$
$$[y, x] + [x, y] = 0,$$
$$[x, y] = -[y, x]. \tag{2.41}$$

Binary operation $[\cdot, \cdot]$ is named Lie bracket. One Lie bracket operator, commutator of vector fields (2.32) has already been mentioned, but without precise definition of Lie bracket necessary properties. However, there are many useful Lie brackets that will be encountered for Lie groups presented in following chapters.

2.5 Rigid body motion in Lie group setting

An important concept in any multibody system analysis is the concept of rigid body, where the rigidity can be defined as the property constraining any two points of the body to be constant distance apart during any motion.

A motion of any point on the unconstrained rigid body in $\mathbb{R}^3$ can be described by six degrees of freedom (DoF) - 3 DoF for position of the rigid body mass center and 3 DoF for orientation (attitude) of rigid body. As illustrated in Fig. 2.7, position of any point P on rigid body can be described as sum of position vectors for body center of mass C (due to rigid body translation) and vector pointing from C to P (due to rigid body rotation)

$$\boldsymbol{x}_P = \boldsymbol{x}_C + \boldsymbol{x}_{C \to P}, \tag{2.42}$$

where all vectors are expressed in inertial (spatial, fixed) reference frame.
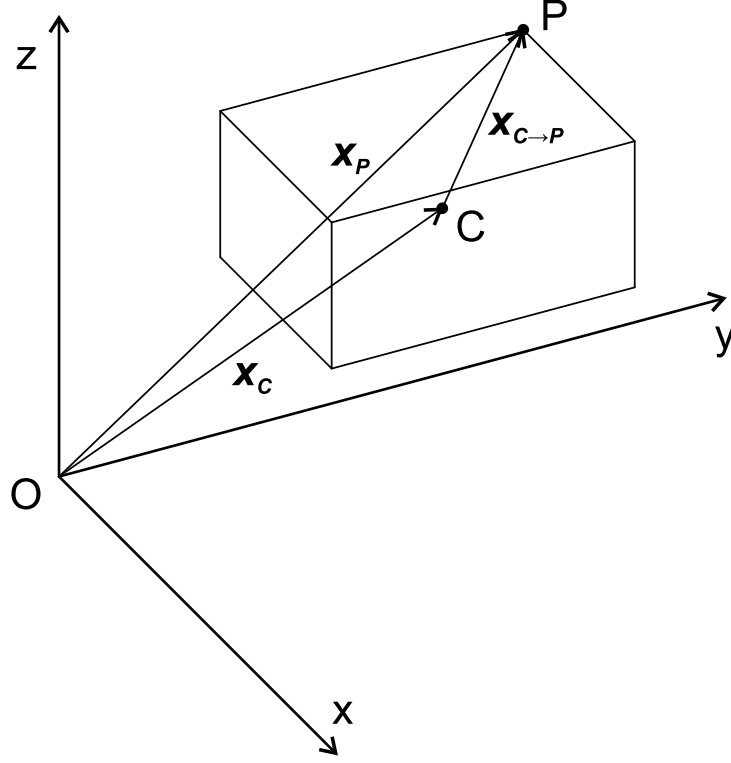
Figure 2.7: Description of any point P as sum of mass center position vector and vector pointing from center of mass to point P.

Since the center of mass translation description presents a trivial task, governed by Newton's law, further discussion focuses on the rigid body rotation, assuming the fixed center of mass, while all presented conclusions remain valid if the center of mass motion is included in analysis.

There are usually three coordinate frames interesting for consideration in framework of rigid bodies: material, spatial and body-fixed coordinate frame. Let $\mathcal{B}$ denote a reference configuration of rigid body, as an open set in $\mathbb{R}^3$. Set $\mathcal{B}$ is assumed to have piecewise smooth boundary. Let material points of rigid body be denoted $\boldsymbol{X} = (X_1, X_2, X_3) \in \mathcal{B}$, with X_i being ith coordinate in material reference frame with orthonormal basis $(\boldsymbol{m_1}, \boldsymbol{m_2}, \boldsymbol{m_3})$. A mapping $\beta : \mathcal{B} \to \mathbb{R}^3$ results with a configuration of $\mathcal{B}$ in spatial reference frame (spatial points of rigid body), with orthonormal basis $(\boldsymbol{e_1}, \boldsymbol{e_2}, \boldsymbol{e_3})$ [39]. Spatial points coordinates are denoted $\boldsymbol{x} = (x_1, x_2, x_3) \in \mathbb{R}^3$. Mapping of rigid body from reference configuration (material coordinate frame) to (spatial) configuration (spatial coordinate frame) is illustrated in Fig. 2.8.

In addition to these coordinate systems, it is also important to introduce body-fixed
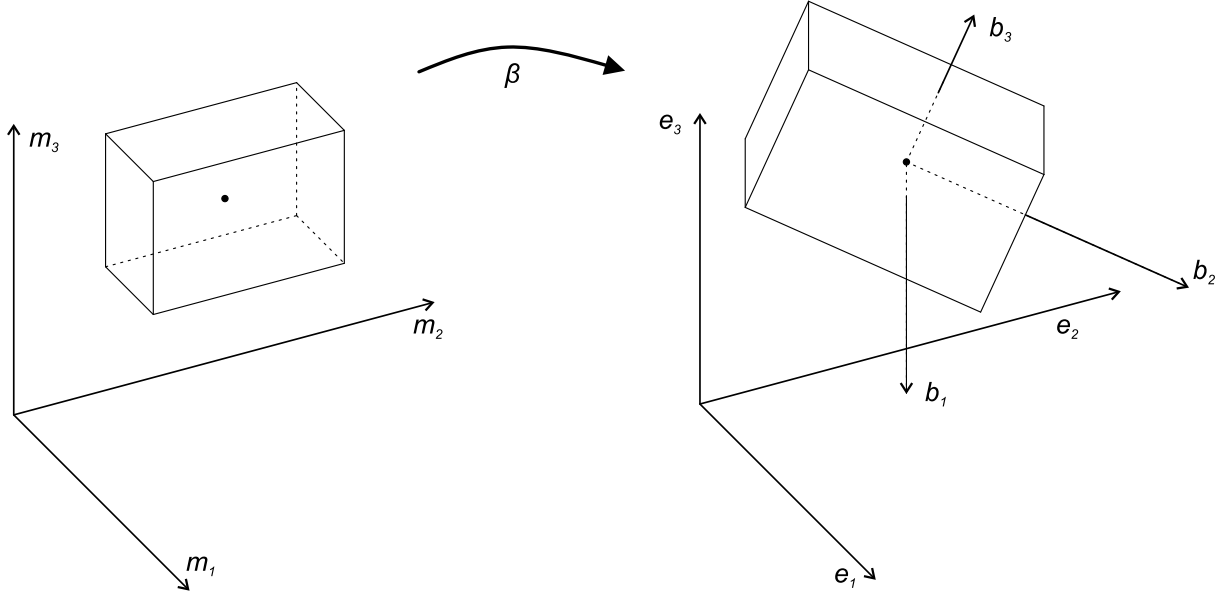
Figure 2.8: Illustration of transformation β from the material $(\boldsymbol{m_1}, \boldsymbol{m_2}, \boldsymbol{m_3})$ to the spatial $(\boldsymbol{e_1}, \boldsymbol{e_2}, \boldsymbol{e_3})$ reference frame and depiction of the body-fixed reference frame $(\boldsymbol{b_1}, \boldsymbol{b_2}, \boldsymbol{b_3})$, moving together with rigid body.

reference frame. As illustrated in Fig. 2.8, as rigid body rotates, spatial coordinate system is fixed in space, while the body-fixed reference frame rotates with the body and is usually anchored at the center of mass.

Since the origin (center of mass) is assumed to be fixed, and since any isometry of $\mathbb{R}^3$ that leaves the origin fixed can be considered rotation, which can be expressed as [39]

$$\boldsymbol{x}\left(\boldsymbol{X}, t\right) = \boldsymbol{R}(t)\boldsymbol{X}, \tag{2.43}$$

for any rotation from the reference configuration. Matrix $\boldsymbol{R}(t)$ represents a rotation matrix with property

$$\boldsymbol{R}^T \boldsymbol{R} = \boldsymbol{R}\boldsymbol{R}^T = \boldsymbol{I}, \tag{2.44}$$

where $\boldsymbol{I}$ represents 3×3 identity matrix. Determinant of the rotation matrix is $\det\left(\boldsymbol{R}(t)\right) = 1$. Configuration space of the rigid body rotation can therefore be identified with special orthogonal group $\boldsymbol{R}(t) \in SO(3)$. The group is closed under matrix multiplication, since for any $\boldsymbol{A}, \boldsymbol{B} \in SO(3)$, matrix product $AB \in SO(3)$, since determinant of the matrix product equals to the product of individual determinants. Group identity is 3×3 identity matrix I, while the inverse element is matrix transpose $\boldsymbol{R}^T$. Lie algebra $so(3)$ of the group

$SO(3)$ contains the elements in form of the skew symmetric matrix

$$\tilde{\boldsymbol{\omega}} = \begin{pmatrix} 0 & -\omega_3 & \omega_2 \\ \omega_3 & 0 & -\omega_1 \\ -\omega_2 & \omega_1 & 0 \end{pmatrix} \in so(3). \tag{2.45}$$

Tilde operator $\tilde{\ }$ maps the vector $\omega \in \mathbb{R}^3$ to Lie algebra $so(3)$. It is interesting to note connection between symmetric matrices and vector product

$$\tilde{\boldsymbol{u}}\boldsymbol{v} = \boldsymbol{u} \times \boldsymbol{v}, \tag{2.46}$$

for any $\boldsymbol{u}, \boldsymbol{v} \in \mathbb{R}^3$. Since the vector product is anticommutative and satisfies Jacobi identity [38] following expression can be derived for any $\boldsymbol{u}, \boldsymbol{v}, \boldsymbol{w} \in \mathbb{R}^3$

$$\begin{aligned} \widetilde{(\tilde{\boldsymbol{u}}\boldsymbol{v})}\boldsymbol{w} &= (\boldsymbol{u} \times \boldsymbol{v}) \times \boldsymbol{w} = -\boldsymbol{w} \times (\boldsymbol{u} \times \boldsymbol{v}) \\ &= \boldsymbol{u} \times (\boldsymbol{v} \times \boldsymbol{w}) + \boldsymbol{v} \times (\boldsymbol{w} \times \boldsymbol{u}) \\ &= \boldsymbol{u} \times (\boldsymbol{v} \times \boldsymbol{w}) - \boldsymbol{v} \times (\boldsymbol{u} \times \boldsymbol{w}) \\ &= \tilde{\boldsymbol{u}}\tilde{\boldsymbol{v}}\boldsymbol{w} - \tilde{\boldsymbol{v}}\tilde{\boldsymbol{u}}\boldsymbol{w} = (\tilde{\boldsymbol{u}}\tilde{\boldsymbol{v}} - \tilde{\boldsymbol{v}}\tilde{\boldsymbol{u}})\,\boldsymbol{w} = [\boldsymbol{u}, \boldsymbol{v}]\,\boldsymbol{w}. \end{aligned} \tag{2.47}$$

Therefore, $so(3)$ is identified with $\mathbb{R}^3$, while the cross product in $\mathbb{R}^3$ is equivalent to Lie bracket in $so(3)$.

The velocity phase space of a rigid body rotation is identified with tangent bundle $TSO(3)$, while the momentum phase space is identified with $T^*SO(3)$[39].

The velocity at a material point X can be defined as

$$\boldsymbol{V}\left(\boldsymbol{X}, t\right) = \frac{\partial \boldsymbol{x}\left(\boldsymbol{X}, t\right)}{\partial t} = \frac{\partial}{\partial t}\left(\boldsymbol{R}(t)\boldsymbol{X}\right) = \dot{\boldsymbol{R}}(t)\boldsymbol{X}, \tag{2.48}$$

where the resulting $\boldsymbol{V}\left(\boldsymbol{X}, t\right)$ is often called material or Lagrangian velocity.

In addition to this, spatial or Eulerian velocity can be defined in similar manner, but based on the position in spatial frame $\boldsymbol{x}$, instead of the material position $\boldsymbol{X}$

$$\boldsymbol{v}(\boldsymbol{x}, t) = \boldsymbol{V}\left(\boldsymbol{X}, t\right) = \dot{\boldsymbol{R}}(t)\boldsymbol{R}^{-1}(t)\boldsymbol{x} = \dot{\boldsymbol{R}}(t)\boldsymbol{R}^T(t)\boldsymbol{x}. \tag{2.49}$$

On the other hand, the velocity can also be defined by assuming the $\boldsymbol{X}$ is time

dependent, while $\boldsymbol{x}$ is fixed (i.e. "looking at the motion from body-fixed reference frame"), leading to

$$\boldsymbol{v}_b(\boldsymbol{X}, t) = -\frac{\partial \boldsymbol{X}(x, t)}{\partial t} = -\frac{\partial}{\partial t}\left(\boldsymbol{R}^{-1}(t)\boldsymbol{x}\right), \tag{2.50}$$

where derivative of the inverse matrix $\frac{\partial}{\partial t}\left(\boldsymbol{R}^{-1}(t)\right)$ can be calculated from

$$\boldsymbol{R}\boldsymbol{R}^{-1} = \boldsymbol{I},$$
$$\frac{\partial}{\partial t}\left(\boldsymbol{R}\boldsymbol{R}^{-1}\right) = \frac{\partial \boldsymbol{I}}{\partial t},$$
$$\dot{\boldsymbol{R}}\boldsymbol{R}^{-1} + \boldsymbol{R}\frac{\partial}{\partial t}\boldsymbol{R}^{-1} = \boldsymbol{0},$$
$$\boldsymbol{R}\frac{\partial}{\partial t}\boldsymbol{R}^{-1} = -\dot{\boldsymbol{R}}\boldsymbol{R}^{-1},$$
$$\frac{\partial}{\partial t}\boldsymbol{R}^{-1} = -\boldsymbol{R}^{-1}\dot{\boldsymbol{R}}\boldsymbol{R}^{-1}. \tag{2.51}$$

By utilizing (2.51), expression (2.50) can be reformulated as

$$\boldsymbol{v}_b(\boldsymbol{X}, t) = \boldsymbol{R}^{-1}\dot{\boldsymbol{R}}\boldsymbol{R}^{-1}\boldsymbol{x}$$
$$= \boldsymbol{R}^{-1}\dot{\boldsymbol{R}}\boldsymbol{X}$$
$$= \boldsymbol{R}^T\boldsymbol{V} = \boldsymbol{R}^T\boldsymbol{v}. \tag{2.52}$$

Similarly as for derivation of (2.51), derivatives of $\boldsymbol{R}\boldsymbol{R}^T = \boldsymbol{I}$ and $\boldsymbol{R}^T\boldsymbol{R} = \boldsymbol{I}$ (2.44) leads to expressions

$$\frac{\mathrm{d}}{\mathrm{d}t}\left(\boldsymbol{R}\boldsymbol{R}^T\right) = \frac{\mathrm{d}}{\mathrm{d}t}\left(\boldsymbol{I}\right)$$
$$\dot{\boldsymbol{R}}\boldsymbol{R}^T + \boldsymbol{R}\dot{\boldsymbol{R}}^T = \boldsymbol{0}$$
$$\dot{\boldsymbol{R}}\boldsymbol{R}^T + \left(\dot{\boldsymbol{R}}\boldsymbol{R}^T\right)^T = \boldsymbol{0}, \tag{2.53}$$
$$\frac{\mathrm{d}}{\mathrm{d}t}\left(\boldsymbol{R}^T\boldsymbol{R}\right) = \frac{\mathrm{d}}{\mathrm{d}t}\left(\boldsymbol{I}\right)$$
$$\dot{\boldsymbol{R}}^T\boldsymbol{R} + \boldsymbol{R}^T\dot{\boldsymbol{R}} = \boldsymbol{0}$$
$$\left(\boldsymbol{R}^T\dot{\boldsymbol{R}}\right)^T + \boldsymbol{R}^T\dot{\boldsymbol{R}} = \boldsymbol{0}, \tag{2.54}$$

leading to the conclusion that both $\dot{\boldsymbol{R}}\boldsymbol{R}^T$ and $\boldsymbol{R}^T\dot{\boldsymbol{R}}$ are skew-symmetric.

Classical definition of angular velocity in spatial (fixed) reference frame can be inferred

from

$$\boldsymbol{v} = \boldsymbol{\Omega} \times \boldsymbol{x} = \tilde{\boldsymbol{\Omega}}\boldsymbol{x}. \qquad (2.55)$$

By combining (2.55) and (2.49), angular velocity in spatial reference frame can be formulated as

$$\tilde{\boldsymbol{\Omega}} = \dot{\boldsymbol{R}}\boldsymbol{R}^{T}, \qquad (2.56)$$

while the angular velocity in body-fixed reference frame can be defined as

$$\tilde{\boldsymbol{\omega}} = \boldsymbol{R}^{T}\dot{\boldsymbol{R}}, \qquad (2.57)$$

with relations between angular velocities $\boldsymbol{\Omega}, \boldsymbol{\omega} \in \mathbb{R}^{3}$ and $\tilde{\boldsymbol{\Omega}}, \tilde{\boldsymbol{\omega}} \in so(3)$

$$\boldsymbol{\Omega} = \boldsymbol{R}\boldsymbol{\omega}, \qquad (2.58)$$

$$\tilde{\boldsymbol{\Omega}} = \boldsymbol{R}\tilde{\boldsymbol{\omega}}\boldsymbol{R}^{T}. \qquad (2.59)$$

Dynamics of rigid body, evolving on $TSO(3)$ cam therefore be reconstructed from (2.57), by formulating system of linear differential equations for $\boldsymbol{R} \in SO(3)$

$$\dot{\boldsymbol{R}} = \boldsymbol{R}\tilde{\boldsymbol{\omega}}. \qquad (2.60)$$

2.6 Ideal fluid in Lie group setting

If the ideal fluid domain is denoted $\mathcal{F}$, the configuration space Q_F constitutes a group of volume-preserving diffeomorphisms $Q_F = G_F = \mathrm{Diff}_{\mathrm{vol}}(\mathcal{F})$. This is an infinite dimensional Lie group with composition as group closure operation.

Each mapping β_F in group G is a mapping of domain $\mathcal{F}$ to itself ($\beta_F : \mathcal{F} \to \mathcal{F}$). Any fluid "particle" (point) from initial (material) configuration $\boldsymbol{X} \in \mathcal{F}$ is mapped by β_F to a current point position $\boldsymbol{x} = \beta_F(\boldsymbol{X}) \in \mathcal{F}$. Therefore, defining β_F provides enough information to prescribe motion of each fluid "particle" - it describes a fluid configuration. The fact that β_F is volume-preserving corresponds to the incompressibility property of ideal fluids, while diffeomorphism assumption ensures that there are no discontinuities in fluid domain (such as cavities for example).

Motion of the fluid can be considered as a family of time dependent mappings of individual fluid particles, giving the position of material point $\boldsymbol{X}$ in the spatial coordinate

frame, at time t as $\boldsymbol{x} = \beta_F(\boldsymbol{X}, t)$. Fluid material velocity field can be defined, similar to the rigid body velocity definition (2.48), as partial derivative of the mapping

$$\boldsymbol{V} = \frac{\partial \beta_F(\boldsymbol{X}, t)}{\partial t}. \tag{2.61}$$

Again similarly as for the rigid body case, spatial velocity field can be defined as

$$\boldsymbol{v} = \boldsymbol{V} = \frac{\partial \beta_F(\beta_F^{-1}\boldsymbol{x}, t)}{\partial t}, \tag{2.62}$$

or in a different notation, without explicit writing of variables

$$\boldsymbol{v} = \dot{\beta_F} \circ \beta_F^{-1}, \tag{2.63}$$

where $\circ$ represents function composition operator (the operator of the $\text{Diff}_{\text{vol}}(\mathcal{F})$ Lie group).

Transformation of the fluid "particle" from the material to spatial reference frame is illustrated in Fig. 2.9, with spatial velocity vector indicated.
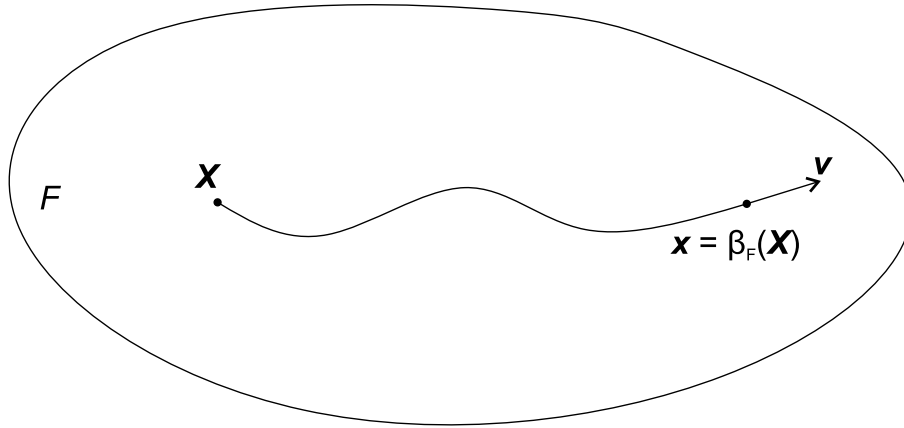
Figure 2.9: Illustration of the ideal fluid "particle" mapping β_F from material to spatial reference frame and spatial velocity vector $\boldsymbol{v}$.

The interesting property of ideal fluids (or even more generally, incompressible fluids) is invarance of fluid kinetic energy with respect to the right translation on the pertinent group $\text{Diff}_{\text{vol}}(\mathcal{F})$. In other words, the right translations $R_y : G_F \rightarrow G_F$ in the form $(R_h(g) = g \circ h)$. This can be explained according to [40] as being due to the fact that right translation by h acts before a diffeomorphism g that evolves with velocity $\dot{g}$. The volume-preserving diffeomorphism h can be therefore considered as "renumeration" of particles at the initial position. However, this "renumeration" changes only the "label" of

the point occupying certain position in time, but the velocity, and consequently kinetic energy, at that position remains unchanged, i.e. invariant to the right translation. This property is often named "particle relabeling" symmetry.

The invariance of spatial velocity (2.63) to the right translation by (time-independent) volume-preserving diffeomorphism $h \in \text{Diff}_{\text{vol}}(\mathcal{F})$ can be shown mathematically by changing β_F with $y = \beta_F \circ h$, leading to

$$
\begin{aligned}
\boldsymbol{v} &= \frac{\partial y(y^{-1}\boldsymbol{x}, t)}{\partial t} = \dot{y} \circ y^{-1} \\
&= \frac{\partial}{\partial t}(\beta_F \circ h) \circ (\beta_F \circ h)^{-1} \\
&= \dot{\beta}_F \circ h \circ h^{-1} \circ \beta^{-1} \\
&= \dot{\beta}_F \circ \beta^{-1},
\end{aligned}
\tag{2.64}
$$

leading to the same result as (2.63), therefore proving right-invariance of ideal fluid spatial (Eulerian) velocity and, consequently, kinetic energy.

Material (Lagrangian) description of fluid motion belongs to the tangent bundle of the volume preserving diffeomorphism $(\boldsymbol{X}, \boldsymbol{V}) \in T\text{Diff}_{\text{vol}}(\mathcal{F})$, while the switch to the spatial (Eulerian) description is done by right translation, as shown in (2.62).

Coupled multibody-fluid equations of motion

3.1 Introduction

As already introduced in section 1.4, flow around flapping wings will be considered potential and incompressible, leading to the added inertia that fluid exerts on the multibody system, while viscous effects will be accounted for by modeling vortex wake, leading to external aerodynamic load on the multibody system. To this end, coupled multibody-fluid system, with the assumption of potential and incompressible fluid is first introduced from a Lie group framework perspective. This is then used to derive equations of motion for a coupled multibody-fluid system in DAE index 1 form, with description of kinematic reconstruction algorithm operating on Lie groups and pertinent Lie algebras. The resulting equations of motion take into account the often mistakenly neglected "aerodynamic load" due to the time-changing nature of added inertia.

3.2 Coupled multibody-fluid system in Lie group framework

A system of k constrained (connected by kinematic joints) rigid bodies, submerged in ideal fluid is considered. At any time t, coupled system consisting of multiple rigid bodies and ideal fluid occupies an open connected region of Euclidean space, denoted $\mathcal{M}$. If domain occupied by ith rigid body is denoted $\mathcal{B}_i$, the multibody system can be said to occupy union of individual rigid body domains as $\mathcal{B} = \bigcup\limits_{i=1}^{k} \mathcal{B}_i \subset \mathcal{M}$. If the fluid occupies a connected region $\mathcal{F} \subset \mathcal{M}$, such that the only "voids" in $\mathcal{F}$ correspond to rigid bodies, the open connected region $\mathcal{M}$ can be represented as $\mathcal{M} = \mathcal{B} \bigcup \mathcal{F} = \bigcup\limits_{i=1}^{k} \mathcal{B}_i \bigcup \mathcal{F}$.

The configuration space of the coupled system $\mathcal{Q}$ is defined as a set of all appropriately smooth mappings $\mathcal{M} \to \mathcal{M}$, corresponding to the combination of individual configuration spaces of multibody system $\mathcal{Q}_{\mathcal{B}}$ and ideal fluid $\mathcal{Q}_{\mathcal{F}}$, which will be discussed in following paragraphs.

The configuration space of ith rigid body can be represetned by $\mathcal{Q}_{\mathcal{B}_i}$, with the properties of Lie group $G_{\mathcal{B}_i} = \mathbb{R}^3 \times SO(3)$, where $\boldsymbol{x_i} \in \mathbb{R}^3$ models center of mass translation in the form of three-dimensional position vector, while $\boldsymbol{R_i} \in SO(3)$ captures rigid body rotation in the form of 3×3 orthogonal rotation matrix. Element of the rigid body configuration space (Lie group) is therefore $q_{\mathcal{B}_i} = (\boldsymbol{x_i}, \boldsymbol{R_i}) \in G_{\mathcal{B}_i}$. Identity element of the group is $e_{\mathcal{B}_i} = (\boldsymbol{0}, \boldsymbol{I})$, where $\boldsymbol{I}$ stands for 3×3 identity matrix, while the left multiplication on the group is defined as $L_q : G_{\mathcal{B}_i} \to G_{\mathcal{B}_i}, q_{\mathcal{B}_i} \to q_{\mathcal{B}_i} \cdot q$. Lie algebra (as introduced in section 2.5) of group $G_{\mathcal{B}_i}$ is defined as $g_{\mathcal{B}_i} = \mathbb{R}^3 \times so(3)$, where $\boldsymbol{v_i} \in \mathbb{R}^3$ models velocity of ith body center of mass, while $\tilde{\boldsymbol{\omega}}_{\boldsymbol{i}} \in so(3)$ represents angular velocity of ith rigid body in the form of skew-symmetric 3×3 matrix. Element of ith rigid body tangent space can therefore be defined as $v_i = (\boldsymbol{v_i}, \tilde{\boldsymbol{\omega}}_{\boldsymbol{i}}) \in g_{\mathcal{B}_i}$. State space of ith rigid body can therefore be defined as $S_i = G_{\mathcal{B}_i} \times g_{\mathcal{B}_i} = \mathbb{R}^3 \times SO(3) \times \mathbb{R}^3 \times so(3)$.

Multibody system, consisting of rigid bodies connected by kinematic constraints (joints), can be modeled in a similar framework as one rigid body. The configuration space of the whole multibody chain (with k bodies as introduced earlier) is comprised of individual rigid body configuration spaces in the form $G_{\mathcal{B}} = \prod_{i=1}^{k} G_{\mathcal{B}_i} = \mathbb{R}^3 \times SO(3) \times \cdots \times \mathbb{R}^3 \times SO(3)$, with elements in the form $q_{\mathcal{B}} = (\boldsymbol{x_1}, \boldsymbol{R_1}, \ldots, \boldsymbol{x_k}, \boldsymbol{R_k}) \in G_{\mathcal{B}}$. Configuration space $G_{\mathcal{B}}$ is also Lie group, with Lie algebra defined as $g_{\mathcal{B}} = \prod_{i=1}^{k} g_{\mathcal{B}_i} = \mathbb{R}^3 \times so(3) \times \cdots \times \mathbb{R}^3 \times so(3)$, with elements in the form $v = (\boldsymbol{v_1}, \tilde{\boldsymbol{\omega}}_{\boldsymbol{1}}, \ldots, \boldsymbol{v_k}, \tilde{\boldsymbol{\omega}}_{\boldsymbol{k}}) \in g_{\mathcal{B}}$. A multibody system state space can therefore be defined as $S_{\mathcal{B}} = G_{\mathcal{B}} \times g_{\mathcal{B}} = \prod_{i=1}^{k} G_{\mathcal{B}_i} \times \prod_{i=1}^{k} g_{\mathcal{B}_i} = \mathbb{R}^3 \times SO(3) \times \cdots \times \mathbb{R}^3 \times SO(3) \times \mathbb{R}^3 \times so(3) \times \cdots \times \mathbb{R}^3 \times so(3) \cong TG_{\mathcal{B}}$, with elements in the form $x_{\mathcal{B}} = (\boldsymbol{x_1}, \boldsymbol{R_1}, \ldots, \boldsymbol{x_k}, \boldsymbol{R_k}, \boldsymbol{v_1}, \tilde{\boldsymbol{\omega}}_{\boldsymbol{1}}, \ldots, \boldsymbol{v_k}, \tilde{\boldsymbol{\omega}}_{\boldsymbol{k}}) \in S_{\mathcal{B}}$ [41]. It is interesting to note that $S_{\mathcal{B}}$ is a Lie group itself, with Lie algebra defined as $s_{\mathcal{B}} = \prod_{i=1}^{k} g_{\mathcal{B}_i} \times \prod_{i=1}^{k} \mathbb{R}^3 = \mathbb{R}^3 \times so(3) \times \cdots \times \mathbb{R}^3 \times so(3) \times \mathbb{R}^3 \times \mathbb{R}^3 \times \cdots \times \mathbb{R}^3 \times \mathbb{R}^3$, with elements in the form $z_{\mathcal{B}} = (\boldsymbol{v_1}, \tilde{\boldsymbol{\omega}}_{\boldsymbol{1}}, \ldots, \boldsymbol{v_k}, \tilde{\boldsymbol{\omega}}_{\boldsymbol{k}}, \dot{\boldsymbol{v}}_{\boldsymbol{1}}, \dot{\boldsymbol{\omega}}_{\boldsymbol{1}}, \ldots, \dot{\boldsymbol{v}}_{\boldsymbol{k}}, \dot{\boldsymbol{\omega}}_{\boldsymbol{k}}) \in s_{\mathcal{B}}$.

As already introduced in section 2.6, configuration space of ideal fluid (fluid particles position field) is represented by volume-preserving diffeomorphism $\text{Diff}_{\text{vol}}(\mathcal{F})$, also having the properties of a Lie group. A "particle relabeling" symmetry, introduced in section 2.6

can now be utilized to perform an important reduction of the coupled system. Let $J_{\mathcal{F}}$ represent a momentum map associated with action of $\text{Diff}_{\text{vol}}(\mathcal{F})$ on configuration space $\mathcal{Q}$, which can be said to represent vorticity advection [42]. The momentum map is conserved with respect to the action, since the Lagrangian of the fluid [43] is invariant to actions of $\text{Diff}_{\text{vol}}(\mathcal{F})$, as discussed in section 2.6. This property can also be described by the fact that action of $\text{Diff}_{\text{vol}}(\mathcal{F})$ has no influence on the multibody system configuration space Lie group $G_{\mathcal{B}}$, but influences only the fluid configuration. To this end, symplectic reduction at zero vorticity results in [29, 44]

$$J_{\mathcal{F}}^{-1}\left(0\right)/\text{Diff}_{\text{vol}}\left(\mathcal{F}\right) = T^{*}\left(\mathcal{Q}/\text{Diff}_{\text{vol}}\left(\mathcal{F}\right)\right) = T^{*}G_{\mathcal{B}}, \tag{3.1}$$

indicating an important conclusion that the whole dynamics of the coupled system evolves in multibody system cotangent bundle $T^{*}G_{\mathcal{B}}$, i.e. fluid variables are reduced out, while fluid effects are accounted for solely by added inertia "felt" by the multibody system due to the environmental fluid. It is important to note that this conclusion is made for the assumption of no vorticity. However, the vorticity will be included in our analysis as previously introduced and further discussed in Chapter 5. In this case, symplectic reduction (3.1) is still valid, but is now not performed at zero vorticity level, but instead at a certain circulation momentum map level in the discretised setting [45, 44]. Since $\text{Diff}_{\text{vol}}(\mathcal{F})$ is a full symmetry Lie group, fluid variables are reduced in the same manner and Hamiltonian dynamics of the coupled system is again represented by multibody system variables only, while the vorticity (circulation) 'additional' effects are included via vector $\boldsymbol{Q_{vort}}$ [44].

3.3 Multibody system equations of motion

Let us first consider one "free" (without any kinematical constraints) rigid body, as illustrated in Fig. 2.7. As previously introduced, any point P on a rigid body can be represented as a sum of center of mass position vector and vector pointing from center of mass to point P (2.42), where all terms in the equation are expressed in spatial coordinate frame. However, the equation can be reformulated as

$$\boldsymbol{x_P} = \boldsymbol{x_C} + \boldsymbol{R}\boldsymbol{x}'_{C \to P}, \tag{3.2}$$

where $\boldsymbol{x}'_{C \to P} \in \mathbb{R}^3$ is now expressed in body-fixed reference frame, while $\boldsymbol{R} \in SO(3)$ represents rotation matrix.

Since the body is considered rigid, vector $\boldsymbol{x}'_{C \to P}$ is constant and taking derivative in time of equation (3.2) results with

$$\boldsymbol{v_P} = \boldsymbol{v_C} + \dot{\boldsymbol{R}} \boldsymbol{x}'_{C \to P}, \tag{3.3}$$

where $\boldsymbol{v_P}$ represents velocity of any point P, while $\boldsymbol{v_C}$ represents velocity of mass center.

Transforming vector $\boldsymbol{x}'_{C \to P}$ to the spatial reference frame results with

$$\boldsymbol{v_P} = \boldsymbol{v_C} + \dot{\boldsymbol{R}} \boldsymbol{R}^T \boldsymbol{x}_{C \to P}, \tag{3.4}$$

and using definition of angular velocity in spatial reference frame (2.56) results with

$$\boldsymbol{v_P} = \boldsymbol{v_C} + \tilde{\boldsymbol{\Omega}} \boldsymbol{x}_{C \to P}. \tag{3.5}$$

In order to derive equations of motion for rotation of one rigid body (denoted by subscript i), we start from the law of angular momentum conservation

$$\dot{\boldsymbol{l}}_i = \boldsymbol{t}_i, \tag{3.6}$$

where $\boldsymbol{l}_i$ represents angular momentum, while $\boldsymbol{t}_i$ represents torque vector, all expressed in spatial reference frame. Angular momentum is defined as $\boldsymbol{l}_i = \boldsymbol{J}_i \boldsymbol{\Omega}_i$, but the time-dependent inertia matrix $\boldsymbol{J}_i$ makes the calculation in this form difficult. To this end, angular momentum is usually expressed in body-fixed reference frame as $\boldsymbol{l}'_i = \boldsymbol{J}'_i \boldsymbol{\omega}_i$. Expression (3.6) can now be rewritten and expanded as

$$\frac{\mathrm{d}}{\mathrm{d}t}(\boldsymbol{R}_i \boldsymbol{l}'_i) = \boldsymbol{R}_i \boldsymbol{t}'_i,$$
$$\frac{\mathrm{d}}{\mathrm{d}t}(\boldsymbol{R}_i \boldsymbol{J}'_i \boldsymbol{\omega}_i) = \boldsymbol{R}_i \boldsymbol{t}'_i,$$
$$\dot{\boldsymbol{R}}_i \boldsymbol{J}'_i \boldsymbol{\omega}_i + \boldsymbol{R}_i \boldsymbol{J}'_i \dot{\boldsymbol{\omega}}_i = \boldsymbol{R}_i \boldsymbol{t}'_i, \tag{3.7}$$

and multiplication of the equation from the left side with $\boldsymbol{R}_i^T$ and applying equation (2.57)

results with

$$\boldsymbol{R}_i^T \dot{\boldsymbol{R}}_i \boldsymbol{J}_i' \boldsymbol{\omega}_i + \boldsymbol{R}_i^T \boldsymbol{R}_i \boldsymbol{J}_i' \dot{\boldsymbol{\omega}}_i = \boldsymbol{R}_i^T \boldsymbol{R}_i \boldsymbol{t}_i',$$

$$\boldsymbol{J}_i' \dot{\boldsymbol{\omega}}_i + \tilde{\boldsymbol{\omega}}_i \boldsymbol{J}_i' \boldsymbol{\omega}_i = \boldsymbol{t}_i'. \tag{3.8}$$

In addition to this, Newton's equations of motion govern the translational dynamics of "free" rigid body in the form

$$\dot{\boldsymbol{p}}_i = \boldsymbol{f}_i$$

$$m_i \dot{\boldsymbol{v}}_i = \boldsymbol{f}_i, \tag{3.9}$$

where $\boldsymbol{p_i}$ represents linear momentum of rigid body i, $\boldsymbol{f}_i$ represents force acting on the body and m_i stands for rigid body mass. Expressions (3.8) and (3.9) represent set of ordinary differential equations (ODE), that can be solved for $\boldsymbol{v_i}$ and $\tilde{\boldsymbol{\omega}}_i$ to obtain velocity field of single "free" rigid body.

If k rigid bodies are considered, with the assumption of no constraints still valid, motion equations can be expressed in matrix form as

$$\boldsymbol{M}\dot{\boldsymbol{v}} = \boldsymbol{Q}, \tag{3.10}$$

where $\boldsymbol{M}$ represents inertia matrix, $\boldsymbol{v}$ is a set of all (both translation and rotation) velocities, while $\boldsymbol{Q}$ is generalized "load" vector, which also includes the effects of expressing equations in rotational (body-fixed) reference frame. Individual terms are equal to

$$\boldsymbol{M} = \begin{pmatrix} m_1 \boldsymbol{I_{3\times 3}} & \boldsymbol{0} & \boldsymbol{0} & \boldsymbol{0} & \ldots & \boldsymbol{0} & \boldsymbol{0} \\ \boldsymbol{0} & \boldsymbol{J_1'} & \boldsymbol{0} & \boldsymbol{0} & \ldots & \boldsymbol{0} & \boldsymbol{0} \\ \boldsymbol{0} & \boldsymbol{0} & m_2 \boldsymbol{I_{3\times 3}} & \boldsymbol{0} & \ldots & \boldsymbol{0} & \boldsymbol{0} \\ \boldsymbol{0} & \boldsymbol{0} & \boldsymbol{0} & \boldsymbol{J_2'} & \ldots & \boldsymbol{0} & \boldsymbol{0} \\ \vdots & \vdots & \vdots & \vdots & \ddots & \vdots & \vdots \\ \boldsymbol{0} & \boldsymbol{0} & \boldsymbol{0} & \boldsymbol{0} & \cdots & m_k \boldsymbol{I_{3\times 3}} & \boldsymbol{0} \\ \boldsymbol{0} & \boldsymbol{0} & \boldsymbol{0} & \boldsymbol{0} & \cdots & \boldsymbol{0} & \boldsymbol{J_k'} \end{pmatrix}, \tag{3.11}$$

$$\boldsymbol{v} = \begin{pmatrix} v_1 \\ \omega_1 \\ v_2 \\ \omega_2 \\ \vdots \\ v_k \\ \omega_k \end{pmatrix}, \tag{3.12}$$

$$\boldsymbol{Q} = \boldsymbol{Q}_F - \boldsymbol{Q}_{vel}, \tag{3.13}$$

$$\boldsymbol{Q}_F = \begin{pmatrix} f_1 \\ t_1 \\ f_2 \\ t_2 \\ \vdots \\ f_k \\ t_k \end{pmatrix}, \qquad \boldsymbol{Q}_{vel} = \begin{pmatrix} 0 \\ \tilde{\omega}_1 J_1' \omega_1 \\ 0 \\ \tilde{\omega}_2 J_2' \omega_2 \\ \vdots \\ 0 \\ \tilde{\omega}_k J_k' \omega_k \end{pmatrix}. \tag{3.14}$$

At this point, previously introduced k rigid bodies are constrained by m kinematical constraints in the form of functions

$$\boldsymbol{g}(\boldsymbol{x}, \boldsymbol{t}) = \boldsymbol{0} \tag{3.15}$$

depending only on positions $\boldsymbol{x}$ (translational position of mass centers and orientation of rigid bodies) and time t, i.e. holonomic constraints, as introduced in section 2.2. Derivative of constraint equations with respect to time results with

$$\frac{\mathrm{d}\boldsymbol{g}(\boldsymbol{x}, \boldsymbol{t})}{\mathrm{d}t} = \boldsymbol{0}$$
$$\frac{\partial \boldsymbol{g}}{\partial \boldsymbol{x}} \boldsymbol{v} + \frac{\partial \boldsymbol{g}}{\partial t} = \boldsymbol{0}$$
$$\boldsymbol{C}\boldsymbol{v} = -\frac{\partial \boldsymbol{g}}{\partial t}, \tag{3.16}$$

where $\boldsymbol{C}$ represents constraint $m \times 6k$ dimensional Jacobian matrix. Resulting constraint forces and torques can now be represented in the form of Lagrange multipliers as $\boldsymbol{C}^T \boldsymbol{\lambda}$, where $\boldsymbol{\lambda}$ represents vector of Lagrangian multipliers, resulting in the Newton-Euler equation

for constrained multibody system

$$\boldsymbol{M}\dot{\boldsymbol{v}} + \boldsymbol{C}^T\boldsymbol{\lambda} = \boldsymbol{Q}. \tag{3.17}$$

Although not necessary, further analysis will be limited to the scleronomous constraints, i.e. constraints not explicitly depending on time t. Rheonomous constraints can be conventionally introduced by expanding equations in a straightforward manner, but here this discussion is omitted for the sake of clarity and because implemented numerical examples include scleronomous constraints only.

Scleronomous onstraint mapping $\boldsymbol{g}(\boldsymbol{x}) : G_{\mathcal{B}} \to \mathbb{R}^m$ imposes geometric constraints on the configuration space $G_{\mathcal{B}}$. Therefore, multibody system can be said to evolve on $(6k-m)$-dimensional sub-manifold, defined as $\mathcal{N} = \{\boldsymbol{x} \in G_{\mathcal{B}} : \boldsymbol{g} = \boldsymbol{0}\}$. The unconstrained configuration space of multibody system $G_{\mathcal{B}}$ is sometimes named ambient configuration space [46].

In order to formulate a (differential algebraic equations) DAE system of index 1, equation (3.16) (with $\frac{\partial \boldsymbol{g}}{\partial t} = \boldsymbol{0}$ because of scleronomous constraint assumption) is differentiated again with respect to time, resulting with contraint equation at acceleration level

$$\boldsymbol{C}(\boldsymbol{x})\dot{\boldsymbol{v}} = \boldsymbol{\zeta}(\boldsymbol{x}, \boldsymbol{v}). \tag{3.18}$$

DAE index 1 system of equations in matrix form can now be formulated as

$$\begin{pmatrix} \boldsymbol{M} & \boldsymbol{C}^T \\ \boldsymbol{C} & \boldsymbol{0} \end{pmatrix} \begin{pmatrix} \dot{\boldsymbol{v}} \\ \boldsymbol{\lambda} \end{pmatrix} = \begin{pmatrix} \boldsymbol{Q} \\ \boldsymbol{\zeta} \end{pmatrix}. \tag{3.19}$$

System (3.19) can be solved for $\dot{\boldsymbol{v}}$ and then kinematic reconstruction on $S_{\mathcal{B}} = G_{\mathcal{B}} \times g_{\mathcal{B}}$ can be performed by utilization of Munthe-Kaas type of ODE integrators [47] (discussed in subsequent section). However, the position constraints (3.15) are included in dynamical equations at the acceleration level, while the constraint equations should also be satisfied at both position and velocity level (well-researched issue of constraint drift, discussed in [48, 49, 50]). The constraint equation at position and velocity level are often denoted hidden constraints, because they do not appear in the system (3.19) directly, but should be satisfied by utilizing dedicated techniques, often called constraint stabilization procedures.

The constraint equations at acceleration level are, of course, satisfied during (3.19) solving, because they are explicitly included in the system.

3.4 Kinematic reconstruction of position and orientation from velocity field

Solving a DAE index 1 system of equations (3.19), results with the acceleration field (both translational and angular acceleration). This can be further integrated - basically with any vector-based method for ordinary differential equations (ODE), such as Runge Kutta for example - together with the constraint stabilization on velocity level (3.16) to obtain velocity field. Kinematical reconstruction is then required to obtain positions and orientations of rigid bodies in the multibody system.

Reconstruction of positions is a straightforward task, performed again by integration with any vector-based ODE solver, together with enforcing constraints at the position level (3.15), since position of ith rigid body is actually represented by a vector in Euclidean space $\boldsymbol{v_i} \in \mathbb{R}^3$.

On the other hand, reconstruction of orientation is a more involving task since, as already introduced in section 2.5, three dimensional rotation is not a vector, but a more nonlinear manifold, i.e. rotation (orientation) matrix of ith rigid body belongs to the special orthogonal group $\boldsymbol{R_i} \in SO(3)$ (most rigorously, it belongs to Lie group, see Chapter 2). Because of this, a conventional ODE integrators would introduce errors in the structure of the rotation matrices, i.e. rotation matrix would "loose" orthogonality property very soon during integration process if conventional vector space based solver (such as Runge Kutta) is used. This could of course be "repaired" by a stabilization algorithm, artificially enforcing matrix orthogonality, but this approach results with six non-trivial algebraic equations for each rigid body, that would lead to the unnecessary complications and inefficiencies in the algorithm (although some authors in recent liretature advocate this approach [51, 52]).

As opposed to the conventional approach, including solution with standard vector-based ODE solvers, the solution of kinematic reconstruction for ith rigid body is expressed, following a theorem by Magnus [53], in the form

$$\boldsymbol{R}(t) = \boldsymbol{R}(0)\exp(\tilde{\boldsymbol{u}}(t)), \tag{3.20}$$

where exp represents the exponential mapping operator, while $\boldsymbol{u}(t) \in \mathbb{R}^3$ represents an instantaneous rotation vector at time t given in its skew-symmetric form, as an element of the pertinent Lie algebra $\tilde{\boldsymbol{u}} \in so(3)$. This vector could also be called scaled rotation vector, distinguishing this representation from the classical description of axis-angle parameters with unit vector and angle, while here the angle is represented by the norm of the instantaneous rotation vector $\phi_{rot} = \|\boldsymbol{u}\|$.

It can be shown that the exponential mapping for rigid body kinematic reconstruction, introduced in (3.20) is equivalent to the Rodrigues formula [54] and can be formulated as [55]

$$\exp(\tilde{\boldsymbol{u}}) = \boldsymbol{I}_{3\times3} + \frac{\sin(\|\boldsymbol{u}\|)}{\|\boldsymbol{u}\|}\tilde{\boldsymbol{u}} + \frac{1 - \cos(\|\boldsymbol{u}\|)}{\|\boldsymbol{u}\|^2}\tilde{\boldsymbol{u}}^2. \tag{3.21}$$

Pertinent to the Munthe-Kaas Lie group numerical method (basically Runge Kutta algorithm based method but designed to operate in Lie groups instead of vector spaces), described in detail in [56, 53, 47], scaled instantaneous vector $\boldsymbol{u}$ can be defined as a solution to the following ODE system

$$\dot{\tilde{\boldsymbol{u}}} = \mathrm{dexp}_{-\tilde{\boldsymbol{u}}}^{-1}(\tilde{\boldsymbol{\omega}}), \quad \tilde{\boldsymbol{u}}_0 = \boldsymbol{0}, \tag{3.22}$$

where dexp represents a differential of the exponential mapping introduced in (3.20), which can be defined as [57]

$$\mathrm{dexp}_{-\tilde{\boldsymbol{u}}}^{-1}(\tilde{\boldsymbol{\omega}}) = \tilde{\boldsymbol{\omega}} + \frac{1}{2}\left[\tilde{\boldsymbol{u}}, \tilde{\boldsymbol{\omega}}\right] + \frac{1}{12}\left[\tilde{\boldsymbol{u}}, \left[\tilde{\boldsymbol{u}}, \tilde{\boldsymbol{\omega}}\right]\right] + \cdots = \tilde{\boldsymbol{\omega}} + \sum_{j=1}^{\infty}(-1)^j\frac{B_j}{j!}\mathrm{ad}_{\tilde{\boldsymbol{u}}}^j(\tilde{\boldsymbol{\omega}}), \tag{3.23}$$

where B_j represents jth Bernoulli number [56], while 'ad' represents an adjoint operator, corresponding to the Lie bracket $[\cdot, \cdot]$ (introduced in section 2.4.1), such that for any $\tilde{\boldsymbol{u}}, \tilde{\boldsymbol{v}} \in so(3)$ adjoint operator results with

$$\tilde{\boldsymbol{w}} = \mathrm{ad}_{\tilde{\boldsymbol{u}}}(\tilde{\boldsymbol{v}}) = [\tilde{\boldsymbol{u}}, \tilde{\boldsymbol{v}}] = \tilde{\boldsymbol{u}}\tilde{\boldsymbol{v}} - \tilde{\boldsymbol{v}}\tilde{\boldsymbol{u}}, \tag{3.24}$$

where resulting $\tilde{\boldsymbol{w}}$ is also element of $so(3)$, since

$$\tilde{\boldsymbol{w}}^T = (\tilde{\boldsymbol{u}}\tilde{\boldsymbol{v}} - \tilde{\boldsymbol{v}}\tilde{\boldsymbol{u}})^T = \tilde{\boldsymbol{v}}^T\tilde{\boldsymbol{u}}^T - \tilde{\boldsymbol{u}}^T\tilde{\boldsymbol{v}}^T$$

$$= \tilde{\boldsymbol{v}}\tilde{\boldsymbol{u}} - \tilde{\boldsymbol{u}}\tilde{\boldsymbol{v}} = -(\tilde{\boldsymbol{u}}\tilde{\boldsymbol{v}} - \tilde{\boldsymbol{v}}\tilde{\boldsymbol{u}}) = -\tilde{\boldsymbol{w}}, \tag{3.25}$$

therefore proving that $\tilde{\boldsymbol{w}} \in so(3)$.

Importantly, there is also a closed-form solution for the series (3.23) resulting in [57]

$$\mathrm{dexp}^{-1}_{-\tilde{\boldsymbol{u}}}(\tilde{\boldsymbol{\omega}}) = \tilde{\boldsymbol{\omega}} + \frac{1}{2}\tilde{\boldsymbol{u}}\tilde{\boldsymbol{\omega}} - \frac{\|\boldsymbol{u}\| \cot\left(\frac{\|\boldsymbol{u}\|}{2}\right) - 2}{2\|\boldsymbol{u}\|^2}\tilde{\boldsymbol{u}}^2\tilde{\boldsymbol{\omega}}. \tag{3.26}$$

The underlying differential equation (3.22) can be solved with any vector space based ODE solver and the overall method order of accuracy will be depending directly on the order of accuracy of the method utilized for solving (3.22). Interestingly, it can be shown [53, 58] that if ODE solver used is of order p it enough to use $\geq p - 2$ number of elements in the sum on the right hand side of (3.23), in order to keep the order of accuracy p. Therefore, if 2nd order accuracy method is to be used, it is enough to set the derivative of scaled instantaneous rotation vector to be equal to the angular velocity of the rigid body, expressed in body-fixed reference frame, i.e. $\dot{\tilde{\boldsymbol{u}}} = \mathrm{dexp}^{-1}_{-\tilde{\boldsymbol{u}}}(\tilde{\boldsymbol{\omega}}) = \tilde{\boldsymbol{\omega}}$.

This defines everything needed to formulate an algorithm for kinematic reconstruction of rigid body rotation from a given velocity field. One time step of the algorithm (starting from ith time step), based on fourth order Runge Kutta method as an ODE solver for (3.22) can be represented as

$$\boldsymbol{k_1} = \Delta t \cdot \mathrm{dexp}^{-1}_{\boldsymbol{0}}(\tilde{\boldsymbol{\omega}}_i)$$

$$\boldsymbol{K_1} = \Delta t \cdot f(t_i)$$

$$\boldsymbol{k_2} = \Delta t \cdot \mathrm{dexp}^{-1}_{-\frac{1}{2}\boldsymbol{k_1}}\left(\tilde{\boldsymbol{\omega}}_i + \frac{1}{2}\boldsymbol{K_1}\right)$$

$$\boldsymbol{K_2} = \Delta t \cdot f\left(t_i + \frac{1}{2}\Delta t\right)$$

$$\boldsymbol{k_3} = \Delta t \cdot \mathrm{dexp}^{-1}_{-\frac{1}{2}\boldsymbol{k_2}}\left(\tilde{\boldsymbol{\omega}}_i + \frac{1}{2}\boldsymbol{K_2}\right)$$

$$\boldsymbol{K_3} = \Delta t \cdot f\left(t_i + \frac{1}{2}\Delta t\right)$$

$$\boldsymbol{k_4} = \Delta t \cdot \mathrm{dexp}^{-1}_{-\boldsymbol{k_2}}(\tilde{\boldsymbol{\omega}}_i + \boldsymbol{K_3})$$

$$\boldsymbol{K_4} = \Delta t \cdot f(t_i + \Delta t)$$

$$\boldsymbol{\omega}_{i+1} = \boldsymbol{\omega}_i + \frac{1}{6}(\boldsymbol{K_1} + 2\boldsymbol{K_2} + 2\boldsymbol{K_3} + \boldsymbol{K_4})$$

$$\boldsymbol{R}_{i+1} = \boldsymbol{R}_i \cdot \exp\left(\frac{1}{6}(\boldsymbol{k_1} + 2\boldsymbol{k_2} + 2\boldsymbol{k_3} + \boldsymbol{k_4})\right)$$

where $f(t_i)$ represents the function for calculating angular velocity derivative at time step t_i, i.e. a solution to the Euler's rotational dynamics equation, such as (3.19).

This update can also be illustrated in the form of "lifting" from the manifold to tangent space, making an update on the Lie algebra and "pulling back" to the manifold, as shown in Fig. 3.1.

3.5 Equations of motion for the coupled mutibody-fluid system

Up until this point, multibody system dynamics and kinematics are analyzed as if evolving in vacuum. As already introduced, symplectic reduction of ideal fluid (3.1) allows for exclusion of fluid variables from the model and coupled system dynamics evolves in multibody system cotangent bundle $T^*G_{\mathcal{B}}$, while the fluid influence on the coupled system motion is modeled by added inertia effects.

However, it is important to note that the added inertia, due to the effects of the ideal fluid on multibody system, is not constant in general (as opposed to the standard rigid body inertia) and the overall inertia matrix "felt" by the multibody system can be expressed as

$$\boldsymbol{M} = \boldsymbol{M_B} + \boldsymbol{M_F}(t), \tag{3.27}$$

with $\boldsymbol{M_B}$ representing a block matrix with masses and inertia matrices of multibody system rigid bodies as diagonal block elements, expressed in body-fixed reference frame, while $\boldsymbol{M_F}(t)$ represents added inertia matrix, capturing all effects of ideal fluid on the multibody system.

Multibody system inertia matrix, expressed in the body-fixed reference frame, can be expressed in block matrix form as

$$\boldsymbol{M_B} = \begin{pmatrix} m_1\boldsymbol{I}_{3\times3} & 0 & 0 & 0 & \cdots & 0 & 0 \\ 0 & \boldsymbol{J_1} & 0 & 0 & \cdots & 0 & 0 \\ 0 & 0 & m_1\boldsymbol{I}_{3\times3} & 0 & \cdots & 0 & 0 \\ 0 & 0 & 0 & \boldsymbol{J_2} & \cdots & 0 & 0 \\ \vdots & \vdots & \vdots & \vdots & \ddots & \vdots & \vdots \\ 0 & 0 & 0 & 0 & \cdots & m_k\boldsymbol{I}_{3\times3} & 0 \\ 0 & 0 & 0 & 0 & \cdots & 0 & \boldsymbol{J_k} \end{pmatrix}, \tag{3.28}$$

where m_i represents mass of the ith rigid body, while $\boldsymbol{J_i}$ represents inertia of ith body, expressed in body-fixed reference frame.

Elements of matrix $\boldsymbol{M_F}(t)$ in each time step are calculated by boundary element method, as described in Chapter 4. The fact that the added inertia matrix is time-dependent should be taken into account when deriving coupled system equations of motion, while it is often neglected in the literature.

The added inertia matrix for a multibody system, with k bodies submerged in fluid can be represented by a block inertia matrix in the form

$$\boldsymbol{M_F} = \begin{pmatrix} m_f^{v_1 v_1} & m_f^{v_1 \omega_1} & m_f^{v_1 v_2} & m_f^{v_1 \omega_2} & \cdots & m_f^{v_1 v_k} & m_f^{v_1 \omega_k} \\ m_f^{\omega_1 v_1} & m_f^{\omega_1 \omega_1} & m_f^{\omega_1 v_2} & m_f^{\omega_1 \omega_2} & \cdots & m_f^{\omega_1 v_k} & m_f^{\omega_1 \omega_k} \\ m_f^{v_2 v_1} & m_f^{v_2 \omega_1} & m_f^{v_2 v_2} & m_f^{v_2 \omega_2} & \cdots & m_f^{v_2 v_k} & m_f^{v_2 \omega_k} \\ m_f^{\omega_2 v_1} & m_f^{\omega_2 \omega_1} & m_f^{\omega_2 v_2} & m_f^{\omega_2 \omega_2} & \cdots & m_f^{\omega_2 v_k} & m_f^{\omega_2 \omega_k} \\ \vdots & \vdots & \vdots & \vdots & \ddots & \vdots & \vdots \\ m_f^{v_k v_1} & m_f^{v_k \omega_1} & m_f^{v_k v_2} & m_f^{v_k \omega_2} & \cdots & m_f^{v_k v_k} & m_f^{v_k \omega_k} \\ m_f^{\omega_k v_1} & m_f^{\omega_k \omega_1} & m_f^{\omega_k v_2} & m_f^{\omega_k \omega_2} & \cdots & m_f^{\omega_k v_k} & m_f^{\omega_k \omega_k} \end{pmatrix}, \tag{3.29}$$

where individual block matrix elements correspond to the added inertia in the "direction" of first superscript, due to the motion in direction of second superscript - this will be discussed in detail in Chapter 4.

Defining a linear and angular momenutm for the coupled multibody-fluid system is not a trivial task to the infinite domain of the surrounding fluid. However, Lord Kelvin introduced concepts of linear and angular impulse of the coupled system [59], which is not equivalent to the coupled system momentum, but varies under external load in the same way the momentum does, i.e.

$$\frac{\mathrm{d}\boldsymbol{\Pi}}{\mathrm{d}t} = \boldsymbol{Q}_{spatial}, \tag{3.30}$$

where $\boldsymbol{\Pi}$ represents total coupled system impulse, while $\boldsymbol{Q}_{spatial}$ represents total applied load (forces and torques), expressed in spatial coordinate frame.

Total impulse of the coupled system can be defined as

$$\boldsymbol{\Pi} = \boldsymbol{M}_{inertial}\boldsymbol{V}, \tag{3.31}$$

where $\boldsymbol{M}$ represents overall inertia of the multibody system expressed in the inertial (spa-

tial or fixed) reference frame, while $\boldsymbol{V} = \begin{pmatrix} \boldsymbol{v}_1^T & \boldsymbol{\omega}_1^T & \boldsymbol{v}_2^T & \boldsymbol{\omega}_2^T & \cdots & \boldsymbol{v}_k^T & \boldsymbol{\omega}_k^T \end{pmatrix}^T$ represents linear and angular velocities of the multibody system. Total impulse $\boldsymbol{\Pi}$ represents both linear and angular impulses of the coupled system.

Expression (3.31) can be further rewritten by including (3.28) and (3.29) as

$$
\boldsymbol{\Pi} = \begin{pmatrix}
\boldsymbol{R_1} \left(m_1 \boldsymbol{v_1} + \sum_{i=1}^k \left(\boldsymbol{m}_f^{v_1 v_i} \boldsymbol{v}_i + \boldsymbol{m}_f^{v_1 \omega_i} \boldsymbol{\omega}_i \right) \right) \\
\boldsymbol{R_1} \left(\boldsymbol{J_1} \boldsymbol{\omega_1} + \sum_{i=1}^k \left(\boldsymbol{m}_f^{\omega_1 v_i} \boldsymbol{v}_i + \boldsymbol{m}_f^{\omega_1 \omega_i} \boldsymbol{\omega}_i \right) \right) \\
\boldsymbol{R_2} \left(m_2 \boldsymbol{v_2} + \sum_{i=1}^k \left(\boldsymbol{m}_f^{v_2 v_i} \boldsymbol{v}_i + \boldsymbol{m}_f^{v_2 \omega_i} \boldsymbol{\omega}_i \right) \right) \\
\boldsymbol{R_2} \left(\boldsymbol{J_2} \boldsymbol{\omega_2} + \sum_{i=1}^k \left(\boldsymbol{m}_f^{\omega_2 v_i} \boldsymbol{v}_i + \boldsymbol{m}_f^{\omega_2 \omega_i} \boldsymbol{\omega}_i \right) \right) \\
\cdots \\
\boldsymbol{R_k} \left(m_k \boldsymbol{v_k} + \sum_{i=1}^k \left(\boldsymbol{m}_f^{v_k v_i} \boldsymbol{v}_i + \boldsymbol{m}_f^{v_k \omega_i} \boldsymbol{\omega}_i \right) \right) \\
\boldsymbol{R_k} \left(\boldsymbol{J_k} \boldsymbol{\omega_k} + \sum_{i=1}^k \left(\boldsymbol{m}_f^{\omega_k v_i} \boldsymbol{v}_i + \boldsymbol{m}_f^{\omega_k \omega_i} \boldsymbol{\omega}_i \right) \right)
\end{pmatrix}. \tag{3.32}
$$

Taking a differential with respect to t of (3.32) results in (separated by matrix block rows for readability, i.e. $\boldsymbol{\Pi_i}$ represents ith block row of total impulse (3.32))

$$
\frac{\mathrm{d}\boldsymbol{\Pi_1}}{\mathrm{d}t} = \dot{\boldsymbol{R_1}} \left(m_1 \boldsymbol{v_1} + \sum_{i=1}^k \left(\boldsymbol{m}_f^{v_1 v_i} \boldsymbol{v}_i + \boldsymbol{m}_f^{v_1 \omega_i} \boldsymbol{\omega}_i \right) \right)
$$
$$
+ \boldsymbol{R_1} \left(m_1 \dot{\boldsymbol{v_1}} + \sum_{i=1}^k \left(\dot{\boldsymbol{m}}_f^{v_1 v_i} \boldsymbol{v}_i + \boldsymbol{m}_f^{v_1 v_i} \dot{\boldsymbol{v}}_i + \dot{\boldsymbol{m}}_f^{v_1 \omega_i} \boldsymbol{\omega}_i + \boldsymbol{m}_f^{v_1 \omega_i} \dot{\boldsymbol{\omega}}_i \right) \right)
$$
$$
\frac{\mathrm{d}\boldsymbol{\Pi_2}}{\mathrm{d}t} = \dot{\boldsymbol{R_1}} \left(\boldsymbol{J_1} \boldsymbol{\omega_1} + \sum_{i=1}^k \left(\boldsymbol{m}_f^{\omega_1 v_i} \boldsymbol{v}_i + \boldsymbol{m}_f^{\omega_1 \omega_i} \boldsymbol{\omega}_i \right) \right)
$$
$$
+ \boldsymbol{R_1} \left(\boldsymbol{J_1} \dot{\boldsymbol{\omega_1}} + \sum_{i=1}^k \left(\dot{\boldsymbol{m}}_f^{\omega_1 v_i} \boldsymbol{v}_i + \boldsymbol{m}_f^{\omega_1 v_i} \dot{\boldsymbol{v}}_i + \dot{\boldsymbol{m}}_f^{\omega_1 \omega_i} \boldsymbol{\omega}_i + \boldsymbol{m}_f^{\omega_1 \omega_i} \dot{\boldsymbol{\omega}}_i \right) \right)
$$
$$
\vdots
$$
$$
\frac{\mathrm{d}\boldsymbol{\Pi_{2k-1}}}{\mathrm{d}t} = \dot{\boldsymbol{R_k}} \left(m_k \boldsymbol{v_k} + \sum_{i=k}^k \left(\boldsymbol{m}_f^{v_k v_i} \boldsymbol{v}_i + \boldsymbol{m}_f^{v_k \omega_i} \boldsymbol{\omega}_i \right) \right)
$$
$$
+ \boldsymbol{R_k} \left(m_k \dot{\boldsymbol{v_k}} + \sum_{i=k}^k \left(\dot{\boldsymbol{m}}_f^{v_k v_i} \boldsymbol{v}_i + \boldsymbol{m}_f^{v_k v_i} \dot{\boldsymbol{v}}_i + \dot{\boldsymbol{m}}_f^{v_k \omega_i} \boldsymbol{\omega}_i + \boldsymbol{m}_f^{v_k \omega_i} \dot{\boldsymbol{\omega}}_i \right) \right)
$$
$$
\frac{\mathrm{d}\boldsymbol{\Pi_{2k}}}{\mathrm{d}t} = \dot{\boldsymbol{R_k}} \left(\boldsymbol{J_k} \boldsymbol{\omega_k} + \sum_{i=k}^k \left(\boldsymbol{m}_f^{\omega_k v_i} \boldsymbol{v}_i + \boldsymbol{m}_f^{\omega_k \omega_i} \boldsymbol{\omega}_i \right) \right)
$$
$$
+ \boldsymbol{R_k} \left(\boldsymbol{J_k} \dot{\boldsymbol{\omega_k}} + \sum_{i=k}^k \left(\dot{\boldsymbol{m}}_f^{\omega_k v_i} \boldsymbol{v}_i + \boldsymbol{m}_f^{\omega_k v_i} \dot{\boldsymbol{v}}_i + \dot{\boldsymbol{m}}_f^{\omega_k \omega_i} \boldsymbol{\omega}_i + \boldsymbol{m}_f^{\omega_k \omega_i} \dot{\boldsymbol{\omega}}_i \right) \right). \tag{3.33}
$$

The equations of motion for the first block row can now be derived from (3.30) and (3.33), after multiplying equation from the left by pertinent rotation matrix transpose $\boldsymbol{R_1^T}$

$$
\boldsymbol{R_1^T \dot{R}_1} \left(m_1 \boldsymbol{v_1} + \sum_{i=1}^{k} \left(\boldsymbol{m_f^{v_1 v_i} v_i} + \boldsymbol{m_f^{v_1 \omega_i} \omega_i} \right) \right)
$$

$$
+ \left(m_1 \boldsymbol{\dot{v}_1} + \sum_{i=1}^{k} \left(\boldsymbol{\dot{m}_f^{v_1 v_i} v_i} + \boldsymbol{m_f^{v_1 v_i} \dot{v}_i} + \boldsymbol{\dot{m}_f^{v_1 \omega_i} \omega_i} + \boldsymbol{m_f^{v_1 \omega_i} \dot{\omega}_i} \right) \right) = \boldsymbol{Q_{ext,1}}
$$

$$
\left(m_1 + \sum_{i=1}^{k} \boldsymbol{m_f^{v_1 v_i}} \right) \boldsymbol{\dot{v}_1} + \sum_{i=1}^{k} \boldsymbol{m_f^{v_1 \omega_i} \dot{\omega}_i}
$$

$$
+ \boldsymbol{\tilde{\omega}_1} \left(m_1 \boldsymbol{v_1} + \sum_{i=1}^{k} \left(\boldsymbol{m_f^{v_1 v_i} v_i} + \boldsymbol{m_f^{v_1 \omega_i} \omega_i} \right) \right) +
$$

$$
+ \sum_{i=1}^{k} \left(\boldsymbol{\dot{m}_f^{v_1 v_i} v_i} + \boldsymbol{m_f^{v_1 v_i} \dot{v}_i} + \boldsymbol{\dot{m}_f^{v_1 \omega_i} \omega_i} \right) = \boldsymbol{Q_{ext,1}}
$$

$$
\left(m_1 + \sum_{i=1}^{k} \boldsymbol{m_f^{v_1 v_i}} \right) \boldsymbol{\dot{v}_1} + \sum_{i=1}^{k} \boldsymbol{m_f^{v_1 \omega_i} \dot{\omega}_i} + \boldsymbol{Q_{vel,1}} + \boldsymbol{Q_{AM,1}} = \boldsymbol{Q_{ext,1}}. \tag{3.34}
$$

Equivalent derivation can be made for other block rows, leading to the equations of motion for the unconstrained multibody system submerged in the ideal fluid

$$
\boldsymbol{M\dot{v}} = \boldsymbol{Q_{ext}} - \boldsymbol{Q_{vel}} - \boldsymbol{Q_{AM}}, \tag{3.35}
$$

where, as already introduced and demonstrated in (3.34) for first block row, $\boldsymbol{Q_{ext}}$ represents general external forces and torques acting on the body (in extended Kirchoff equations [59]), $\boldsymbol{Q_{vel}}$ represents "load" resulting from expressing equations in rotating body-fixed reference frame, while $\boldsymbol{Q_{AM}}$ represents "load" due to the added inertia time-dependence. All quantities are expressed in body-fixed reference frame.

As already mentioned, the vorticity effects will be introduced in the model in the form of external forces and torques (represented here by $\boldsymbol{Q_{vort}}$), leading to the final equations of motion for unconstrained coupled system

$$
\boldsymbol{M\dot{v}} = \boldsymbol{Q_{ext}} + \boldsymbol{Q_{vort}} - \boldsymbol{Q_{vel}} - \boldsymbol{Q_{AM}}. \tag{3.36}
$$

Introduction of kinematic constraints results in the same equations of motion system as introduced in (3.19), with the differences in inertia matrix and force vector. Inertia matrix now consists of body inertia, together with added inertia "felt" by the multibody

system due to the surrounding fluid (3.27). The force vector $\boldsymbol{Q}$ in (3.19) now consists of multiple elements and can be expressed in the form

$$\boldsymbol{Q} = \boldsymbol{Q}_{ext} + \boldsymbol{Q}_{vort} - \boldsymbol{Q}_{vel} - \boldsymbol{Q}_{AM}. \qquad (3.37)$$

Subsequent chapters will introduce the approaches to modeling added inertia matrix and vorticity force vector.
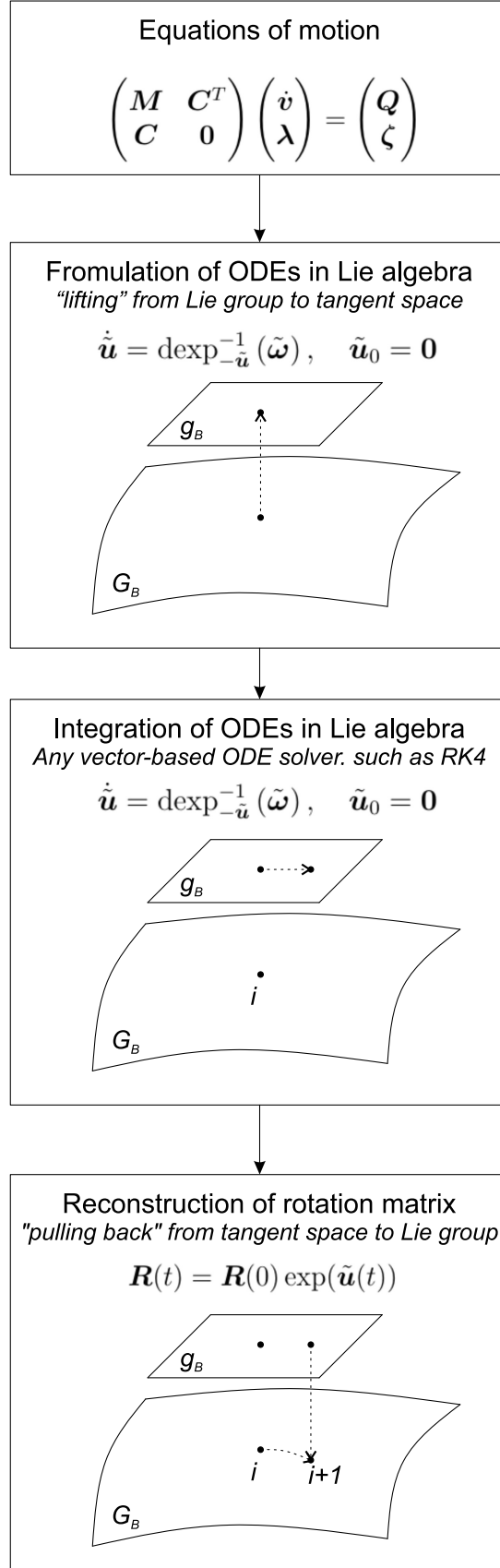
Figure 3.1: Illustration of the algorithm for kinematic reconstruction of orientation (rotation matrix) from the angular velocity field, operating in Lie algebra, i.e. tangent space of the rigid body Lie group.

Added inertia

4.1 Introduction

As already introduced in section 1.4, added inertia effects are important for an insect-type flapping flight modeling due to the high accelerations involved and highly complex wing kinematics. Proposed approach takes into account coupling effects, while also modeling exact body shapes, opposed to the conventional low and mid-fidelity flapping wing aerodynamics modeling approaches, usually capturing added inertia effects with simple algebraic terms either neglecting phenomena important for flapping wing aerodynamics or requiring experimental results. The equations of motion for coupled system, involving added inertia are derived in Chapter 3, while this chapter focuses on calculation of the added inertia effects for a given configuration and kinematics of multibody system, as well as fluid density. This includes formulating the problem in the form of a set of exterior Laplace boundary value problems, as well as description of collocation boundary element method used for solving resulting boundary value problems.

4.2 Lagrangian of the coupled multibody-fluid system

Lagrangian function, introduced in section 2.2, of the coupled system of rigid bodies and ideal fluid is equal to total kinetic energy of the system if no external forces and torques are imposed, i.e.

$$\mathcal{L}_S = T_{\mathcal{F}} + \sum_{i=1}^{N} T_{\mathcal{B}_i}, \tag{4.1}$$

where $T_{\mathcal{F}}$ represents kinetic energy of the fluid, while $T_{\mathcal{B}_i}$ stands for kinetic energy of ith body.

Kinetic energy of the homogeneous fluid can be expressed as

$$T_{\mathcal{F}} = \frac{1}{2}\rho_{\mathcal{F}} \int_{\mathcal{F}} \|\boldsymbol{u}\|^2 \, \mathrm{d}V, \tag{4.2}$$

where $\rho_{\mathcal{F}}$ represents fluid density, while $\boldsymbol{u}$ represents fluid velocity vector.

If the fluid is considered potential, as indicated in [29], the fluid velocity u can be expressed as gradient of the potential function ϕ

$$\boldsymbol{u} = \nabla\phi. \tag{4.3}$$

Combining equations (4.2) and (4.3) leads to

$$\begin{aligned}
T_{\mathcal{F}} &= \frac{1}{2}\rho_{\mathcal{F}} \int_{\mathcal{F}} \|\nabla\phi\|^2 \, \mathrm{d}V, \\
&= \frac{1}{2}\rho_{\mathcal{F}} \int_{\mathcal{F}} \nabla\phi \cdot \nabla\phi \, \mathrm{d}V.
\end{aligned} \tag{4.4}$$

By utilizing product rules for multiplication of vector field by scalar, the expression under integral can be expressed as

$$\nabla\phi \cdot \nabla\phi = \nabla \cdot (\phi\nabla\phi) - \phi\Delta\phi, \tag{4.5}$$

while Laplacian of ϕ is zero due to the assumed fluid incompressibility

$$\Delta\phi = 0, \tag{4.6}$$

leading to expression for fluid kinetic energy

$$T_{\mathcal{F}} = \frac{1}{2}\rho_{\mathcal{F}} \int_{\mathcal{F}} \nabla \cdot (\phi\nabla\phi) \, \mathrm{d}V. \tag{4.7}$$

Since the fluid is taken to be at rest in infinity - this is physically justified since any non-zero value of the fluid velocity at infinity leads to infinite values of kinetic energy - divergence theorem (also known as Gauss-Ostrogradsky theorem, or Green's theorem in two dimensions), a special case of more general Stokes formula [40], can be applied to transform the expression in (4.7) from volume integral over the fluid domain $\mathcal{F}$ to the

surface integral over boundary of the multibody system $\partial \mathcal{B} = \sum_{i=1}^{k} \partial \mathcal{B}_i$

$$T_{\mathcal{F}} = \frac{1}{2} \rho_{\mathcal{F}} \int_{\sum_{i=1}^{k} \partial \mathcal{B}_i} \phi \nabla \phi \cdot \boldsymbol{n_i} \, \mathrm{d}S, \tag{4.8}$$

where $\boldsymbol{n_i}$ represents the unit normal vector to $\partial \mathcal{B}_i$, pointing inward to the body, or outwards to the fluid domain $\mathcal{F}$.

Since velocity potential at any point depends only on the configurations and velocities pertinent to the multibody system [60], the potential can be formulated as

$$\phi = \sum_{i=1}^{k} \left(\boldsymbol{v_i} \cdot \boldsymbol{\theta_i} + \boldsymbol{\omega_i} \cdot \boldsymbol{\eta_i} \right), \tag{4.9}$$

where $\boldsymbol{\theta_i}$ represents the vector of translational velocity potentials related to ith body, $\boldsymbol{\eta_i}$ represents the vector of rotational velocity potentials related to ith body, while $\boldsymbol{v_i}$ and $\boldsymbol{\omega_i}$ represent respectively translational and rotational velocity of ith body in body-fixed reference frame.

Since body velocities do not depend on the positional coordinates, the directional derivative of the potential function along the unit normal of ith body is equal to

$$\nabla \phi \cdot \boldsymbol{n} \bigg|_{\partial \mathcal{B}_i} = \frac{\partial \phi}{\partial \boldsymbol{n}} \bigg|_{\partial \mathcal{B}_i} = \sum_{i=1}^{k} \left(\boldsymbol{v_i} \cdot \frac{\partial \boldsymbol{\theta_i}}{\partial \boldsymbol{n_i}} + \boldsymbol{\omega_i} \cdot \frac{\partial \boldsymbol{\eta_i}}{\partial \boldsymbol{n_i}} \right). \tag{4.10}$$

The expressions for calculating normal derivatives of the velocity potentials can be obtained by imposing the non-penetrability condition, constraining the fluid flow on the surface of the multibody system to tangential component only, requiring the components of fluid flow and body velocity in normal direction to be equal

$$\frac{\partial \phi}{\partial \boldsymbol{n}} \bigg|_{\partial \mathcal{B}_i} = v_{\text{point}} \cdot \boldsymbol{n_i} = \left(\boldsymbol{v_i} + \boldsymbol{\omega_i} \times \boldsymbol{r_i} \right) \cdot \boldsymbol{n_i}, \tag{4.11}$$

where v_{point} represents the velocity of the point on the ith body surface, $\boldsymbol{r_i}$ denotes position of the point and $\boldsymbol{n_i}$ represents unit normal, all expressed in $\mathcal{B}_i$-fixed reference frame.

Combining equations (4.10) and (4.11) leads to the expression

$$\sum_{i=1}^{k} \left(\boldsymbol{v_i} \cdot \frac{\partial \boldsymbol{\theta_i}}{\partial \boldsymbol{n_i}} + \boldsymbol{\omega_i} \cdot \frac{\partial \boldsymbol{\eta_i}}{\partial \boldsymbol{n_i}} \right) = \left(\boldsymbol{v_i} + \boldsymbol{\omega_i} \times \boldsymbol{r_i} \right) \cdot \boldsymbol{n_i}, \tag{4.12}$$

which has to be satisfied for any possible combination of velocities $\boldsymbol{v_i}$ and $\boldsymbol{\omega_i}$, therefore

requiring that

$$
\begin{aligned}
\boldsymbol{v}_i \cdot \frac{\partial \boldsymbol{\theta}_i}{\partial \boldsymbol{n}_i} &= \boldsymbol{v}_i \cdot \boldsymbol{n}_i \\
\boldsymbol{\omega}_i \cdot \frac{\partial \boldsymbol{\eta}_i}{\partial \boldsymbol{n}_i} &= (\boldsymbol{\omega}_i \times \boldsymbol{r}_i) \cdot \boldsymbol{n}_i
\end{aligned}
\tag{4.13}
$$

The expression $(\boldsymbol{\omega}_i \times \boldsymbol{r}_i) \cdot \boldsymbol{n}_i$ can be rewritten as

$$
\begin{aligned}
(\boldsymbol{\omega}_i \times \boldsymbol{r}_i) \cdot \boldsymbol{n}_i &= (\tilde{\boldsymbol{\omega}}_i \boldsymbol{r}_i)^{\mathrm{T}} \boldsymbol{n}_i = -(\tilde{\boldsymbol{r}}_i \boldsymbol{\omega}_i)^{\mathrm{T}} \boldsymbol{n}_i = -\boldsymbol{\omega}_i^{\mathrm{T}} \tilde{\boldsymbol{r}}_i^{\mathrm{T}} \boldsymbol{n}_i = \boldsymbol{\omega}_i^{\mathrm{T}} \tilde{\boldsymbol{r}}_i \boldsymbol{n}_i \\
&= \boldsymbol{\omega}_i \cdot (\boldsymbol{r}_i \times \boldsymbol{n}_i),
\end{aligned}
\tag{4.14}
$$

where $\tilde{\cdot}$ operator represents a skew symmetric matrix with properties

$$
\tilde{\boldsymbol{a}} \boldsymbol{b} = \boldsymbol{a} \times \boldsymbol{b}, \ \tilde{\boldsymbol{a}}^{\mathrm{T}} = -\tilde{\boldsymbol{a}} \qquad \forall \, \boldsymbol{a}, \boldsymbol{b} \in \mathbb{R}^3.
\tag{4.15}
$$

Expressions (4.13) and (4.14) can be combined to obtain values for the normal derivatives of velocity potentials on $\partial \mathcal{B}_j$ as

$$
\begin{aligned}
\frac{\partial \boldsymbol{\theta}_i}{\partial \boldsymbol{n}_j} &= \begin{cases} \boldsymbol{n}_i & i = j, \\ \boldsymbol{0} & i \neq j, \end{cases} \\
\frac{\partial \boldsymbol{\eta}_i}{\partial \boldsymbol{n}_j} &= \begin{cases} \boldsymbol{r}_i \times \boldsymbol{n}_i & i = j, \\ \boldsymbol{0} & i \neq j. \end{cases}
\end{aligned}
\tag{4.16}
$$

The expression for fluid kinetic energy (4.8) can now be rewritten, by using (4.9), (4.10) and (4.16), as

$$
\begin{aligned}
T_{\mathcal{F}} &= \frac{1}{2} \rho_{\mathcal{F}} \int_{\sum_{j=1}^{k} \partial \mathcal{B}_j} \sum_{i=1}^{k} (\boldsymbol{v}_i \cdot \boldsymbol{\theta}_i + \boldsymbol{\omega}_i \cdot \boldsymbol{\eta}_i) \left(\frac{\partial \boldsymbol{\theta}_j}{\partial \boldsymbol{n}_j} \cdot v_j + \frac{\partial \boldsymbol{\eta}_j}{\partial \boldsymbol{n}_j} \cdot \omega_j \right) \mathrm{d}S, \\
&= \frac{1}{2} \rho_{\mathcal{F}} \sum_{i=1}^{k} \sum_{j=1}^{k} \int_{\partial \mathcal{B}_j} \left(\boldsymbol{v}_i^{\mathrm{T}} \boldsymbol{\theta}_i \frac{\partial \boldsymbol{\theta}_j}{\partial \boldsymbol{n}_j}^{\mathrm{T}} v_j + \boldsymbol{v}_i^{\mathrm{T}} \boldsymbol{\theta}_i \frac{\partial \boldsymbol{\eta}_j}{\partial \boldsymbol{n}_j}^{\mathrm{T}} \omega_j \right. \\
&\qquad\qquad\qquad \left. + \boldsymbol{\omega}_i^{\mathrm{T}} \boldsymbol{\eta}_i \frac{\partial \boldsymbol{\theta}_j}{\partial \boldsymbol{n}_j}^{\mathrm{T}} v_j + \boldsymbol{\omega}_i^{\mathrm{T}} \boldsymbol{\eta}_i \frac{\partial \boldsymbol{\eta}_j}{\partial \boldsymbol{n}_j}^{\mathrm{T}} \omega_j \right) \mathrm{d}S.
\end{aligned}
\tag{4.17}
$$

If $\boldsymbol{V}_i = \begin{pmatrix} \boldsymbol{v}_i^{\mathrm{T}} & \boldsymbol{\omega}_i^{\mathrm{T}} \end{pmatrix}^{\mathrm{T}}$ is introduced to represent translational and rotational velocity of ith body, and matrix defining added inertia contribution of the body i on the body j is

introduced in block matrix form as

$$
\boldsymbol{M}_{ij}^f =
\begin{pmatrix}
\boldsymbol{m}_{ij}^{f,vv} & \boldsymbol{m}_{ij}^{f,v\omega} \\
\\
\boldsymbol{m}_{ij}^{f,\omega v} & \boldsymbol{m}_{ij}^{f,\omega\omega}
\end{pmatrix},
\tag{4.18}
$$

where elements are equal to

$$
\begin{aligned}
\boldsymbol{m}_{ij}^{f,vv} &= \int_{\partial\mathcal{B}_j} \boldsymbol{\theta}_i \frac{\partial\boldsymbol{\theta}_j}{\partial\boldsymbol{n}_j}^{\mathrm{T}} \,\mathrm{d}S, &
\boldsymbol{m}_{ij}^{f,v\omega} &= \int_{\partial\mathcal{B}_j} \boldsymbol{\theta}_i \frac{\partial\boldsymbol{\eta}_j}{\partial\boldsymbol{n}_j}^{\mathrm{T}} \,\mathrm{d}S, \\
\boldsymbol{m}_{ij}^{f,\omega v} &= \int_{\partial\mathcal{B}_j} \boldsymbol{\eta}_i \frac{\partial\boldsymbol{\theta}_j}{\partial\boldsymbol{n}_j}^{\mathrm{T}} \,\mathrm{d}S, &
\boldsymbol{m}_{ij}^{f,\omega\omega} &= \int_{\partial\mathcal{B}_j} \boldsymbol{\eta}_i \frac{\partial\boldsymbol{\eta}_j}{\partial\boldsymbol{n}_j}^{\mathrm{T}} \,\mathrm{d}S,
\end{aligned}
\tag{4.19}
$$

the expression (4.17) can be reformulated as

$$
\begin{aligned}
T_{\mathcal{F}} &= \frac{1}{2}\rho_{\mathcal{F}} \sum_{i=1}^{k}\sum_{j=1}^{k} \left(\boldsymbol{v}_i^{\mathrm{T}} \boldsymbol{m}_{ij}^{f,vv} \boldsymbol{v}_i + \boldsymbol{v}_i^{\mathrm{T}} \boldsymbol{m}_{ij}^{f,v\omega} \boldsymbol{\omega}_i + \boldsymbol{\omega}_i^{\mathrm{T}} \boldsymbol{m}_{ij}^{f,\omega v} \boldsymbol{v}_i + \boldsymbol{\omega}_i^{\mathrm{T}} \boldsymbol{m}_{ij}^{f,\omega\omega} \boldsymbol{\omega}_i \right), \\
&= \frac{1}{2}\rho_{\mathcal{F}} \sum_{i=1}^{k}\sum_{j=1}^{k} \boldsymbol{V}_i^{\mathrm{T}} \boldsymbol{M}_{ij}^f \boldsymbol{V}_j.
\end{aligned}
\tag{4.20}
$$

The matrix M_{ij}^f represents the added inertia that body j experiences due to the influence from body i.

4.3 Boundary value problem

Derivatives of translational and rotational parts of fluid velocity potential in (4.19) are known from non-penetrability boundary conditions (4.16). However, values of the potentials along the surface of the multibody system have to be calculated. It is important to note that each of the potentials also has to satisfy divergence-free assumption (4.6), in order for the formulation (4.9) to be valid for any combination of body velocities. This leads to $6k$ exterior Laplace problems with boundary constraints (4.16).

Following the approach in [61], since $\Delta\theta_1 = 0$, the expression

$$
\int_{\mathcal{F}} f\Delta\theta_1 \,\mathrm{d}V = 0
\tag{4.21}
$$

holds for any sufficiently well behaved function f, with position as only variable.

It is now useful to mention Green's second identity, which can be expressed as [62]

$$\int_{\mathcal{F}} (f\Delta\theta_1 - \theta_1\Delta f)\,\mathrm{d}V = \int_{\partial\mathcal{B}} \left(f\frac{\partial\theta_1}{\partial\boldsymbol{n}} - \theta_1\frac{\partial f}{\partial\boldsymbol{n}}\right)\mathrm{d}S, \tag{4.22}$$

which can be applied to expression (4.21), resulting in

$$\int_{\partial\mathcal{B}} \left(f\frac{\partial\theta_1}{\partial\boldsymbol{n}} - \theta_1\frac{\partial f}{\partial\boldsymbol{n}}\right)\mathrm{d}S + \int_{\mathcal{F}} \theta_1\Delta f\,\mathrm{d}V = 0. \tag{4.23}$$

If function f is taken to be fundamental solution, satisfying Laplace solution $\Delta f = 0$, expression (4.23) is defined by using boundary domain only, as

$$\int_{\partial\mathcal{B}} \left(f\frac{\partial\theta_1}{\partial\boldsymbol{n}} - \theta_1\frac{\partial f}{\partial\boldsymbol{n}}\right)\mathrm{d}S = 0. \tag{4.24}$$

Fundamental solution, usually named Green's function G_L, for the Laplace equation in three dimensions can be taken as [61]

$$G_L(P,T) = \frac{1}{4\pi r}, \tag{4.25}$$

where $P, T \in \partial(B)$ represent points on the boundary of the multibody system, while $r = \|\boldsymbol{r}\| = \|T - P\|$ represents distance between points P and T.

The boundary value problem can now be defined for any point on the multibody system boundary point P, as

$$\mathcal{P}(P) = \lim_{P_E \to P} \int_{\partial\mathcal{B}} \left(G_L(P_E,T)\frac{\partial\theta_1}{\partial\boldsymbol{n}}(T) - \theta_1(T)\frac{\partial G_L}{\partial\boldsymbol{n}}(P_E,T)\right)\mathrm{d}T = 0, \tag{4.26}$$

where limit is necessary, because of the singularity in Green's function, and its derivative, for $P = T$. However, the integral itself is not singular, as shown for the chosen discretization in the following sections.

4.4 Boundary element method

In order to solve (4.26) for value of potential θ_1 over the multibody system boundary, the surface is discretized by boundary elements. The following discussion and derivation is presented for the case of two dimensions, for the sake of clarity and brevity. However, algorithm for analysis in three dimensions is derived equivalently.

If the boundary of the two dimensional geometry is discretized by N boundary elements (and nodes), as illustrated in Fig. 4.1, there are multiple approaches that can be taken in order to solve for the boundary value problem (4.26). Probably the most intuitive approach is to enforce (4.26) in each of the discretization nodes P_i

$$
\begin{pmatrix}
\mathcal{P}(P_1) \\
\mathcal{P}(P_2) \\
\vdots \\
\mathcal{P}(P_N)
\end{pmatrix} = \mathbf{0}, \tag{4.27}
$$

leading to what is usually called collocation boundary element method.
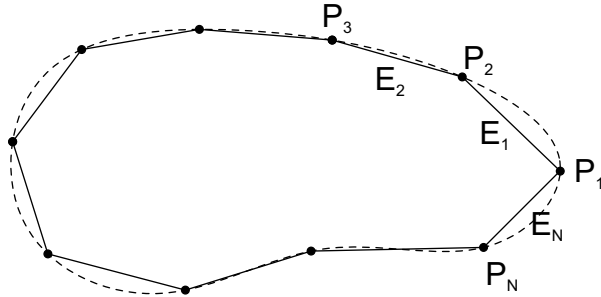
Figure 4.1: Illustration of two dimensional shape discretization with N boundary elements E, and associated N discretization nodes P.

In order to solve the boundary value problem (4.26), two integrals need to be discretized, namely

$$
\begin{aligned}
\mathcal{I}_i^1 &= \lim_{P_E \to P_i} \int_{\partial \mathcal{B}} G_L\left(P_E, T\right) \frac{\partial \theta_1}{\partial \boldsymbol{n}}(T)\, \mathrm{d}T, \\
\mathcal{I}_i^2 &= \lim_{P_E \to P_i} \int_{\partial \mathcal{B}} \theta_1(T) \frac{\partial G_L}{\partial \boldsymbol{n}}\left(P_E, T\right) \mathrm{d}T.
\end{aligned} \tag{4.28}
$$

If two dimensional shape is discretized by boundary elements, the integrals can be approximated as

$$
\begin{aligned}
\mathcal{I}_i^1 &\approx \sum_{j=1}^{N} \int_{E_j} G_L\left(P_i, T\right) \frac{\partial \theta_1}{\partial \boldsymbol{n}}(T)\, \mathrm{d}T, \\
\mathcal{I}_i^2 &\approx \sum_{j=1}^{N} \int_{E_j} \theta_1(T) \frac{\partial G_L}{\partial \boldsymbol{n}}\left(P_i, T\right) \mathrm{d}T,
\end{aligned} \tag{4.29}
$$

while equality sign $=$ will be used instead of approximation sign $\approx$ in further discussion, to simplify reading.

The boundary elements are taken to be linear, but it is important to note that higher order approximations can easily be implemented by changing shape functions and adding nodes as necessary, while the rest of the method remains unchanged.

The boundary element numbering is set to increase in the anticlockwise direction, as shown in Fig. 4.1, while the normal to the elements points inward to the shape, in order to be equivalent to (4.8). This means that if the boundary element is traversed from its lower numbered node to higher numbered node (except for the last element), normal points to the left. The linear 2D boundary element is illustrated in Fig. 4.2. Parametric variable s is defined as $0 \leq s \leq 1$, for each element.
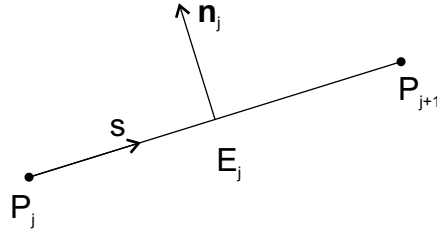
Figure 4.2: Illustration of ith linear 2D boundary element, with its associated unit normal.

The approximation of values for the potential and its derivative over the element can now be defined as

$$
\begin{aligned}
\theta_1(s) &= \psi_1(s)\theta_1(P_i) + \psi_2(s)\theta_1(P_{i+1}), \\
\frac{\partial \theta_1}{\partial \boldsymbol{n}}(s) &= \psi_1(s)\frac{\partial \theta_1}{\partial \boldsymbol{n}}(P_i) + \psi_2(s)\frac{\partial \theta_1}{\partial \boldsymbol{n}}(P_{i+1}),
\end{aligned}
\tag{4.30}
$$

where $\psi_1(s)$ and $\psi_2(s)$ represent linear shape functions, defined as

$$
\begin{aligned}
\psi_1(s) &= 1 - s, \\
\psi_2(s) &= s.
\end{aligned}
\tag{4.31}
$$

If the linear approximations of potential and its derivative (4.30) are used and integration variable changed to parametric variable s, the integrals (4.29) can be formulated as

$$
\begin{aligned}
\mathcal{I}_i^1 &= \sum_{j=1}^{N} \int_0^1 G_L\left(P_i, T(s)\right) \left(\psi_1(s)\frac{\partial \theta_1}{\partial \boldsymbol{n}}(P_j) + \psi_2(s)\frac{\partial \theta_1}{\partial \boldsymbol{n}}(P_{j+1})\right) J(s)\,\mathrm{d}s, \\
&= \sum_{j=1}^{N} \int_0^1 G_L\left(P_i, T(s)\right) \sum_{k=1}^{2}\left(\psi_k(s)\frac{\partial \theta_1}{\partial \boldsymbol{n}}(P_{j+k-1})\right) J(s)\,\mathrm{d}s,
\end{aligned}
$$

$$
\begin{aligned}
&= \sum_{k=1}^{2} \sum_{j=1}^{N} \frac{\partial \theta_1}{\partial \boldsymbol{n}}(P_{j+k-1}) \int_0^1 \psi_k(s) G_L\left(P_i, T(s)\right) J(s)\, \mathrm{d}s, \\
&= \sum_{j=1}^{N} \sum_{k=1}^{2} \frac{\partial \theta_1}{\partial \boldsymbol{n}}(P_{j+k-1}) \mathcal{I}_{ik}^{1,j}, \tag{4.32} \\
\mathcal{I}_i^2 &= \sum_{j=1}^{N} \int_0^1 \Big(\psi_1(s)\theta_1(P_j) + \psi_2(s)\theta_1(P_{j+1})\Big) \frac{\partial G_L}{\partial \boldsymbol{n}}\left(P_i, T(s)\right) J(s)\, \mathrm{d}s, \\
&= \sum_{j=1}^{N} \int_0^1 \frac{\partial G_L}{\partial \boldsymbol{n}}\left(P_i, T(s)\right) \sum_{k=1}^{2} \Big(\psi_k(s)\theta_1(P_{j+k-1})\Big) J(s)\, \mathrm{d}s, \\
&= \sum_{k=1}^{2} \sum_{j=1}^{N} \theta_1(P_{j+k-1}) \int_0^1 \psi_k(s)\frac{\partial G_L}{\partial \boldsymbol{n}}\left(P_i, T(s)\right) J(s)\, \mathrm{d}s, \\
&= \sum_{j=1}^{N} \sum_{k=1}^{2} \theta_1(P_{j+k-1}) \mathcal{I}_{ik}^{2,j}, \tag{4.33}
\end{aligned}
$$

while $J = \|\frac{\mathrm{d}T}{\mathrm{d}s}\|$ represents Jacobian, which is constant for a linear element, being equal to element's length. It is also important to take into account when implementing algorithm that P_{N+1} occurs in the above expressions, and should be set to P_1, because of the closed chain of boundary elements - this has been omitted from the presented formal expressions to avoid introducing unnecessary confusion.

The collocation equations (4.27) can now be formulated as

$$
\begin{pmatrix} \mathcal{I}_1^2 \\ \mathcal{I}_2^2 \\ \vdots \\ \mathcal{I}_N^2 \end{pmatrix} = \begin{pmatrix} \mathcal{I}_1^1 \\ \mathcal{I}_2^1 \\ \vdots \\ \mathcal{I}_N^1 \end{pmatrix}, \tag{4.34}
$$

resulting in the linear system of N equations with N unknowns. The problem of formulating the final system of linear equations can now be approached as

$$
\boldsymbol{A} \begin{pmatrix} \theta_1(P_1) \\ \theta_1(P_2) \\ \vdots \\ \theta_1(P_N) \end{pmatrix} = \boldsymbol{B} \begin{pmatrix} \frac{\partial \theta_1}{\partial \boldsymbol{n}}(P_1) \\ \frac{\partial \theta_1}{\partial \boldsymbol{n}}(P_2) \\ \vdots \\ \frac{\partial \theta_1}{\partial \boldsymbol{n}}(P_N) \end{pmatrix}, \tag{4.35}
$$

where matrices $\boldsymbol{A}$ and $\boldsymbol{B}$ are equal to

$$\boldsymbol{A} = \begin{pmatrix} \mathcal{I}_{12}^{2,N} + \mathcal{I}_{11}^{2,1} & \mathcal{I}_{12}^{2,1} + \mathcal{I}_{11}^{2,2} & \cdots & \mathcal{I}_{12}^{2,N-1} + \mathcal{I}_{11}^{2,N} \\ \mathcal{I}_{22}^{2,N} + \mathcal{I}_{21}^{2,1} & \mathcal{I}_{22}^{2,1} + \mathcal{I}_{21}^{2,2} & \cdots & \mathcal{I}_{22}^{2,N-1} + \mathcal{I}_{21}^{2,N} \\ \vdots & & \ddots & \vdots \\ \mathcal{I}_{N2}^{2,N} + \mathcal{I}_{N1}^{2,1} & \mathcal{I}_{N2}^{2,1} + \mathcal{I}_{N1}^{2,2} & \cdots & \mathcal{I}_{N2}^{2,N-1} + \mathcal{I}_{N1}^{2,N} \end{pmatrix}, \tag{4.36}$$

$$\boldsymbol{B} = \begin{pmatrix} \mathcal{I}_{12}^{1,N} + \mathcal{I}_{11}^{1,1} & \mathcal{I}_{12}^{1,1} + \mathcal{I}_{11}^{1,2} & \cdots & \mathcal{I}_{12}^{1,N-1} + \mathcal{I}_{11}^{1,N} \\ \mathcal{I}_{22}^{1,N} + \mathcal{I}_{21}^{1,1} & \mathcal{I}_{22}^{1,1} + \mathcal{I}_{21}^{1,2} & \cdots & \mathcal{I}_{22}^{1,N-1} + \mathcal{I}_{21}^{1,N} \\ \vdots & & \ddots & \vdots \\ \mathcal{I}_{N2}^{1,N} + \mathcal{I}_{N1}^{1,1} & \mathcal{I}_{N2}^{1,1} + \mathcal{I}_{N1}^{1,2} & \cdots & \mathcal{I}_{N2}^{1,N-1} + \mathcal{I}_{N1}^{1,N} \end{pmatrix}. \tag{4.37}$$

The Green function, involved in calculation of integral $\mathcal{I}_{ik}^{1,j}$ for two dimensional Laplace problem can be defined as

$$G_L(P, T) = -\frac{\ln(r)}{2\pi}, \tag{4.38}$$

where $r = \|\boldsymbol{r}\| = \|T - P\|$.

In order to determine directional derivative required for computing integral $\mathcal{I}_{ik}^{2,j}$, the gradient of the Green function is calculated as

$$\begin{aligned} \nabla G_L = -\frac{1}{2\pi} \begin{pmatrix} \frac{1}{r} \frac{\partial}{\partial x_T} \left(\sqrt{(x_T - x_P)^2 + (y_T - y_P)^2} \right) \\ \frac{1}{r} \frac{\partial}{\partial y_T} \left(\sqrt{(x_T - x_P)^2 + (y_T - y_P)^2} \right) \end{pmatrix} = \\ = -\frac{1}{2\pi r^2} \begin{pmatrix} x_T - x_P \\ y_T - y_P \end{pmatrix} = -\frac{\boldsymbol{r}}{2\pi r^2}. \end{aligned} \tag{4.39}$$

Directional derivative of the Green function with respect to unit normal can now be formulated as

$$\frac{\partial G_L}{\partial \boldsymbol{n}} = \nabla G_L \cdot \boldsymbol{n} = -\frac{\boldsymbol{r} \cdot \boldsymbol{n}}{2\pi r^2}. \tag{4.40}$$

It is now important to note that both Green's function $G_L(P, T)$ (and consequently integral $\mathcal{I}_{ik}^{1,j}$) together with its directional derivative with respect to unit normal $\frac{\partial G_L}{\partial \boldsymbol{n}}$ (and

consequently integral $\mathcal{I}_{ik}^{2,j}$) depend only on the shape of bodies and the configuration of the multibody system. Because of this, matrices $\boldsymbol{A}$ and $\boldsymbol{B}$ do not depend on the velocity potential considered in analysis and same matrices can be used for all velocity potential components, as long as the shape or multibody system configuration (most often caused by relative rotation between bodies) is not changed. Therefore, in each time step matrices $\boldsymbol{A}$ and $\boldsymbol{B}$ are formulated only once and then used to solve for three velocity components

$$
\boldsymbol{A} \begin{pmatrix} \theta_1(P_1) \\ \vdots \\ \theta_1(P_N) \end{pmatrix} = \boldsymbol{B} \begin{pmatrix} \frac{\partial \theta_1}{\partial \boldsymbol{n}}(P_1) \\ \vdots \\ \frac{\partial \theta_1}{\partial \boldsymbol{n}}(P_N) \end{pmatrix}, \boldsymbol{A} \begin{pmatrix} \theta_2(P_1) \\ \vdots \\ \theta_2(P_N) \end{pmatrix} = \boldsymbol{B} \begin{pmatrix} \frac{\partial \theta_2}{\partial \boldsymbol{n}}(P_1) \\ \vdots \\ \frac{\partial \theta_2}{\partial \boldsymbol{n}}(P_N) \end{pmatrix},
$$
$$
\boldsymbol{A} \begin{pmatrix} \eta(P_1) \\ \vdots \\ \eta(P_N) \end{pmatrix} = \boldsymbol{B} \begin{pmatrix} \frac{\partial \eta}{\partial \boldsymbol{n}}(P_1) \\ \vdots \\ \frac{\partial \eta}{\partial \boldsymbol{n}}(P_N) \end{pmatrix}.
$$

(4.41)

This is important since formulating matrices $\boldsymbol{A}$ and $\boldsymbol{B}$ consumes the most of the computational time required to run the algorithm, due to computation of $2N$ integrals for each matrix.

However, some of the integrals involved in populating matrices $\boldsymbol{A}$ and $\boldsymbol{B}$ are not as trivial as it may seem at a first glance. If the collocation point P_i also belongs to the element E_j over which integrations in $\mathcal{I}_{ik}^{1,j}$ and $\mathcal{I}_{ik}^{2,j}$ are performed the underlying functions (Green's function and its directional derivative with respect to unit normal) become singular, because at some point $r \to 0$, causing $G_L(P,T) \to \infty$ and $\partial G_L / \partial \boldsymbol{n} \to -\infty$. In total, there are four singular integrals for each collocation point (each row of matrix $\boldsymbol{A}$ or $\boldsymbol{B}$), two occurring on the main diagonal, and two on the neighboring matrix elements, as illustrated on the Fig. 4.3 for one body. For the case of multibody chain, matrices like one illustrated in Fig. 4.3 are supplemented with nonsingular block matrices, since no singular integral occurs for the combination of collocation point P_i on one body and element E_j on another.

Although the functions under integral diverge, the integrals themselves are convergent
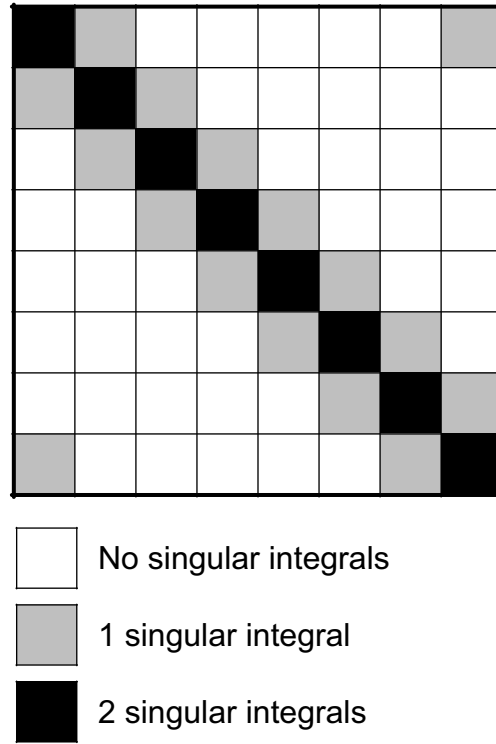
No singular integrals

1 singular integral

2 singular integrals

Figure 4.3: Illustration of singular integral positions in matrices $\boldsymbol{A}$ and $\boldsymbol{B}$ for one body.

and analytic solutions can be found. Singular integrals occur under two circumstances, when collocation point P_i is at the lower numbered node of element E_j (Fig. 4.4a), or when the point P_i is at the higher numbered node of element E_j (Fig. 4.4b). The problem of singular integrals is approached by replacing collocation point P by

$$P_{\varepsilon,i} = P + \varepsilon \boldsymbol{n_j}, \tag{4.42}$$

as illustrated in Fig. 4.5, and taking the limit of the integral as $\varepsilon \to 0$. Analytic integration of eight singular integrals (four for each matrix $\boldsymbol{A}$ or $\boldsymbol{B}$) is presented in next subsections, followed by subsection on regular integral calculation.
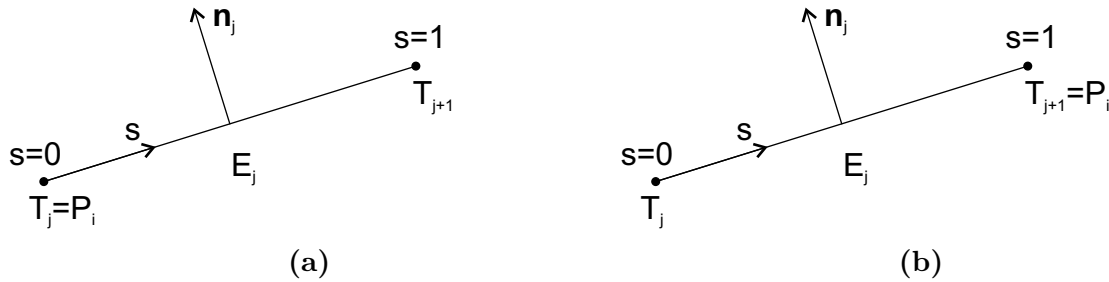

(a)

(b)

Figure 4.4: Two circumstances under which singular integration occurs: (a) when collocation point is at the begining of element ($s = 0$) or (b) when collocation point is at the end of element $s = 1$.
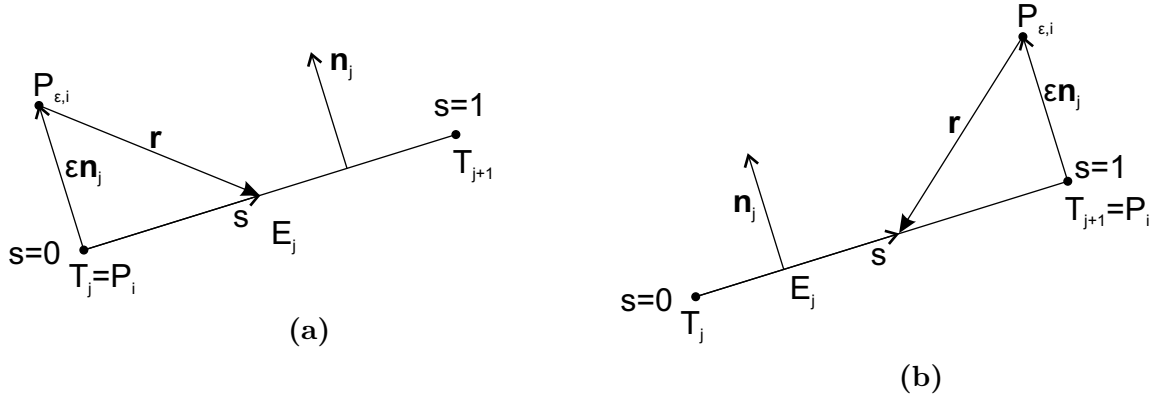
Figure 4.5: Illustration of replacing collocation point P_i with $P_{\varepsilon,i}$ and resulting distance vector $\boldsymbol{r}$.

4.4.1 Singular integral with collocation point at the beginning of element

The first case considered is the collocation point P_i at the beginning of element E_j over which the integration occurs (Fig. 4.4a).

Singular integral of G_L with shape function ψ_1

The first sigular integral considered is

$$
\begin{aligned}
\mathcal{I}_{i1}^{1,i} &= \int_0^1 \psi_1(s) G_L\left(P_{\varepsilon,i}, T(s)\right) J \,\mathrm{d}s \\
&= J \int_0^1 (1-s) \frac{-\ln(r)}{2\pi} \,\mathrm{d}s \\
&= -\frac{J}{4\pi} \int_0^1 (1-s) \ln(r^2) \,\mathrm{d}s,
\end{aligned}
\tag{4.43}
$$

where r^2 can be expressed as (see Fig. 4.5a)

$$
r^2 = J^2 s^2 + \varepsilon^2.
\tag{4.44}
$$

The integral can now be formulated as

$$
\mathcal{I}_{i1}^{1,i} = -\frac{J}{4\pi} \lim_{\varepsilon \to 0} \int_0^1 (1-s) \ln(J^2 s^2 + \varepsilon^2) \,\mathrm{d}s
\tag{4.45}
$$

and now utilization of symbolic integration results with

$$\mathcal{I}_{i1}^{1,i} = \frac{1}{8J\pi} \lim_{\varepsilon \to 0} \left(\left(J^2 s^2 - 2J^2 s + \varepsilon^2\right) \ln\left(J^2 s^2 + \varepsilon^2\right) \right.$$
$$\left. \left. -4J\varepsilon \arctan\left(\frac{Js}{\varepsilon}\right) - J^2 s^2 + 4J^2 s\right) \right|_{s=0}^{s=1}.$$
(4.46)

There are two terms involving ε variable and the limits are equal to

$$\lim_{\varepsilon \to 0} \left(\left(J^2 s^2 - 2J^2 s + \varepsilon^2\right) \ln\left(J^2 s^2 + \varepsilon^2\right) \right) = 2(J^2 s^2 - 2J^2 s) \ln\left(Js\right), \quad (4.47)$$

$$\lim_{\varepsilon \to 0} \left(4J\varepsilon \arctan\left(\frac{Js}{\varepsilon}\right) \right) = 4J \cdot 0 \cdot \frac{\pi}{2} = 0. \quad (4.48)$$

The integral can now finally be evaluated as

$$\mathcal{I}_{i1}^{1,i} = \frac{1}{8J\pi} \left(2(J^2 s^2 - 2J^2 s) \ln\left(Js\right) - J^2 s^2 + 4J^2 s \right) \Big|_{s=0}^{s=1},$$
$$= \frac{J}{8\pi} \left(3 - 2\ln(J) \right).$$

(4.49)

It may be useful to note that final calculation also involved term

$$\lim_{s \to 0}(s \ln(Js)) = \lim_{s \to 0} \frac{\ln(Js)}{\frac{1}{s}} = \lim_{s \to 0} \frac{\frac{1}{s}}{\frac{-1}{s^2}} = \lim_{s \to 0}(-s) = 0. \quad (4.50)$$

Singular integral of G_L with shape function ψ_2

Similar approach is used to derive analytic solution to integral

$$\mathcal{I}_{i2}^{1,i} = \int_0^1 \psi_2(s) G_L\left(P_{\varepsilon,i}, T(s)\right) J \, \mathrm{d}s$$
$$= -\frac{J}{4\pi} \int_0^1 s \ln(r^2) \, \mathrm{d}s$$
$$= -\frac{J}{4\pi} \lim_{\varepsilon \to 0} \int_0^1 s \ln(J^2 s^2 + \varepsilon^2) \, \mathrm{d}s, \quad (4.51)$$

and symbolic integration then results with

$$\mathcal{I}_{i2}^{1,i} = -\frac{1}{8J\pi} \lim_{\varepsilon \to 0} \left(\left(J^2 s^2 + \varepsilon^2 \right) \ln \left(J^2 s^2 + \varepsilon^2 \right) - J^2 s^2 \right) \Bigg|_{s=0}^{s=1}. \tag{4.52}$$

There is only one term consisting of ε and the limit is equal to

$$\lim_{\varepsilon \to 0} \left(\left(J^2 s^2 + \varepsilon^2 \right) \ln \left(J^2 s^2 + \varepsilon^2 \right) \right) = 2J^2 s^2 \ln(Js). \tag{4.53}$$

If the similar rule as (4.50) is applied, the integral is evaluated as

$$\mathcal{I}_{i2}^{1,i} = -\frac{1}{8J\pi} \left(2J^2 s^2 \ln(Js) - J^2 s^2 \right) \Bigg|_{s=0}^{s=1} \tag{4.54}$$

$$= \frac{J}{8\pi} \left(1 - 2\ln(J) \right). \tag{4.55}$$

Singular integral of $\partial G_L / \partial \boldsymbol{n}$ with shape function ψ_1

Singular integral of $\partial G_L / \partial \boldsymbol{n}$ with first shape function is formulated as

$$\mathcal{I}_{i1}^{2,i} = \int_0^1 \psi_1(s) \frac{\partial G_L}{\partial \boldsymbol{n}} \left(P_{\varepsilon,i}, T(s) \right) J \, \mathrm{d}s$$

$$= J \int_0^1 (1 - s) \frac{-\boldsymbol{r} \cdot \boldsymbol{n}}{2\pi r^2} \, \mathrm{d}s$$

$$= -\frac{J}{2\pi} \int_0^1 (1 - s) \frac{\boldsymbol{r} \cdot \boldsymbol{n}}{r^2} \, \mathrm{d}s. \tag{4.56}$$

It can be concluded from Fig. 4.5a that distance vector can be formulated as $\boldsymbol{r} = -\varepsilon \boldsymbol{n} + Js\boldsymbol{n}_\perp$, where $\boldsymbol{n}_\perp$ represents unit vector in direction of variable s growth (perpendicular to $\boldsymbol{n}$), and therefore the expression $\boldsymbol{r} \cdot \boldsymbol{n}$ is equal to

$$\boldsymbol{r} \cdot \boldsymbol{n} = (-\varepsilon \boldsymbol{n} + Js\boldsymbol{n}_\perp) \cdot \boldsymbol{n} = -\varepsilon, \tag{4.57}$$

since $\boldsymbol{n}$ represent unit vector. With this expression derived and r^2 expression from (4.44), integral can be formulated as

$$\mathcal{I}_{i1}^{2,i} = \frac{J}{2\pi} \lim_{\varepsilon \to 0} \int_0^1 (1 - s) \frac{\varepsilon}{J^2 s^2 + \varepsilon^2} \, \mathrm{d}s. \tag{4.58}$$

Symbolic integration of this expression results with

$$\mathcal{I}_{i1}^{2,i} = \frac{1}{2\pi} \lim_{\varepsilon \to 0} \left(\arctan\left(\frac{Js}{\varepsilon}\right) - \frac{\varepsilon \ln\left(J^2 s^2 + \varepsilon^2\right)}{2J} \right) \Bigg|_{s=0}^{s=1}, \tag{4.59}$$

with terms in limit equaling to

$$\lim_{\varepsilon \to 0} \arctan\left(\frac{Js}{\varepsilon}\right) = \frac{\pi}{2}, \tag{4.60}$$

$$\lim_{\varepsilon \to 0} \frac{\varepsilon \ln\left(J^2 s^2 + \varepsilon^2\right)}{2J^2} = 0. \tag{4.61}$$

Finally, the integral is equal to

$$\mathcal{I}_{i1}^{2,i} = \frac{1}{2\pi} \cdot \frac{\pi}{2} = \frac{1}{4}. \tag{4.62}$$

Singular integral of $\partial G_L / \partial \boldsymbol{n}$ with shape function ψ_2

Similar approach is again used to derive analytic solution to integral with shape function ψ_2

$$\begin{aligned}
\mathcal{I}_{i2}^{2,i} &= \int_0^1 \psi_2(s) \frac{\partial G_L}{\partial \boldsymbol{n}} \left(P_{\varepsilon,i}, T(s) \right) J \, \mathrm{d}s \\
&= -\frac{J}{2\pi} \int_0^1 s \frac{\boldsymbol{r} \cdot \boldsymbol{n}}{r^2} \, \mathrm{d}s \\
&= \frac{J}{2\pi} \lim_{\varepsilon \to 0} \int_0^1 s \frac{\varepsilon}{J^2 s^2 + \varepsilon^2} \, \mathrm{d}s.
\end{aligned} \tag{4.63}$$

Symbolic integration now results with

$$\lim_{\varepsilon \to 0} \left(\frac{\varepsilon}{2J^2} \left(\ln\left(\varepsilon^2 + J^2\right) - 2\ln\left(\varepsilon\right) \right) \right) \Bigg|_{s=0}^{s=1}, \tag{4.64}$$

which results in limit with

$$\mathcal{I}_{i2}^{2,i} = 0. \tag{4.65}$$

4.4.2 Singular integral with collocation point at the end of element

This sections focuses on singular integrals occurring when the collocation point P_i is at the end of element E_j over which the integration is performed (Fig. 4.5b). Since the procedure is similar to the one presented in Sect. 4.4.1 for collocation point at the beginning of element, main differences will be discussed here and then the solutions for singular integrals will be presented with minimal discussion.

The difference occurs in calculation of distance vector, which can be expressed as (see Fig. 4.5b)

$$\boldsymbol{r} = -\varepsilon\boldsymbol{n} - J(1-s)\boldsymbol{n}_\perp. \tag{4.66}$$

Terms r^2 and $\boldsymbol{n} \cdot r$, required for calculating singular integrals can now be expressed as

$$r^2 = J^2(1-s)^2 + \varepsilon^2, \tag{4.67}$$

$$\boldsymbol{n} \cdot r = -\varepsilon. \tag{4.68}$$

Integrals can now be calculated as follows.

Singular integral of G_L with shape function ψ_1

$$
\begin{aligned}
\mathcal{I}_{i1}^{1,i-1} &= \int_0^1 \psi_1(s)G_L\left(P_{\varepsilon,i}, T(s)\right) J \, \mathrm{d}s \\
&= -\frac{J}{4\pi} \int_0^1 (1-s)\ln(r^2) \, \mathrm{d}s \\
&= -\frac{J}{4\pi} \lim_{\varepsilon\to 0} \int_0^1 (1-s)\ln(J^2(1-s)^2 + \varepsilon^2) \, \mathrm{d}s.
\end{aligned}
\tag{4.69}
$$

Symbolic integration results with

$$
\mathcal{I}_{i1}^{1,i-1} = \frac{1}{8J\pi} \lim_{\varepsilon\to 0} \left(\ln\left(J^2(1-s)^2 + \varepsilon^2\right)\left(J^2(1-s)^2 + \varepsilon^2\right) \right.
$$
$$
\left. \left. -J^2(1-s)^2 \right) \right|_{s=0}^{s=1}
\tag{4.70}
$$

Taking into account limits and integral bounds, singular integral is calculated as

$$
\begin{aligned}
\mathcal{I}_{i1}^{1,i-1} &= \frac{1}{8J\pi} \left(2\ln\left(J\left(1-s\right)\right) \left(J^2\left(1-s\right)^2\right) - J^2\left(1-s\right)^2 \right) \Bigg|_{s=0}^{s=1} \\
&= \frac{1}{8J\pi} \left(-2\ln(J)J^2 + J^2 \right) \\
&= \frac{J}{8\pi} \left(1 - 2\ln(J) \right).
\end{aligned}
\tag{4.71}
$$

Singular integral of G_L with shape function ψ_2

$$
\begin{aligned}
\mathcal{I}_{i2}^{1,i-1} &= \int_0^1 \psi_2(s) G_L\left(P_{\varepsilon,i}, T(s)\right) J \, \mathrm{d}s \\
&= -\frac{J}{4\pi} \int_0^1 s\ln(r^2) \, \mathrm{d}s \\
&= -\frac{J}{4\pi} \lim_{\varepsilon\to 0} \int_0^1 s\ln(J^2(1-s)^2 + \varepsilon^2) \, \mathrm{d}s.
\end{aligned}
\tag{4.72}
$$

Symbolic integration now results with

$$
\begin{aligned}
\mathcal{I}_{i2}^{1,i-1} = -\frac{1}{8J\pi} \lim_{\varepsilon\to 0} &\left(4J\varepsilon \arctan\left(\frac{J(s-1)}{\varepsilon}\right) - J^2 s^2 - 2J^2 s \right. \\
&\left. + \ln\left(J^2(s-1)^2 + \varepsilon^2\right) \left(J^2(s-1)(s+1) + \varepsilon^2\right) \right) \Bigg|_{s=0}^{s=1}
\end{aligned}
\tag{4.73}
$$

Taking into account limits and integral bounds, singular integran can be calculated as

$$
\begin{aligned}
\mathcal{I}_{i2}^{1,i-1} &= -\frac{1}{8J\pi} \left(-J^2 s^2 - 2J^2 s + \ln\left(J^2(s-1)^2\right) \left(J^2\left(s^2-1\right)\right) \right) \Bigg|_{s=0}^{s=1} \\
&= -\frac{1}{8J\pi} \left(2\ln(J)J^2 - 3J^2 \right) \\
&= \frac{J}{8\pi} \left(3 - 2\ln(J) \right).
\end{aligned}
\tag{4.74}
$$

Singular integral of $\partial G_L / \partial \boldsymbol{n}$ with shape function ψ_1

$$
\mathcal{I}_{i1}^{2,i-1} = \int_0^1 \psi_1(s) \frac{\partial G_L}{\partial \boldsymbol{n}} \left(P_{\varepsilon,i}, T(s)\right) J \, \mathrm{d}s
$$

$$= -\frac{J}{2\pi} \int_0^1 (1-s)\frac{\boldsymbol{r} \cdot \boldsymbol{n}}{r^2}\,\mathrm{d}s$$

$$= \frac{J}{2\pi} \lim_{\varepsilon \to 0} \int_0^1 (1-s)\frac{\varepsilon}{J^2(1-s)^2 + \varepsilon^2}\,\mathrm{d}s. \tag{4.75}$$

Symbolic integration results with

$$\mathcal{I}_{i1}^{2,i-1} = -\frac{J}{2\pi} \lim_{\varepsilon \to 0} \left.\frac{\varepsilon \ln\left(J^2\left(s-1\right)^2 + \varepsilon^2\right)}{2J^2}\right|_{s=0}^{s=1}, \tag{4.76}$$

which after taking limit into account, results with

$$\mathcal{I}_{i1}^{2,i-1} = 0. \tag{4.77}$$

Singular integral of $\partial G_L/\partial \boldsymbol{n}$ with shape function ψ_2

$$\begin{aligned}\mathcal{I}_{i2}^{2,i-1} &= \int_0^1 \psi_2(s)\frac{\partial G_L}{\partial \boldsymbol{n}}\left(P_{\varepsilon,i}, T(s)\right) J\,\mathrm{d}s \\ &= -\frac{J}{2\pi} \int_0^1 s\frac{\boldsymbol{r} \cdot \boldsymbol{n}}{r^2}\,\mathrm{d}s \\ &= \frac{J}{2\pi} \lim_{\varepsilon \to 0} \int_0^1 s\frac{\varepsilon}{J^2(1-s)^2 + \varepsilon^2}\,\mathrm{d}s.\end{aligned} \tag{4.78}$$

Symbolic integration results with

$$\mathcal{I}_{i2}^{2,i-1} = \frac{J}{2\pi} \lim_{\varepsilon \to 0} \left.\left(\frac{\arctan\left(\frac{J(s-1)}{\varepsilon}\right)}{J} + \frac{\varepsilon \ln\left(J^2\left(s-1\right)^2 + \varepsilon^2\right)}{2J^2}\right)\right|_{s=0}^{s=1}. \tag{4.79}$$

Limits and integral bounds are utilized to calculate final value as

$$\mathcal{I}_{i2}^{2,i-1} = \frac{J}{2\pi} \cdot \frac{\pi}{2J} = \frac{1}{4}. \tag{4.80}$$

4.4.3 Regular integrals

When the element E_j over which the integration in $\mathcal{I}_{ik}^{1,j}$ or $\mathcal{I}_{ik}^{2,j}$ occurs does not incorporate collocation point P_i, the integral is regular (all white cells in illustrated matrix in Fig. 4.3 contain only regular integrals) and any standard quadrature method can be used. Here, the Gauss quadrature with four integration points is used.

Table 4.1

Values of weight and node positions for 4-point Gaussian quadrature.

Number g	Node position ζ_g	Weight w_g
1	$\frac{1}{2} - \frac{1}{2}\sqrt{\frac{3}{7} + \frac{2}{7}\sqrt{\frac{6}{5}}}$	$\frac{18 - \sqrt{30}}{72}$
2	$\frac{1}{2} - \frac{1}{2}\sqrt{\frac{3}{7} - \frac{2}{7}\sqrt{\frac{6}{5}}}$	$\frac{18 + \sqrt{30}}{72}$
3	$\frac{1}{2} + \frac{1}{2}\sqrt{\frac{3}{7} - \frac{2}{7}\sqrt{\frac{6}{5}}}$	$\frac{18 + \sqrt{30}}{72}$
4	$\frac{1}{2} + \frac{1}{2}\sqrt{\frac{3}{7} + \frac{2}{7}\sqrt{\frac{6}{5}}}$	$\frac{18 - \sqrt{30}}{72}$

The regular integrals are therefore solved as

$$
\begin{aligned}
\mathcal{I}_{ik}^{1,j} &= \int_0^1 \psi_k(s) G_L\left(P_i, T(s)\right) J \, \mathrm{d}s \\
&= J \sum_{g=1}^4 w_g \psi_k(\zeta_g) G_L\left(P_i, T(\zeta_g)\right),
\end{aligned}
\tag{4.81}
$$

$$
\begin{aligned}
\mathcal{I}_{ik}^{2,j} &= \int_0^1 \psi_k(s) \frac{\partial G_L}{\partial \boldsymbol{n}}\left(P_i, T(s)\right) J \, \mathrm{d}s \\
&= J \sum_{g=1}^4 w_g \psi_k(\zeta_g) \frac{\partial G_L}{\partial \boldsymbol{n}}\left(P_i, T(\zeta_g)\right),
\end{aligned}
\tag{4.82}
$$

while values of weights w_g and node positions ζ_g can be found in Table 4.1 (values can be found in [61]).

4.5 Validation

In order to validate proposed approach for calculating added inertia matrix, analytic solutions for added inertia values for simple forms will be used. All solutions are taken for two dimensional forms with unit thickness, due to availability of data in literature and unit density for simplicity, since this has no effect on solutions because density only causes linear scaling of all added inertia component values.

First form considered is unit circle, as the simplest form possible, for which the analytical added inertia matrix is equal to [63]

$$
\boldsymbol{M_{unit\_circle}} = \begin{pmatrix} \pi & 0 & 0 \\ 0 & \pi & 0 \\ 0 & 0 & 0 \end{pmatrix}.
\tag{4.83}
$$

The proposed algorithm is validated on the two non-zero values and the relative error is reported in diagrams. Relative error is calculated as

$$E_{rel} = \left| \frac{m_{numeric} - m_{analytic}}{m_{analytic}} \right|, \qquad (4.84)$$

where $m_{numeric}$ represents numerically calculated value of the analyzed added inertia component, while $m_{analytic}$ stands for the respective analytic solution.

The convergence of the numeric solution towards analytically calculated value is presented in Fig. 4.6 for two non-zero added inertia components and for number of elements ranging from $N = 20$ to $N = 480$. It can be concluded that numeric solution quickly converges to the analytic, and it took only 100 boundary elements to converge under 2% relative error.
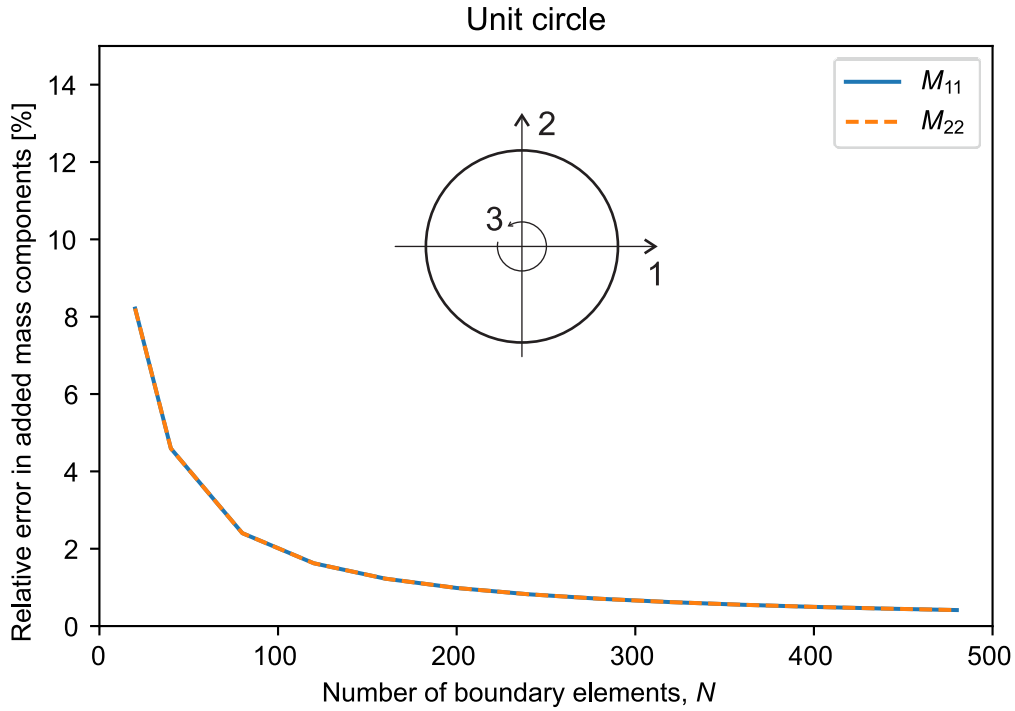

Figure 4.6: Relative error of non-zero added inertia components, with respect to the number of boundary elements used on the example of unit circle.

A bit more complicated second analyzed test case is ellipse with semi-major and semi-minor axes equal to $a = 3$ in x direction and $b = 1$ in y direction, for which the analytic

added inertia matrix can be calculated as [63]

$$\boldsymbol{M_{ellipse}} = \begin{pmatrix} \pi b^2 & 0 & 0 \\ 0 & \pi a^2 & 0 \\ 0 & 0 & \frac{1}{8}\pi\left(a^2 - b^2\right)^2 \end{pmatrix} = \begin{pmatrix} \pi & 0 & 0 \\ 0 & 9\pi & 0 \\ 0 & 0 & 8\pi \end{pmatrix}. \tag{4.85}$$

The convergence of numeric solution towards analytic is similarly presented for growing number of elements (again ranging from $N = 20$ to $N = 480$) and now for three non-zero added inertia components in Fig. 4.7. The convergence was a bit slower, when compared to the unit circle, but nevertheless the solution quickly converged to under 2% relative error.
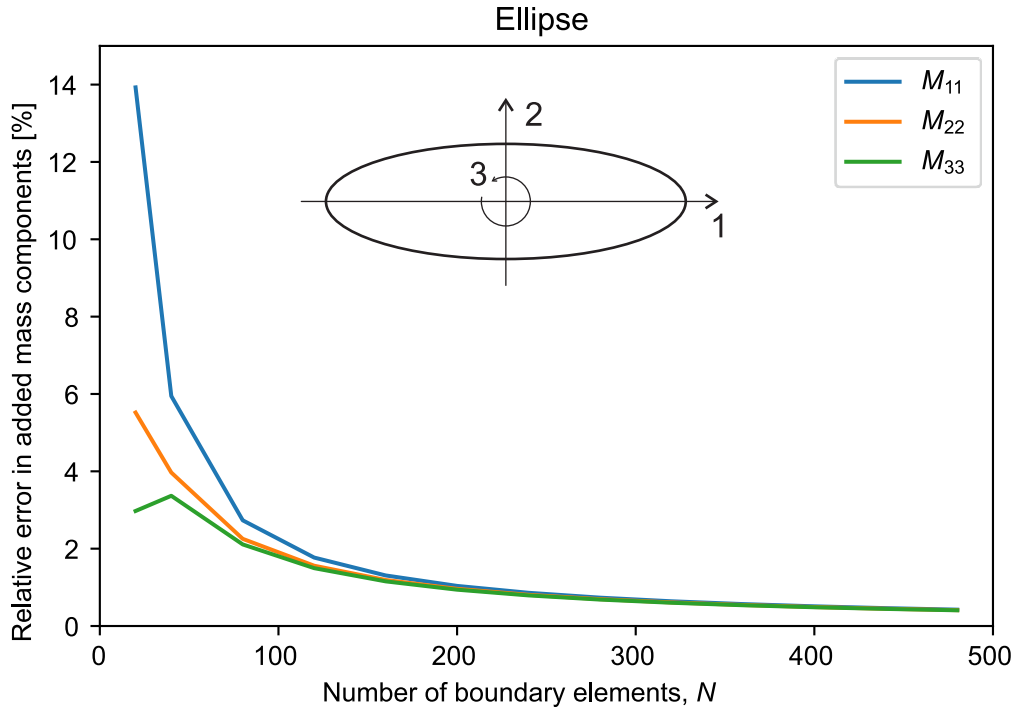

Figure 4.7: Relative error of non-zero added inertia components, with respect to the number of boundary elements used on the example of ellipse with semi-major and semi-minor axes equal to $a = 3$ and $b = 1$.

The first two test cases analyzed involved blunt shapes, without sharp edges, which may often arise in flapping airfoil modeling. Therefore, in order to validate the method for sharp-edged shapes, the first (simplest) test case with sharp edges analyzed is unit

square, for which the added inertia matrix can be calculated as [63]

$$\boldsymbol{M_{unit\_square}} = \begin{pmatrix} 4.754 & 0 & 0 \\ 0 & 4.754 & 0 \\ 0 & 0 & 0.725 \end{pmatrix}. \tag{4.86}$$

The convergence of numeric solution is again presented for boundary elements number ranging from $N = 20$ to $N = 480$, for three non-zero added inertia components in Fig. 4.8. The convergence for translational components was very fast and only $N = 20$ boundary elements (smallest number tested) was enough to almost exactly represent added mass. On the other hand, rotational component converged a bit slower, but nevertheless converged towards analytic solution relatively fast.
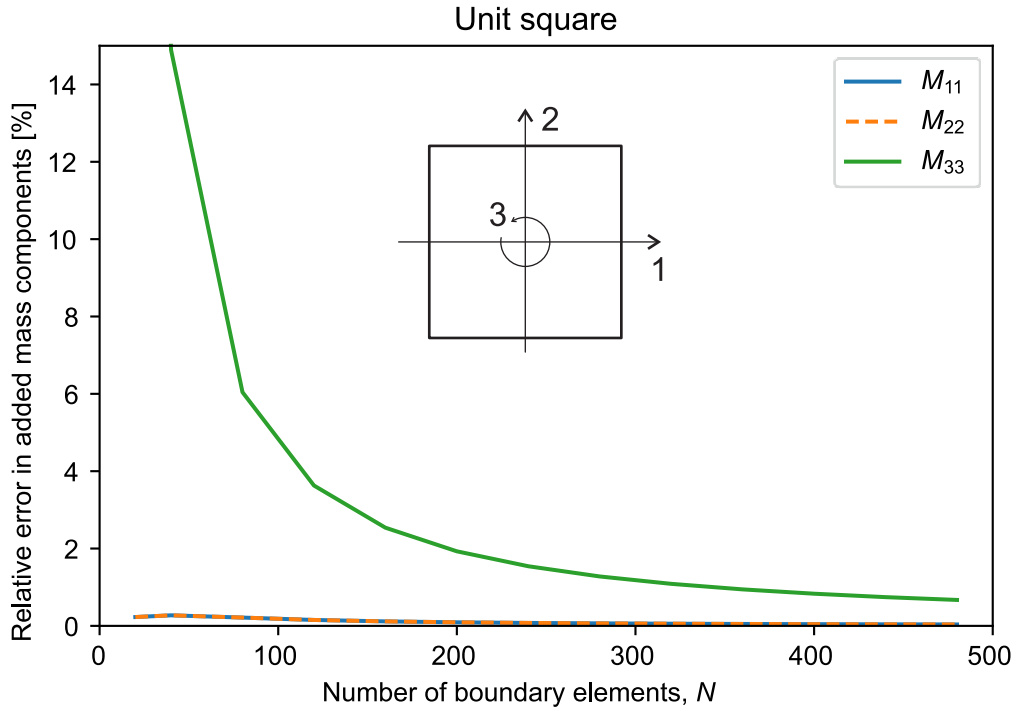

Figure 4.8: Relative error of non-zero added inertia components, with respect to the number of boundary elements used on the example of unit square.

Finally, the rectangle with large aspect ratio (side lengths equaling $a = 40$ and $b = 1$) is analyzed. However, no closed form solutions for the rectangle have been found, but analytical solution for the second translational (largest) component is found to be equal to [64]

$$\boldsymbol{M_{rectangle,22}} = \frac{1}{4} \cdot 1.05\pi a^2 = 420\pi. \tag{4.87}$$

The convergence is now presented only for the known second value of added inertia, again for boundary elements number ranging from $N = 20$ to $N = 480$ in Fig. 4.9. It can be noticed that the value again very rapidly converged towards almost exact solution.
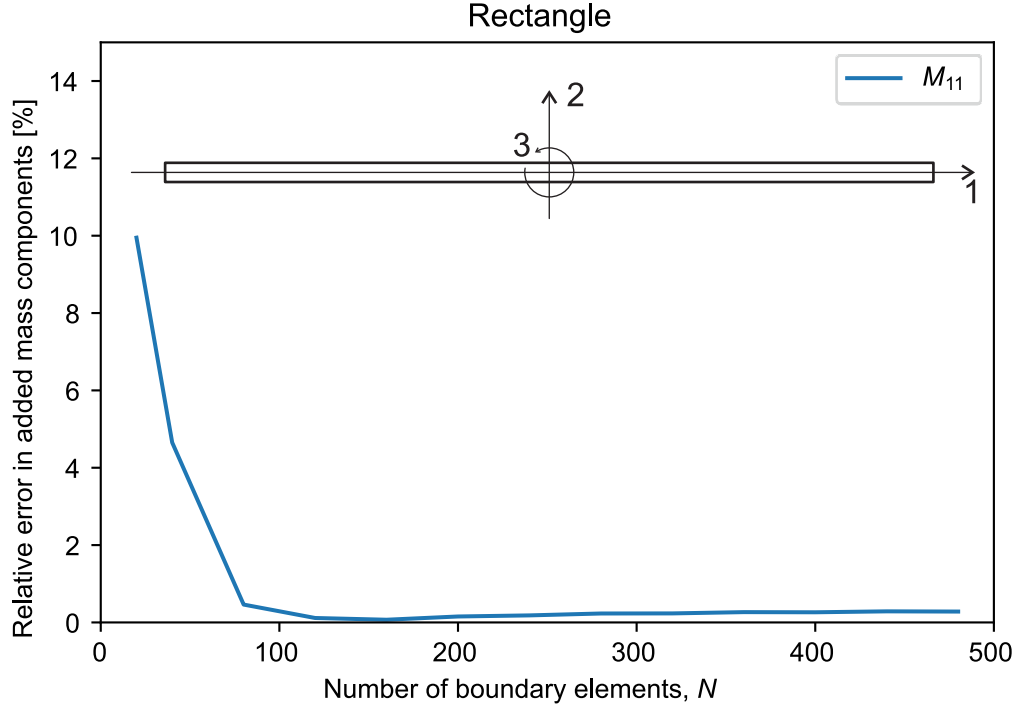

Figure 4.9: Relative error of non-zero added inertia components, with respect to the number of boundary elements used on the example of rectangle with large aspect ratio (side lengths equal to $a = 40$ and $b = 1$).

Vorticity effects

5.1 Introduction

This section focuses on modeling viscous aerodynamic effects on the insect-type flapping wings. As already mentioned, due to the high flapping frequency (large Strouhal number), thick boundary layer is not formed on the wing surface and boundary layer-induced forces can usually be neglected, although the low Reynolds number involved suggests otherwise. To this end, the viscous effects will be captured by modeling unsteady vortex wake, shed by the flapping wings, only. Mathematically, this leads to the Helmholtz-Hodge decomposition of fluid velocity into curl-free and divergence-free parts, as follows

$$\boldsymbol{u} = \nabla\phi + \nabla \times \boldsymbol{\Psi}, \tag{5.1}$$

where ϕ corresponds to the velocity potential introduced and described in Chapter 4, while Ψ is equal to

$$\boldsymbol{\Psi} = \begin{pmatrix} 0 \\ 0 \\ \psi_v \end{pmatrix}, \tag{5.2}$$

where ψ_v represents stream function.

The vortex wake has influence only on the second term in (5.1), while the effects of first term are modeled in Chapter 4. It is important to emphasize that $\nabla\phi$ and $\nabla \times \boldsymbol{\Psi}$ represent orthogonal components of fluid velocity and therefore the effects of each term can be modeled separately and effects added - no aerodynamic effect is therefore modeled twice.

Insect-type flapping aerodynamics is characterized by vortex shedding from leading

edge, considered as an important phenomenon for increasing lift [1] or preventing stall [4], together with the trailing edge vortex shedding, present also in the conventional fixed-wing aerodynamics.

Effects of the vortex wake on a multibody system are expressed as an external aerodynamic load $\boldsymbol{Q_{vort}}$ in (3.36). This chapter focuses on description of the method for vortex wake modeling and calculation of aerodynamic load $\boldsymbol{Q_{vort}}$.

It is important to note again, as explained after symplectic reduction is introduced in (3.1), that introduction of the vorticity effects via load vector $\boldsymbol{Q_{vort}}$ does not compromise previously utilized symplectic reduction of the Hamiltonian system, reducing out fluid variables, since the equivalent reduction can be performed at different level of circulation. Therefore, derived equations of motion remain valid even after introduction of the vorticity effects.

Vortex wake consists of irrotational point vortices and the proposed method for vorticity effects modeling is inspired by lumped-vortex element method presented in [65]. However, the approach taken here is tailored for utilization in insect-type aerodynamics modeling. One step in algorithm loop consists of wake evolution step, where vortex wake positions and intensities are updated, vortex shedding steps, modeling shedding of new point vortex from both leading and trailing edge of the wing and final step calculating aerodynamic load induced by current vortex wake. Algorithm tasks are illustrated by flowchart in Fig. 5.1 and explained in respective sections.

5.2 Discretization

The cross sections of flapping wing airfoils are generally very thin, with wing thickness being less than 5% of wing chord. Therefore, the wing section is here considered as a line (infinitely thin airfoil), but shape discretization can easily be incorporated if needed for certain application, with all discussion presented here staying the same.

Each vortex element consists of a vortex that is constantly attached at $\frac{1}{4}$ of element length and moves together with element and collocation point at $\frac{3}{4}$ of vortex element, at which the boundary conditions are enforced. The illustration of wing dicretized with N_v vortex elements is presented in Fig. 5.2. In addition to vortex elements and nodes, the figure also includes the illustration of newly shed vortex from both leading and trailing edge.
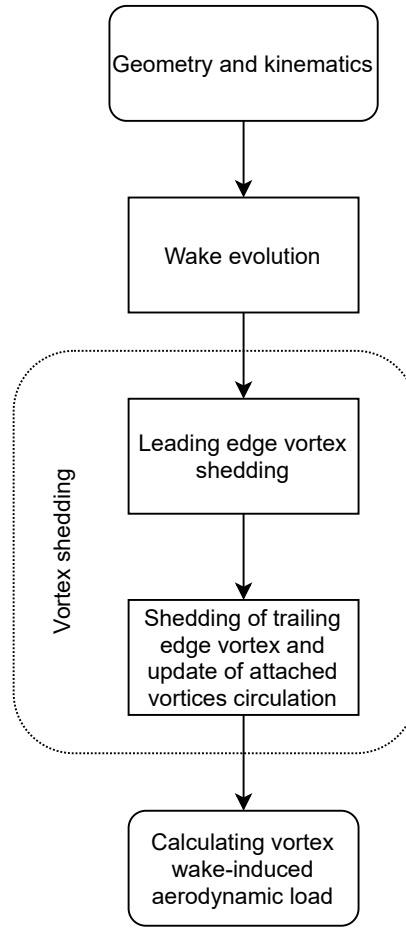
Figure 5.1: Flowchart illustrating tasks involved in one time step of vortex effects modeling algorithm.

5.3 Wake evolution

The irrotational point vortices in vortex wake are considered "free" and having no inertia, i.e. point vortices move according to the velocity at center point. The velocity at vortex point is induced by all attached and all other "free" wake vortices.

Irrotational point vortices by definition (in order to satisfy generation of irrotational flow) induce velocity in the form [66]

$$\|\boldsymbol{v_{in}}\| = \frac{\Gamma}{2\pi r},\tag{5.3}$$

where Γ represents vortex circulation, while r presents distance from the vortex center point.

However, in order to reduce numerical issues with instability near the vortex center point (when $r \to 0$) due to the singularity, the vortex core in which the induced velocity
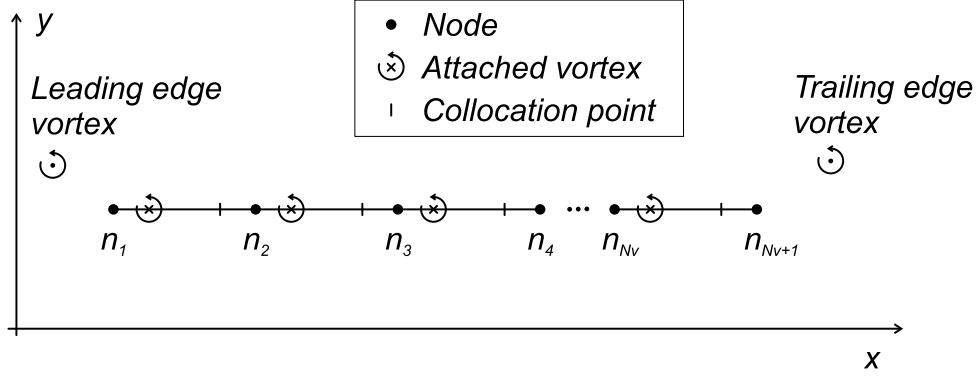
Figure 5.2: Illustration of thin flapping airfoil disretization with N_v vortex elements, each consisting of attached vortex and collocation point, together with newly shed vortex from both leading and trailing edge.

does not change is introduced. In the vortex core, the velocity is constant and equal to the velocity at the core boundary. Therefore, as illustrated in Fig. 5.3, the velocity induced at position P_i by irrotational point vortex V_i, with circulation Γ_i, is equal to

$$
\boldsymbol{v_{in}}\left(P_i, V_i\right) = \begin{cases} \frac{\Gamma_i}{2\pi\|\boldsymbol{r_i^v}\|^2} \begin{pmatrix} -r_{iy}^v \\ \\ r_{ix}^v \end{pmatrix}, & \text{if } \|\boldsymbol{r_i^v}\| > r_c^v, \\ \\ \frac{\Gamma_i}{2\pi r_c^v \|\boldsymbol{r_i^v}\|} \begin{pmatrix} -r_{iy}^v \\ \\ r_{ix}^v \end{pmatrix}, & \text{if } \|\boldsymbol{r_i^v}\| \le r_c^v, \end{cases}
\tag{5.4}
$$

where $\boldsymbol{r_i^v}$ is distance vector from vortex center point to position at which the velocity is induced, calculated as

$$
\boldsymbol{r_i^v} = \boldsymbol{p^{P_i}} - \boldsymbol{p^{V_i}},
\tag{5.5}
$$

where $\boldsymbol{p^{V_i}}$ is vortex position and $\boldsymbol{p^{P_i}}$ is position of point P_i. Vortex core radius is here set to be equal to $r_c^v = 10^{-8}$.

The overall velocity of each vortex can now be calculated as

$$
\boldsymbol{v_i^{vor}} = \sum_{j=1}^{N_v} \boldsymbol{v_{in}}\left(W_i, V_j\right) + \sum_{j=1, j \ne i}^{N_w} \boldsymbol{v_{in}}\left(W_i, W_j\right), \quad \text{for } i = 1, 2, ..., N_w,
\tag{5.6}
$$

where W_i represents i-th "free" vortex, while V_j represents j-th attached vortex and N_w is total number of point vortices in vortex wake at a current time step. The velocity at infinity is here taken to be zero $\boldsymbol{v_\infty} = \boldsymbol{0}$, without any loss of generality, since any velocity at infinity can be added to the current body velocity.
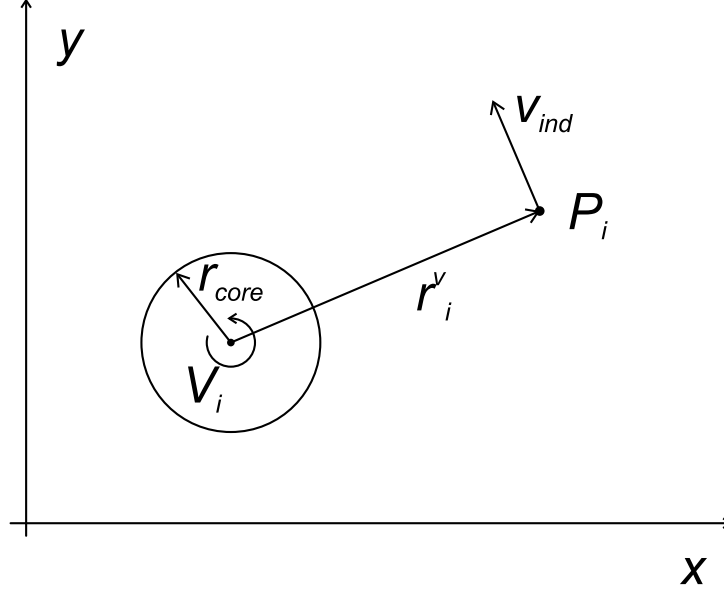
Figure 5.3: Illustration of velocity induced by irrotational point vortex at a distance larger than vortex core radius.

The (updated) position of each wake vortex in time step t can now be calculated as

$$\boldsymbol{p}_i^{vor}(t) = \boldsymbol{p}_i^{vor}(t-1) + \Delta t \cdot \boldsymbol{v}_i^{vor}, \text{ for } i = 1, ..., N_w,\tag{5.7}$$

where Δt represents time step size.

The vortex wake dissipation is neglected and each vortex has a constant circulation from the time it is shed from the wing edge. Therefore, wake vortex circulation in time step t is calculated as

$$\Gamma_i^w(t) = \Gamma_i^w(t-1), \text{ for } i = 1, ..., N_w.\tag{5.8}$$

5.4 Vortex shedding

In order to realistically model insect-type flapping aerodynamics, vortex wake is shed from both leading and trailing wing edge. In the proposed algorithm, vortex is first shed from the leading edge and subsequently trailing edge vortex shedding is performed in conjunction with the update of attached vortex ciruclations, as described in following subsections.

5.4.1 Leading edge vortex shedding

The idea for leading edge vortex (LEV) shedding is found in [67]. However, the method proposed here does not involve any time step-dependent factors, that may induce instabilities and result divergence in the case of highly unsteady flows, pertinent to insect-type flapping aerodynamics.

A newly shed LEV is placed on the line traveled by wing leading edge from the last time step, but closer to the current edge position. To be more precise, new LEV is placed at a 0.3 distance traveled, measured from the current edge position, leading to the expression for calculating position of new LEV, created in time step i

$$\boldsymbol{p}_i^{LEV} = \boldsymbol{p}_i^{LE} + 0.3 \cdot \left(\boldsymbol{p}_{i-1}^{LE} - \boldsymbol{p}_i^{LE} \right), \tag{5.9}$$

where $\boldsymbol{p}_i^{LE}$ represents position of wing leading edge in time step i.

To understand why the vortex is not placed at the middle of the distance traveled, equation (5.3) should be taken into account. If more than one time step is considered for the same distance traveled, with one shed vortex for each time step, due to the nonlinearity of expression (5.3), vortex influence on the induced velocity exponentially drops with distance. If one vortex with circulation equal to the overall sum of all vortex circulations is to be placed at the middle point of the distance, the overall influence of the vortex wake would be underestimated. To mitigate this issue numerically, position in the range between 0.2 and 0.3 distance traveled is usually used [65].

The circulation of this newly shed vortex is determined from the circulation of the attached vortex, closest to the leading edge, in previous time step. Informally, this can be considered as releasing part of the attached circulation from the leading part of airfoil into the wake. However, as the experimental data and previous experience suggest, LEV is not released into the wake for small angles of attack, and therefore threshold for LEV shedding is introduced. Circulation of the newly created LEV can therefore be calculated as

$$\begin{aligned} \Gamma_{LEV} &= 0, & \text{if } \ \alpha < \alpha_{th}, \\ \Gamma_{LEV} &= \frac{\Gamma_1}{2}, & \text{if } \ \alpha \geq \alpha_{th}, \end{aligned} \tag{5.10}$$

where α represents instantaneous angle of attack, while α_{th} represents threshold for shed-

ding leading edge vortex (chosen to be $\alpha_{th} = \frac{\pi}{4}$ in the proposed algorithm).

5.4.2 Trailing edge vortex shedding and update of attached vortex circulations

After releasing LEV in the wake, new trailing edge vortex (TEV) can be created and attached vortices updated to satisfy boundary and physical conditions. Calculation of new TEV circulation and updating attached vortex circulations is coupled task, requiring satisfaction of two conditions: non-penetrability condition on the surface and Kelvin circulation theorem.

Non-penetrability condition introduced in Chapter 4 by expression (4.11) ensured that the first component in the Helmholtz-Hodge decomposition (5.1) of fluid velocity did not generate non-physical "leaks" of the fluid through the surface. Equivalently, the second component of Helmholtz-Hodge decomposition is required to generate only tangential flow in vortex elements' collocation points. To this end, non-penetrability condition of the vortical part of fluid flow is introduced as

$$\left(\sum_{j=1}^{N_v} \boldsymbol{v_{in}}\left(C_i, V_j \right) + \sum_{j=1}^{N_w} \boldsymbol{v_{in}}\left(C_i, W_j \right) \right) \cdot \boldsymbol{n_i} = (\boldsymbol{v} + \boldsymbol{\omega} \times \boldsymbol{r_i^c}) \cdot \boldsymbol{n_i},$$

$$\text{for } i = 1, 2, ..., N_v, \qquad (5.11)$$

where C_i represents ith collocation point, $\boldsymbol{v}$ and $\boldsymbol{\omega}$ represent wing translational and angular velocity, while $\boldsymbol{r_i^c}$ represents distance vector from body center of mass to collocation point i. The velocity at infinity $\boldsymbol{v_\infty}$ is again neglected here, and all translational velocity is accounted for by body velocity $\boldsymbol{v}$.

On the other hand, Kelvin circulation theorem, requiring that the overall circulation of the multibody-fluid coupled system be preserved, was inherently satisfied by first component in the Helmholtz-Hodge decomposition (5.1) of fluid velocity, since no circulation is generated at all. However, the second component of Helmholtz-Hodge decomposition causes the circulation about the body (due to attached vortices) and in the surrounding fluid (due to "free" wake vortices) to be non-zero. These circulations have to be balanced, leading to another constraint in the form

$$\sum_{j=1}^{N_v} \Gamma_j + \sum_{j=1}^{N_w} \Gamma_j^w = 0, \qquad (5.12)$$

where Γ_j represents circulation of j-th attached vortex, while Γ_j^w represents circulation of j-th wake vortex.

The Kelvin circulation theorem, represented in the algorithm by constraint (5.12), is a direct consequence of vorticity advection condition, i.e. $\text{Diff}_{\text{vol}}(\mathcal{F})$ invariance of the momentum map $J_{\mathcal{F}}$ introduced in (3.1).

Similarly as the LEV, the TEV is placed on the line travel by trailing edge since the previous time step, and again at 0.3 distance for the same reasons discussed for LEV. The position of new TEV can therefore be calculated as

$$\boldsymbol{p}_i^{TEV} = \boldsymbol{p}_i^{TE} + 0.3 \cdot \left(\boldsymbol{p}_{i-1}^{TE} - \boldsymbol{p}_i^{TE}\right), \tag{5.13}$$

where $\boldsymbol{p}_i^{TE}$ represents position of wing trailing edge in time step i.

Since the end of last time step, when both boundary condition and Kelvin circulation theorem were satistfied, new LEV and TEV are shed into wake and the wake vortex positions are updated. The circulation of LEV is known, while the circulation of TEV needs to be calculated, together with the new values of circulation for all attached vortices, leading to $N_v + 1$ unknowns. N_v equations arise from the non-penetrability boundary condition (5.11) in the from

$$\left(\sum_{j=1}^{N_v} \boldsymbol{v_{in}}\left(C_i, V_j\right)\Big|_{\Gamma_j=1} \Gamma_j + \sum_{j=1}^{N_w-1} \boldsymbol{v_{in}}\left(C_i, W_j\right)\Big|_{\Gamma_j^w=1} \Gamma_j^w\right) \cdot \boldsymbol{n_i}$$

$$+ \boldsymbol{v_{in}}\left(C_i, W_{TEV}\right)\big|_{\Gamma_{TEV}=1} \Gamma_{TEV} = \left(\boldsymbol{v} + \boldsymbol{\omega} \times \boldsymbol{r_i^c}\right) \cdot \boldsymbol{n_i}, \quad \text{for } i = 1, 2, ..., N_v,$$

$$\left(\sum_{j=1}^{N_v} \boldsymbol{v_{in}}\left(C_i, V_j\right)\Big|_{\Gamma_j=1} \Gamma_j\right) \cdot \boldsymbol{n_i} + \boldsymbol{v_{in}}\left(C_i, W_{TEV}\right)\big|_{\Gamma_{TEV}=1} \Gamma_{TEV}$$

$$= \left(\boldsymbol{v} + \boldsymbol{\omega} \times \boldsymbol{r_i^c} - \sum_{j=1}^{N_w-1} \boldsymbol{v_{in}}\left(C_i, W_j\right)\Big|_{\Gamma_j^w=1} \Gamma_j^w\right) \cdot \boldsymbol{n_i}, \quad \text{for } i = 1, 2, ..., N_v. \tag{5.14}$$

This system of N_v equations is supplemented with the equation enforcing Kelvin circulation theorem to result with solvable system of $N_v + 1$ equations with $N_v + 1$ unknowns. The equation (5.12) in time step i can be expressed as

$$\sum_{j=1}^{N_v} \Gamma_{j,i} + \sum_{j=1}^{N_{w,i}} \Gamma_{j,i}^w = 0, \tag{5.15}$$

and since the wake circulation change since the previous time step occurred only be-

cause two new vortices are shed (existing vortices do not dissipate in time, as previously described), the equation can be reformulated as

$$\sum_{j=1}^{N_v} \Gamma_{j,i} + \Gamma_{TEV,i} + \Gamma_{LEV,i} + \sum_{j=1}^{N_{w,i-1}} \Gamma_{j,i-1}^{w} = 0. \tag{5.16}$$

The Kelvin circulation theorem was also satisfied in the previous time step, and therefore the overall vortex wake circulation in the previous time step can be replaced by the negative overall attached vortices circulation, leading to the final expression

$$\sum_{j=1}^{N_v} \Gamma_{j,i} + \Gamma_{TEV,i} + \Gamma_{LEV,i} - \sum_{j=1}^{N} \Gamma_{j,i-1} = 0,$$

$$\sum_{j=1}^{N_v} \Gamma_{j,i} + \Gamma_{TEV,i} = \sum_{j=1}^{N} \Gamma_{j,i-1} - \Gamma_{LEV,i}. \tag{5.17}$$

The linear system of equations can now be defined as

$$
\begin{pmatrix}
\boldsymbol{D_{1,1}} & \boldsymbol{D_{1,2}} & \cdots & \boldsymbol{D_{1,N_v}} & \boldsymbol{D_{1,N_v+1}} \\
\boldsymbol{D_{2,1}} & \boldsymbol{D_{2,2}} & \cdots & \boldsymbol{D_{2,N_v}} & \boldsymbol{D_{2,N_v+1}} \\
\vdots & \vdots & \ddots & \vdots & \vdots \\
\boldsymbol{D_{N_v,1}} & \boldsymbol{D_{N_v,2}} & \cdots & \boldsymbol{D_{N_v,N_v}} & \boldsymbol{D_{N_v,N_v+1}} \\
1 & 1 & \cdots & 1 & 1
\end{pmatrix}
\begin{pmatrix}
\Gamma_{1,i} \\
\Gamma_{2,i} \\
\vdots \\
\Gamma_{N,i} \\
\Gamma_{TEV,i}
\end{pmatrix}
\tag{5.18}
$$

$$
=
\begin{pmatrix}
\left(\boldsymbol{v} + \boldsymbol{\omega} \times \boldsymbol{r_1^c} - \sum_{j=1}^{N_w-1} \boldsymbol{v_{in}} \left(C_1, W_j \right) \Big|_{\Gamma_j^w=1} \Gamma_j^w \right) \cdot \boldsymbol{n_1} \\
\left(\boldsymbol{v} + \boldsymbol{\omega} \times \boldsymbol{r_2^c} - \sum_{j=1}^{N_w-1} \boldsymbol{v_{in}} \left(C_2, W_j \right) \Big|_{\Gamma_j^w=1} \Gamma_j^w \right) \cdot \boldsymbol{n_2} \\
\vdots \\
\left(\boldsymbol{v} + \boldsymbol{\omega} \times \boldsymbol{r_{N_v}^c} - \sum_{j=1}^{N_w-1} \boldsymbol{v_{in}} \left(C_{N_v}, W_j \right) \Big|_{\Gamma_j^w=1} \Gamma_j^w \right) \cdot \boldsymbol{n_{N_v}} \\
\sum_{j=1}^{N} \Gamma_{j,i-1} - \Gamma_{LEV,i}
\end{pmatrix},
\tag{5.19}
$$

where $\boldsymbol{D}$ represents $(N_v \times N_v + 1)$ influence matrix, with components equal to

$$\boldsymbol{D_{i,j}} = \boldsymbol{v_{in}} \left(C_i, V_j \right) \Big|_{\Gamma_j=1} \cdot \boldsymbol{n_i}. \tag{5.20}$$

Solving system of equations (5.18) results with value of circulation for the newly shed trailing edge vortex Γ_{TEV}, while all the attached vortex circulations are updated to ensure satisfaction of both non-penetrability (5.11) and Kelvin circulation (5.12) constraints.

5.5 Vortex wake-induced aerodynamic load

The calculation of aerodynamic load induced by vortex wake is based on the Kutta-Joukowski theorem (Kutta-Joukowski force has an interesting interpretation in the geometric mechanics setting, being the result of the curvature of Neumann connection [68]), relating circulation around the airfoil and velocity as [66]

$$F_{def}^{KJ} = \rho v^{KJ} \Gamma, \tag{5.21}$$

where ρ represents fluid density, v^{KJ} is the value of velocity, while Γ represents circulation around wing. The resulting force F_{def}^{KJ} is perpendicular to velocity v^{KJ}.
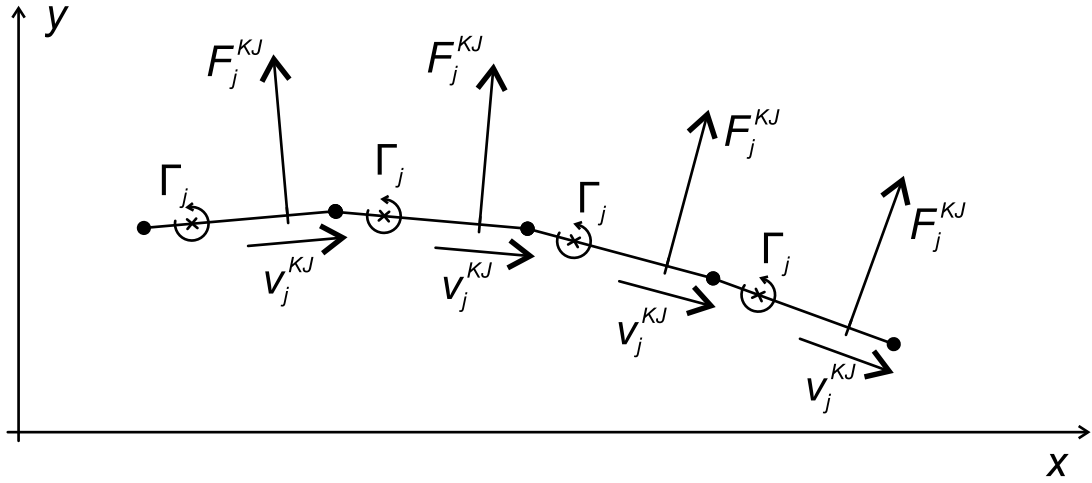

Figure 5.4: Illustration of Kutta Joukowski force calculation for each of the vortex elements, based on the velocity in collocation point and circulation of the attached vortex.

For discretized airfoil, the Kutta-Joukowski force contribution from jth vortex element (illustrated in Fig. 5.4) is then calculated as

$$F_j^{KJ} = \rho v_j^{KJ} \Gamma_j, \tag{5.22}$$

while the fluid velocity at each element collocation point v_j^{KJ} is calculated by combining

body velocity and overall induced velocity (from all atached and "free" vortices) as

$$v_j^{KJ} = \left\| - \boldsymbol{v} - \boldsymbol{\omega} \times \boldsymbol{r_j^c} + \sum_{i=1}^{N_v} \boldsymbol{v_{in}} \left(C_j, V_i \right) + \sum_{i=1}^{N_w} \boldsymbol{v_{in}} \left(C_j, W_i \right) \right\|.$$ (5.23)

The resulting force is perpendicular to the vortex element, since the velocity at collocation point is necessarily tangential to the vortex element (enforced by boundary condition (5.11)). Vortex wake-induced lift and drag force can now be calculated as

$$L^{KJ} = \sum_{j=1}^{N_v} \rho v_j^{KJ} \Gamma_j \cos(\gamma_j),$$ (5.24)

$$D^{KJ} = - \sum_{j=1}^{N_v} \rho v_j^{KJ} \Gamma_j \sin(\gamma_j),$$ (5.25)

where γ_j represents the the angle between vortex element j and x axis.

Numerical experiments

This chapter presents results of numerical experiments aimed to demonstrate performance of proposed insect-type flapping wing aerial vehicle computational model. Both numerical experiments involve fruit fly-like morphology due to the availability of experiments and experimentally fitted parameters for quasi steady aerodynamic models. First test case involves standstill hovering of the fruit fly on Earth, with the flapping pattern as suggested in the literature, involving smooth angle functions. Second test case involves aerial vehicle with fruit fly-like wings, enlarged to enable flight in much thinner Martian atmosphere, with Mars selected due to the recent increased interest in Mars atmospheric flight and flapping wing concept potential in Martian atmosphere. Standstill hovering of this aerial vehicle on Mars is analyzed with flapping pattern characterized by non-smooth angle functions in discrete form, obtained by optimization in previous research.

6.1 Fruit fly-like aerial vehicle hovering

First numerical experiment considered is based on the hovering of the fruit fly (lat. *Drosophila melanogaster*), due to the availability of both numerical results and validated aerodynamic models [69, 27]. The benchmarking aerodynamic model is based on the experiments with dynamically scaled wing and surrounding fluid.

6.1.1 Physical properties

A dynamically scaled apparatus for experiments included a slightly different shape of the wing, compared to *D. melanogaster*, but mostly in the wing root area and the difference shouldn't affect the results significantly [69]. However, descriptions provided in [69, 27] are too basic and insufficient for replicating wing shape. To this end, fruit fly

Table 6.1
Relevant fruit fly model parameters

Notation	Parameter	Value
m_b	main body mass (kg)	9.6×10^{-7}
m_w	wing mass (kg)	2.4×10^{-9}
I_w	Wing inertia matrix $\left(kg \cdot m^2\right)$	$\begin{bmatrix} 2.889 & -8.368 & 0 \\ -8.368 & 48.255 & 0 \\ 0 & 0 & 51.144 \end{bmatrix} \cdot 10^{-16}$
R	wing length (m)	2.5×10^{-3}
b	wing thickness (m)	2.5×10^{-5}
$\bar{c}$	mean chord length (m)	6.7×10^{-4}
$\hat{x}_0$	pitching axis position (in chord lengths)	0.25
ρ	air density $\left(kg/m^3\right)$	1.184
C_R	rotational force coefficient	1.55

wing is modeled based on real world fruit fly wing photography. Dimensions of the fruit fly wing on the photography are determined such that the wing length corresponds to the value indicated in [70]. A wing length to thickness ratio, used in [27], is adopted. No reliable data for *D. melanogaster* wing mass has been found in literature and therefore the value of *D. virilis* wing mass [71] is used for analysis. It can be noticed that *D. virilis* wing is slightly larger than *D. melanogaster* wing and therefore probably heavier, but the difference should be negligible. A wing from the photographs, with dimensions determined as explained, is then modeled in CAD software as a homogeneous body to calculate wing inertia values.

Fruit fly main body is modeled as fully symmetrical with center of mass positioned exactly in the middle between wing joints, with main body mass found in [70]. All physical properties pertinent to the aerodynamic modeling are given in Table 6.1.

6.1.2 Kinematics

Fruit fly motion can be described as the motion of the main body, together with the relative motion of each wing with respect to the main body. All entities (main body and wings) are modeled as rigid bodies. To this end, relative motion of each wing with respect to the main body can be described by three relative angles, namely *stroking* angle α describing horizontal motion of the wing, *pitching* angle β describing twist of the wing and *deviation* angle γ describing motion of the wing in the vertical plane. These flapping angles are shown in Fig. 6.1 illustrating fruit fly flapping in three dimensions.
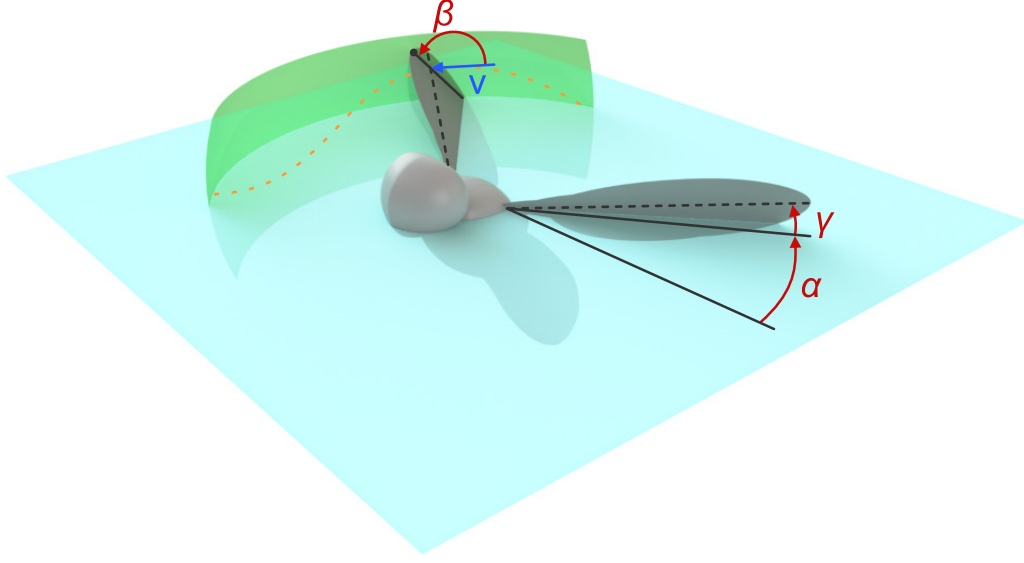
Figure 6.1: Illustration of the fruit fly model flapping, with stroking α, pitching β and deviation γ angles indicated.

Deviation angle γ is taken to be zero during the analyzed test case, in order to enable comparison of results to the results available in literature [27]. The justification for neglecting angle in aerodynamic model utilized in [27] is based on the experimental results in [72], indicating that this angle significantly influences aerodynamic force development over one flapping cycle, but has no significant effect on the value of the overall (cycle-averaged) aerodynamic force. In other words, neglecting deviation angle leads to the different plot of the force value over a flapping cycle, but almost the same value of the average force over a full flapping cycle. In addition to this, high values of flapping frequencies, compared to the fruit fly motion frequency, allow for utilization of cycle-averaged forces instead of instantaneous forces, with negligible loss in accuracy [73]. To this end, wing relative motion is described by stroking α and pitching β angles.

The flapping pattern analyzed is based on a optimal flapping pattern for a fruit fly hovering, obtained in [74]. Stroking angle function $\alpha(t)$ is modeled by smoothed triangular function, which can be described by expression

$$\alpha(t) = \frac{\alpha_m}{\arcsin\left(K_\alpha\right)} \arcsin\left(K_\alpha \sin(2\pi f t)\right),\tag{6.1}$$

where α_m corresponds to the stroking angle amplitude, f represents flapping frequency, while shape of the function is controlled by factor $0 < K_\alpha < 1$. As $K_\alpha \to 1$, angle function $\alpha(t)$ converges towards triangular function, i.e. wing stroking motion is characterized by

Table 6.2
Angle function parameters

Notation	Parameter	Value
α_m	stroking angle amplitude	$\dfrac{\pi}{2}$
K_α	stroking function shape parameter	0.7
β_m	pitching angle amplitude	$\dfrac{7\pi}{18}$
β_a	average pitching value offset	$\dfrac{\pi}{2}$
β_p	pitching phase offset	0
K_β	pitching function shape parameter	2

greater acceleration and deceleration at onset and end of stroke.

Pitching angle evolution in time t is modeled by smoothed trapezoidal function, at flapping frequency f, as

$$\beta(t) = \frac{\beta_m}{\tanh\left(K_\beta\right)} \tanh\left(-K_\beta \cos(2\pi f t + \beta_p)\right) + \beta_a, \tag{6.2}$$

where β_m corresponds to pitching function amplitude, β_p is phase offset, while β_a represents offset of the pitching angle average value. Factor $0 < K_\beta < \infty$ again controls the shape of the function, where as $K_\beta \to \infty$, shape of the function $\beta(t)$ converges towards a step functin, i.e. wing experiences infinite pitching velocities.

The parameters in angle functions (6.1) and (6.2) for the flapping pattern analyzed in this numerical test case are shown in table 6.2.

Hovering with physical properties defined in subsection 6.1.1 at flapping angle functions defined by (6.1) and (6.2) occurs at flapping frequency equal to $f = 167.3$ Hz and the resulting angle functions $\alpha(t)$ and $\beta(t)$ are illustrated in Fig. 6.2 and Fig. 6.3 respectively.
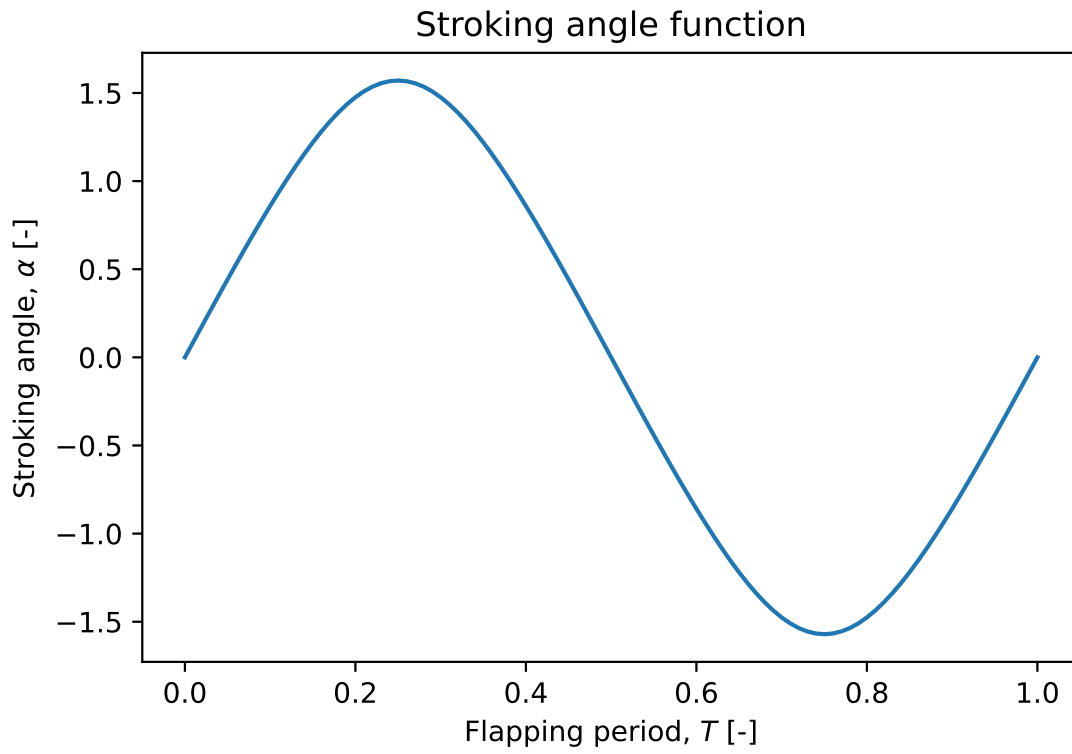
Figure 6.2: Evolution of stroking angle function $\alpha(t)$ over one flapping period for a fruit fly-like aerial vehicle hovering.
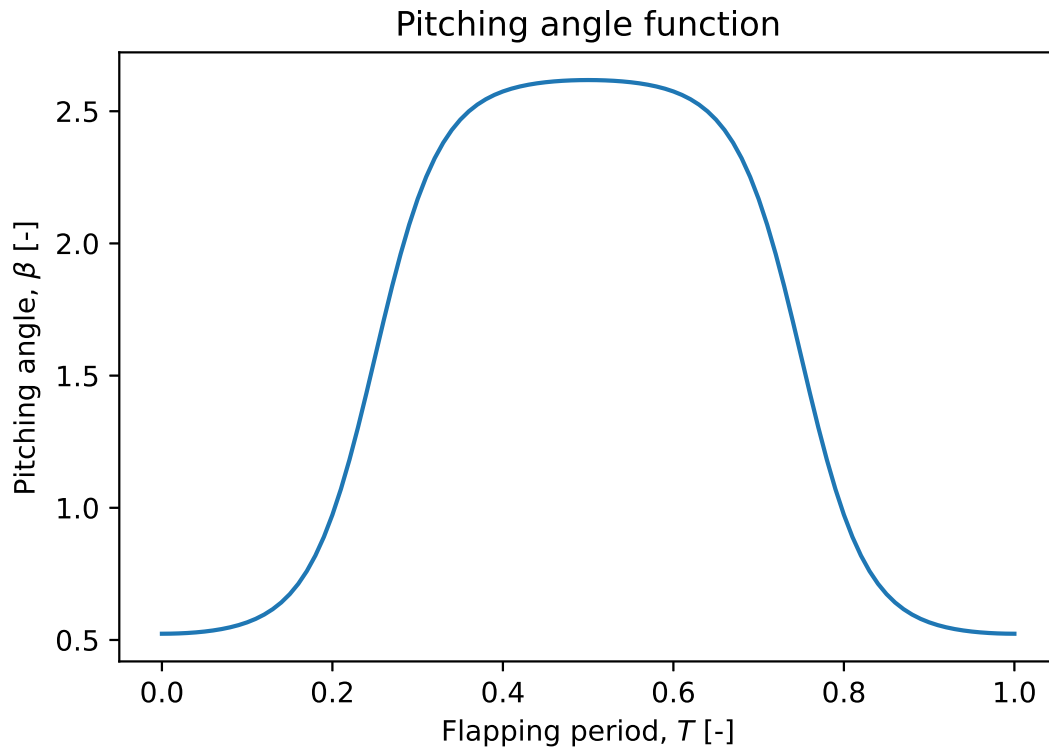

Figure 6.3: Evolution of pitching angle function $\beta(t)$ over one flapping period for a fruit fly-like aerial vehicle hovering.

6.1.3 Aerodynamic phenomena pertinent to fruit fly-like flapping flight

The experiments in [72] indicated that the aerodynamic force on a flapping wing is almost perpendicular to the wing surface at any point in time, leading to the conclusion that the pressure forces are main drivers of aerodynamic load, while the shear forces can mostly be neglected. In addition to this, with the aim of simplifying description of complex aerodynamic phenomena, the insect flight aerodynamics can be decomposed into five smaller aerodynamic phenomena [75]. Aerodynamic phenomena are named: translational circulation, rotational circulation, added mass, wing-wake interaction and clap and fling. Naming of individual aerodynamic phenomena is adopted from [25], where an explanation for the naming is also given.

Translational circulation phenomenon describes effects of stall avoidance due to the creation and reattachment of leading edge vortex (LEV). Stroking at large angles of attack causes the separation of the flow at leading edge of the wing, thus generating a stable vortex - LEV [76]. The reattachment of the flow to the wing is described as a means of avoiding the stall that would occur in the steady flow for the same airfoil at the same angle of attack [77]. The LEV can therefore be thought as increasing the curvature of the wing and therefore circulation, leading to the increase in aerodynamic force [78]. Aerodynamic load stemming from a described phenomenon is denoted by the term translational forces, while the "translational" in the name is utilized to emphasize the fact that these forces are mainly caused by the translational (forward and backward) part of wing motion.

Rotational circulation describes the effect caused by the wing pitching during flapping. Although the lift force value is found to be largest for steady flapping at 45° [73], the increase in angle of attack during flapping causes short, but significant, jump in the lift force. This is caused by slowdown of the fluid below pitching axis and acceleration of the fluid above, driving the increase in LEV volume and creation of trailing edge vortex (TEV). LEV growth leads to the larger circulation, consequently causing larger lift force values. However, in addition to the lift force increase, a significant jump in the drag force can also be observed observed. Since these effects are driven by the wing pitching rotation during flapping, the phenomenon is named rotational circulation and resulting forces rotational forces.

Added mass phenomenon has already been described as the additional inertia "felt" by

the wing because of the acceleration (and deceleration) while submerged in fluid, instead of moving in vacuum. In other words, the wing acceleration inherently causes acceleration in the surrounding fluid, which has to be taken in the account for inertia forces calculation.

Wing-wake interaction phenomenon is used to describe effects of the wing passing through the wake generated during previous flapping cycles. The change between upstroke and downstroke phase causes shedding of LEV and TEV, creating a complex unsteady wake through which wing passes in subsequent stroke phase [79]. This phenomenon may have a significant influence on the aerodynamic forces, and up to 23% of the lift force at certain point can be due to the wing-wake interaction phenomenon [78].

Clap and fling phenomenon describes effects happening due to the wings coming close to each other and then separating. As described in [80], the phenomenon starts as wings decelerate and wing leading edges come close to each other (clap phase). This is followed by the wings pitching about leading edge, squeezing the fluid between wings. After wings become parallel and close to each other over whole chord, fling phase starts by pitching about the trailing edge, creating an "empty" space, that the fluid fills. The phenomenon is highly unsteady and can cause the increase in instantaneous lift force by up to 17% [81].

6.1.4 Quasi steady aerodynamic model used for benchmarking

A benchmarking aerodynamic model [27] is based on the quasi steady algebraic equations for force modeling. The parameters of aerodynamic model have been determined by fitting the quasi steady model results to the experimental measurements, obtained in [72]. Therefore, if the flapping pattern analyzed is similar to flapping pattern used for experimental measurements, model can be used as a benchmarking tool. However, it is important to note that the results are fitted in the cycle-averaged manner, i.e. only the average lift and drag force can be deemed reliable, while the evolution of the force over a flapping cycle is not validated.

It has been shown that three of the five aerodynamic phenomena mentioned in sub-section 6.1.3, namely translational circulation, rotational circulation and added mass, can be well approximated by quasi steady aerodynamic model [27]. On the other hand, quasi steady model is not suitable for modeling highly unsteady phenomena, such as wing-wake interaction and clap and fling. However, as discussed in [73], effects of the highly unsteady aerodynamic phenomena may not have significant influence on the overall cycle-averaged

forces, despite having significant influence at the instantaneous lift and drag force. This is because these effects cause significant change in force at the beginning and end of each stroke, but with effects at the beginning and end often canceling each other. However, this cannot be taken as a general consideration and quasi steady models developed in this manner should be used only for flow condition similar to those used in the experiment, because as shown in [81], the clap and fling phenomenon can significantly increase value of the total lift.

It is also important to note that, although the process of both creation and evolution of LEV is an inherently unsteady process that couldn't be modeled by a quasi steady method, it is demonstrated in [1] that the overall forces caused by LEV can be reliably modeled by quasi steady model (here captured by translational forces modeling).

Quasi steady aerodynamic model utilized here is based has been initially developed in [69] and improved in a number of subsequent papers by the same group of authors and recently in [25].

Translational lift F_{TL} and drag F_{TD} forces are calculated based on the blade element theory, analogous to the approach in [82], leading to the expressions

$$F_{TL} = \int_0^R \frac{1}{2}\rho r^2 \dot{\alpha}^2 c(r) C_{TL}(\delta) dr, , \tag{6.3}$$

$$F_{TD} = \int_0^R \frac{1}{2}\rho r^2 \dot{\alpha}^2 c(r) C_{TD}(\delta) dr, , \tag{6.4}$$

where R corresponds to wing length, ρ represents fluid density, r is the current radial position along the wing, $\dot{\alpha}$ represents stroking velocity, $c(r)$ is the chord length at radial position r from the wing root, while C_{LT} and C_{DT} represent translational lift and drag coefficients. Dependence of coefficients on the angle of attack δ is determined based on the experimental data in [69] and can be expressed as

$$C_{LT}(\delta) = 0.225 + 1.58\sin(2.13\delta - 7.2°), \tag{6.5}$$

$$C_{DT}(\delta) = 1.95 - 1.55\cos(2.04\delta - 9.82°), \tag{6.6}$$

with δ in trigonometric functions expressed in degrees.

On the other hand, no explicit expression for calculating rotational force coefficient is given in [27]. It is discussed that the coefficient depends on two variables, namely

pitching velocity and pitching axis position. However, in the end pitching axis has been fixed (as indicated in table 6.1) and the coefficient value is selected for the combination of selected axis position and highest pitching velocity experienced. This procedure resulted in a constant value of the rotational force coefficient, simplifying calculaton, while having a small effect on accuracy. The rotational force F_R can now, based on the given discussion, be expressed as

$$F_R = \rho C_R R^2 \dot{\alpha} \dot{\beta} \overline{c}^2 \int_0^1 \hat{r} \hat{c}^2 (\hat{r}) \, dr, \tag{6.7}$$

where C_R represents discussed rotational force coefficient (given in table 6.1), $\dot{\beta}$ denotes pitching velocity, $\overline{c}$ is a wing mean chord length, while $\hat{r} = \dfrac{r}{R}$ and $\hat{c} = \dfrac{c}{\overline{c}}$ represent non-dimensional values for radial position along the wing and chord length, respectively.

The added mass force expression can be found in [72] (with the correction of the misprint in the paper, denoting a stroking acceleration where stroking velocity is supposed to be)

$$\begin{aligned} F_A = &\frac{\pi}{4} \rho R^2 \overline{c}^2 \left(\ddot{\alpha} \sin \delta + \dot{\alpha} \dot{\delta} \cos \delta \right) \int_0^1 \hat{r} \hat{c}^2 (\hat{r}) \, dr \\ &- \frac{\pi}{16} \rho \ddot{\delta} \overline{c}^3 R \int_0^1 \hat{c}^2 (\hat{r}) \, dr, \end{aligned} \tag{6.8}$$

where $\ddot{\alpha}$ represents stroking acceleration, while $\dot{\delta}$ and $\ddot{\delta}$ denote angle of attack first and second derivative with respect to time.

6.1.5 Benchmark results

Quasi steady-based aerodynamic model presented in subsection 6.1.4 is applied on the fruit fly-like vehicle flapping with kinematics as introduced in subsection 6.1.2 (flapping anle functions depicted in Fig. 6.2 and Fig. 6.3) to obtain benchmark results for validation of the proposed method. Evolution of the lift and drag force components over one flapping period are presented in Fig. 6.4 and Fig. 6.5 for all three aerodynamic phenomena (described in subsection 6.1.3) captured by quasi steady aerodynamic model. Plots of the overall lift and drag force evolution over one flapping period are given in Fig. 6.6 and Fig. 6.7, respectively, together with designation of the average lift and drag force values.
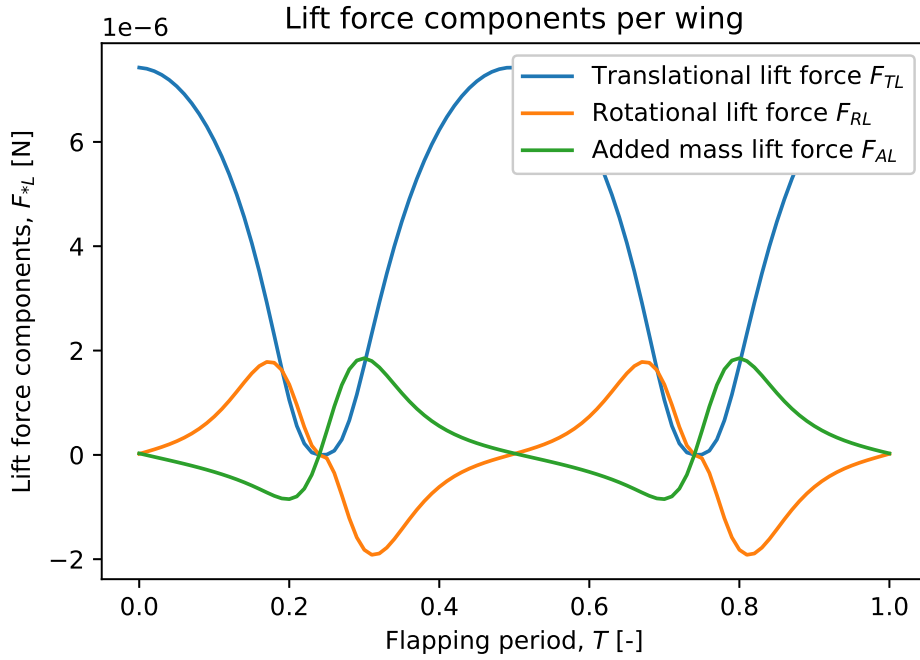
Figure 6.4: Lift force components over one flapping cycle, calculated by quasi steady aerodynamic model for fruit fly-like aerial vehicle flapping with angle functions presented in Fig. 6.2 and Fig. 6.3. Force components values correspond to one wing, while the forces are equal on each wing, due to the symmetrical flapping.
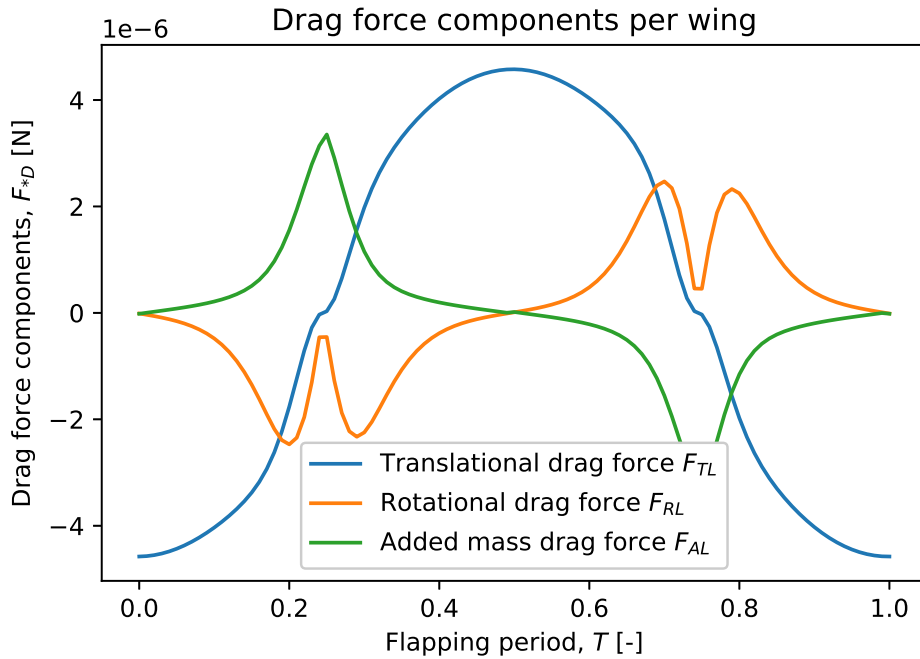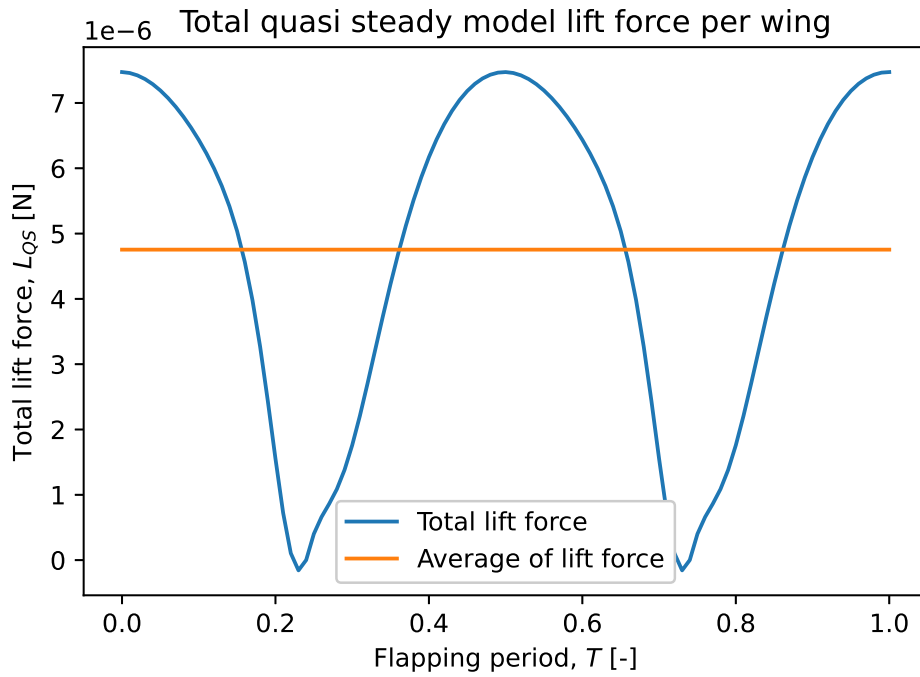

Figure 6.5: Drag force components over one flapping cycle, calculated by quasi steady aerodynamic model for fruit fly-like aerial vehicle flapping with angle functions presented in Fig. 6.2 and Fig. 6.3. Force components values correspond to one wing, while the forces are equal on each wing, due to the symmetrical flapping.

Figure 6.6: Total value of the lift force per one wing, calculated for fruit fly-like vehicle hovering with quasi steady aerodynamic model. Plot includes both total lift force evolution and cycle-averaged lift force value.
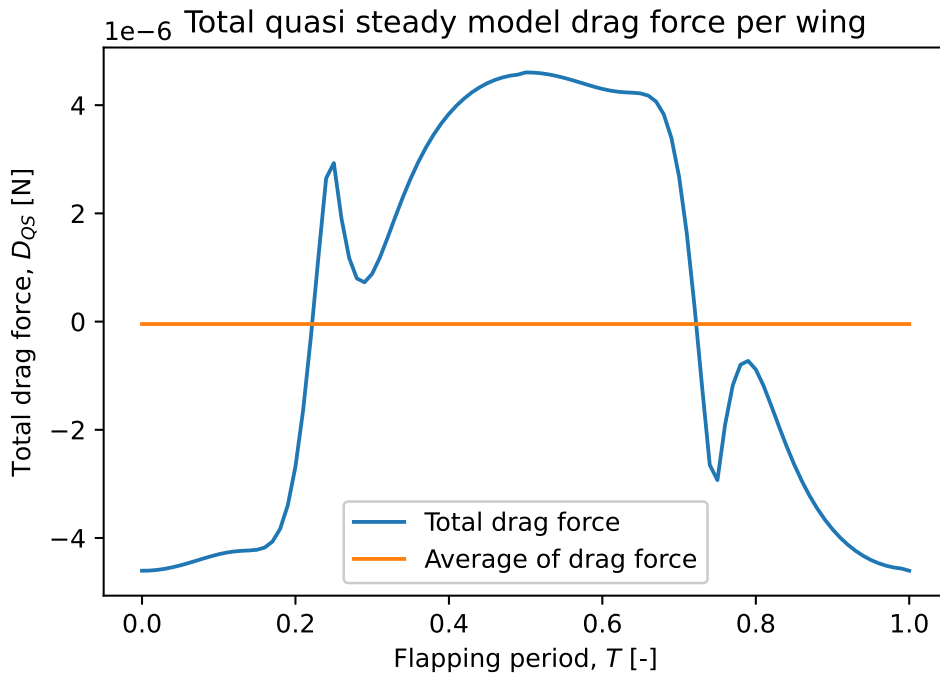
Figure 6.7: Total value of the drag force per one wing, calculated for fruit fly-like vehicle hovering with quasi steady aerodynamic model. Plot includes both total drag force evolution and cycle-averaged drag force value.

As previously explained, quasi steady aerodynamic model is experimentally validated in terms of the average force, while the exact force evolution over a flapping cycle might not be reliable, since certain neglected aerodynamic phenomena might have a significant influence on the force evolution, with negligible influence on average force values (see discussion in subsection 6.1.4).

6.1.6 Results of the analysis with proposed computational model

As introduced, proposed computational model of an insect type flapping wing aerial vehicle consists of two distinct procedures for modeling effects of added inertia (Chapter 4) and vortex wake (Chapter 5), performed in conjunction to model aerodynamics of insect type flapping wing aerial vehicles.

For the purpose of added inertia effects modeling, cross section of the wing is set to be ellipse, due to the unavailability of better fruit fly wing cross section data. The ellipse semi-major axis is equal to half the chord $\dfrac{c}{2}$ at the radial position r along the wing, while the semi-minor axis corresponds to the assumed constant wing thickness (table 6.1). Boundary of the ellipse is discretized with 300 boundary elements. Flapping wing cross section is illustrated in Fig. 6.8, with indication of pitching angle, together with spatial and body-fixed reference frames. Since the vehicle is assumed to be in standstill hovering, coordinate system fixed to the fruit fly like vehicle main body is equivalent to the spatial (fixed) reference frame.

Kinematics of the flapping is introduced in subsection 6.1.2, while each flapping cycle is discretized with 100 time steps. Summing the effects of $\boldsymbol{M_F}\dot{\boldsymbol{v}}$ and $\boldsymbol{Q_{AM}}$ in (3.36) results in the overall aerodynamic load due to the added inertia of the surrounding fluid. Resulting force components and torque, all expressed in the body-fixed reference frame (illustrated in Fig. 6.8 as O'), are shown in Fig. 6.9 and Fig. 6.10.

It may seem from the Fig. 6.9 that the added mass in x' direction is surprisingly zero. However, it is nonzero, but approximately three orders of magnitude smaller than the added mass y' components, due to the high ellipse eccentricity (large ratio between semi-major and semi-minor axis). After taking into account the orientation of the flapping wing in each time step, the lift and drag added mass components (added mass forces in x and y direction on Fig. 6.8), can be calculated resulting in plot shown in Fig. 6.11.
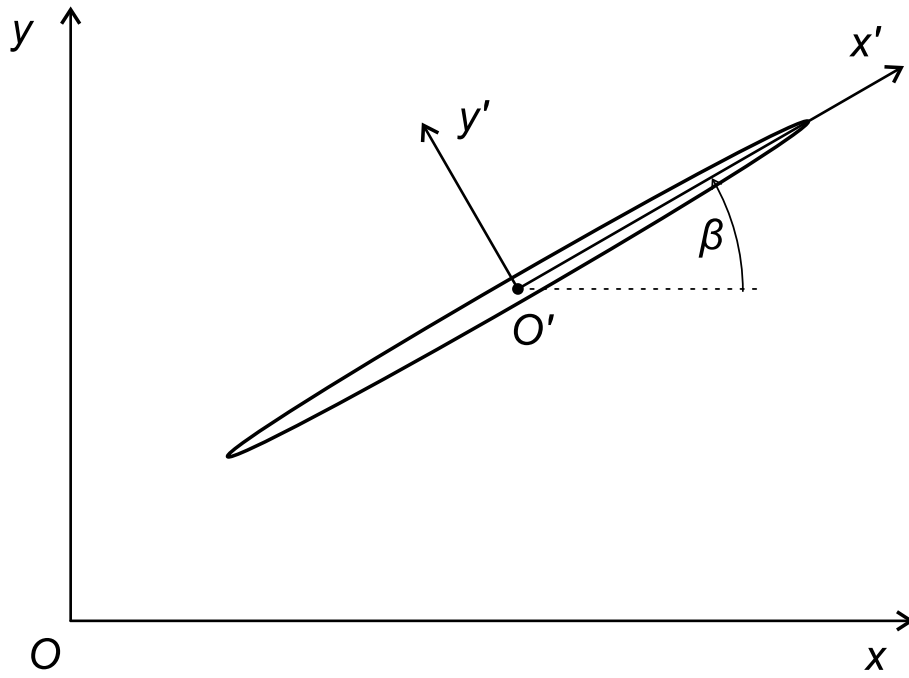
Figure 6.8: Illustration of the modeled flapping wing cross section with spatial O and body-fixed O' reference frames.
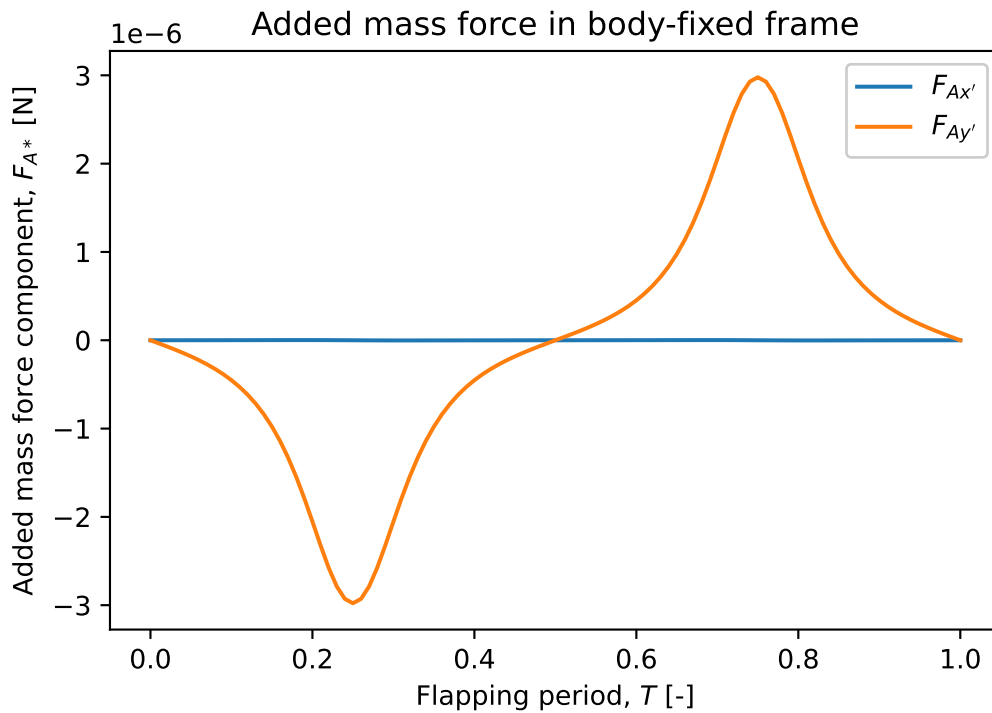

Figure 6.9: Evolution of added mass force components in the body-fixed reference frame (O' in Fig. 6.8) over one flapping cycle for a fruit fly-like aerial vehicle hovering.

As expected, symmetrical flapping pattern (shown in Fig. 6.2 and Fig. 6.3) produced symmetric added mass lift and drag components in Fig. 6.9, which cancel over whole
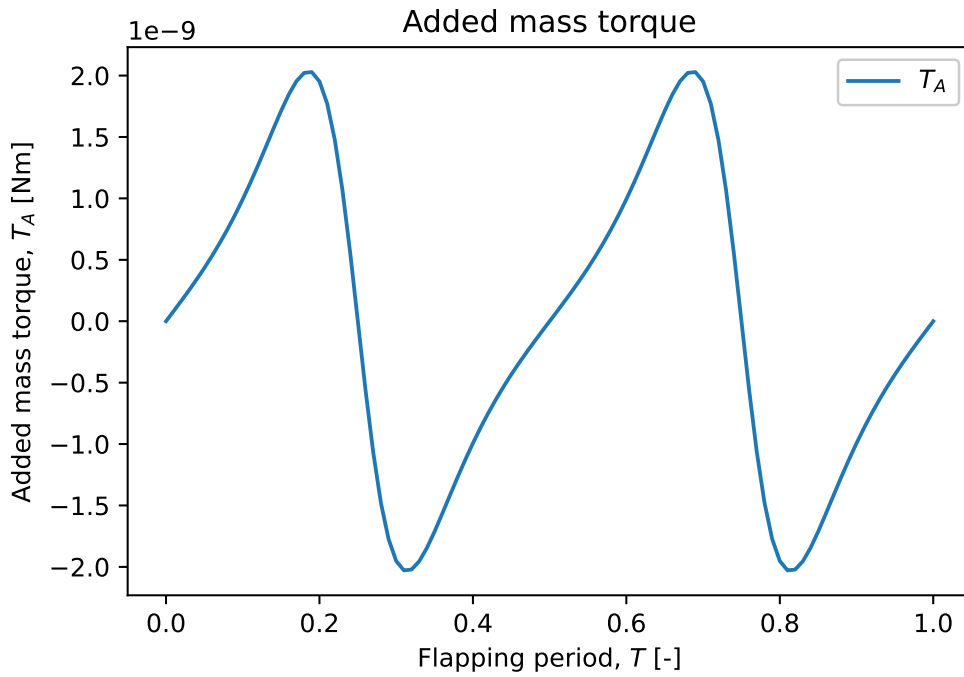
Figure 6.10: Evolution of added mass torque over one flapping cycle for a fruit fly-like aerial vehicle hovering.
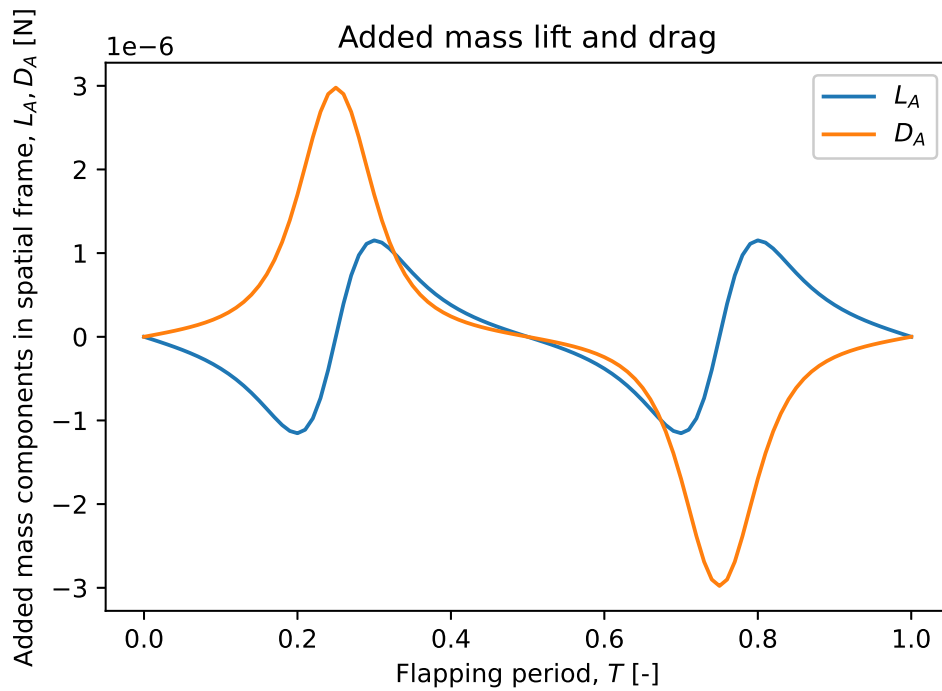

Figure 6.11: Added mass lift and drag force components over one flapping cycle for a fruit fly-like aerial vehicle hovering.

flapping cycle.

For the purpose of vorticity effects modeling airfoil is discretized with 10 vortex elements

(described in Chapter 5) of equal length. Kinematics of the flapping is, naturally, also same as introduced in subsection 6.1.2, while each flapping cycle is again discretized with 100 time steps. Vortex wake generation and evolution for these 100 time steps are illustrated in selected snapshots of wing and vortex wake, at different points in flapping period T, in Fig. 6.12.
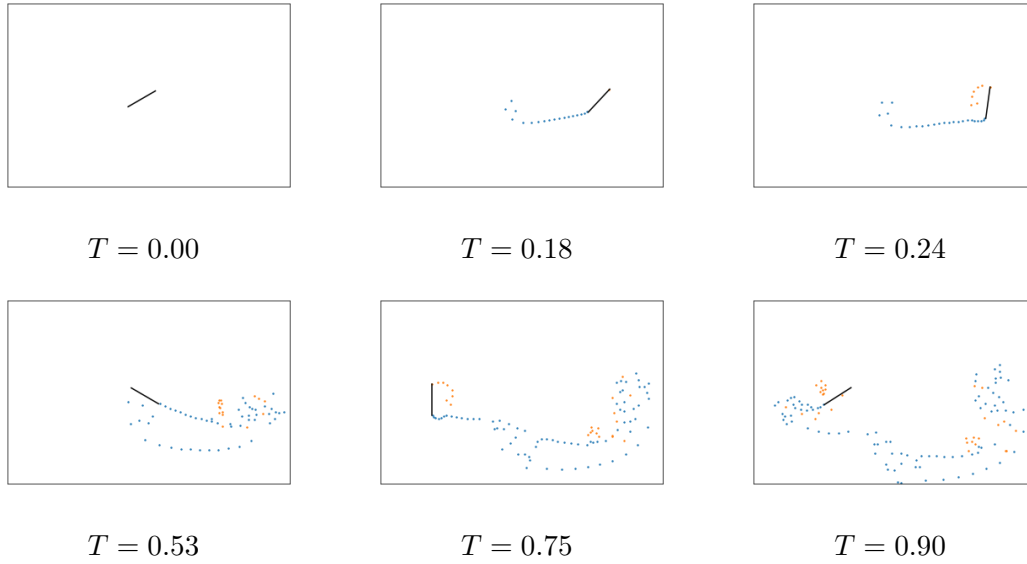

| $T = 0.00$ | $T = 0.18$ | $T = 0.24$ |

| $T = 0.53$ | $T = 0.75$ | $T = 0.90$ |

Figure 6.12: Snapshots of wing airfoil and vortex wake at different points in flapping period T. Blue points denote vortices that are shed from trailing edge, while orange points represent vortices shed from wing leading edge.

A vortex wake illustrated in Fig. 6.12 generates a circulation in airfoil-attached vortices, which can be used to calculate lift and drag force, due to the vorticity effects ($\boldsymbol{Q_{vort}}$ in (3.36)). Resulting lift and drag forces, due to vorticity effects, are presented in Fig. 6.13.

The overall computational procedure took approximately 40 ms for modeling of one flapping cycle, lasting $T = \frac{1}{f} = \frac{1}{167.3} \approx 6$ ms. However, it is important to note that the computational procedure could be further numerically improved and there are parts of the proposed algorithm that could be efficiently computed in parallel. Nevertheless, this is already multiple orders of magnitude computationally faster than conventional CFD algorithms, not applicable for use in simulation, control study and optimization [2]. Values of the total lift and drag force, calculated by the proposed computational model of insect type flapping wing aerial vehicle, can be obtained by summing added mass (Fig. 6.11) and vorticity effects (Fig. 6.13) lift and drag components, resulting with the force evolution presented in Fig. 6.14 and Fig. 6.15.
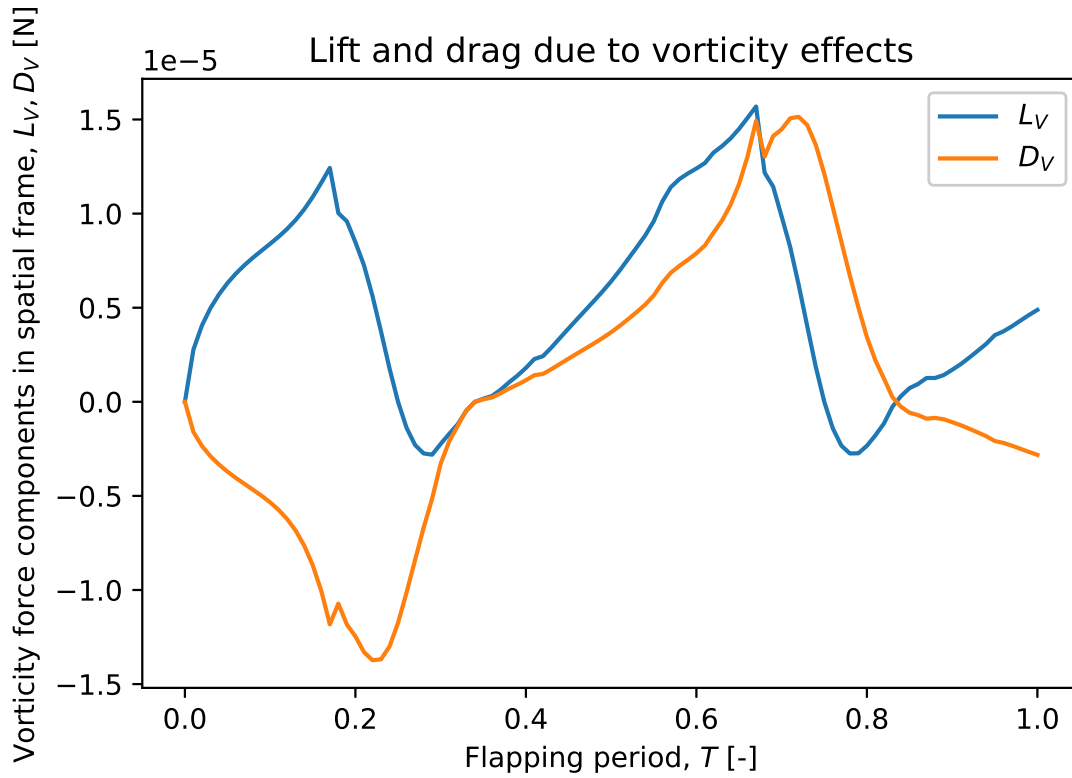
Figure 6.13: Lift and drag force due to vorticity wake effects over one flapping period for a fruit fly-like aerial vehicle hovering.
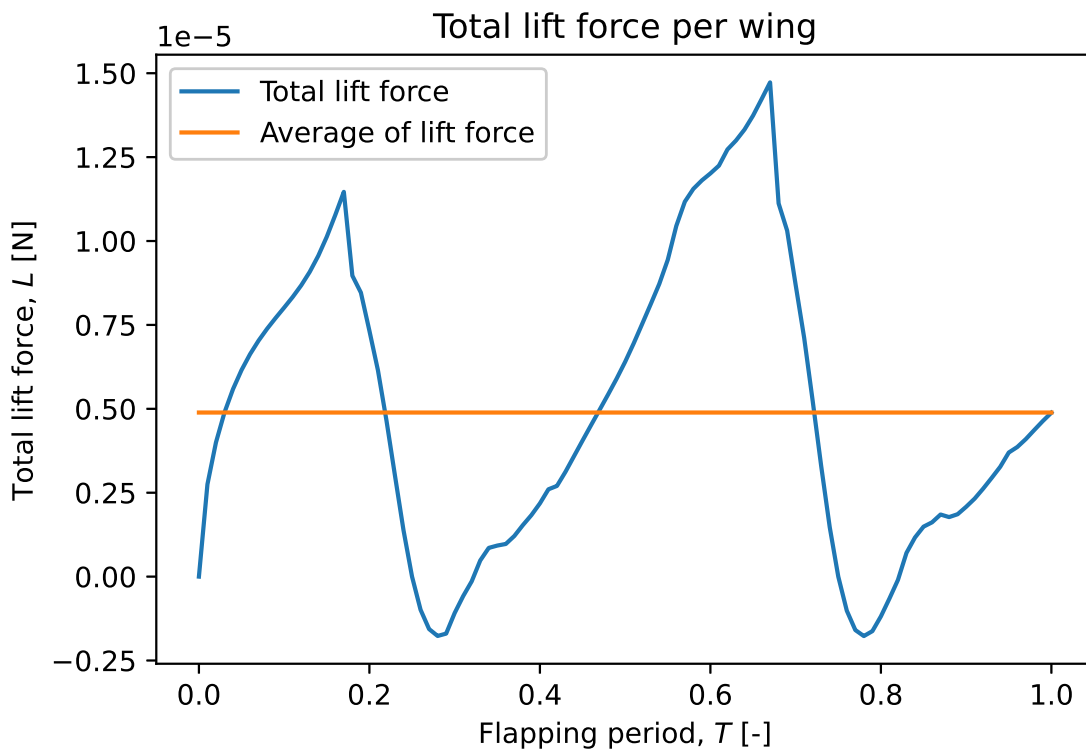

Figure 6.14: Total value of the lift force per one wing, calculated for fruit fly-like vehicle hovering with proposed computational model. Plot includes both total lift force evolution and cycle-averaged lift force value.
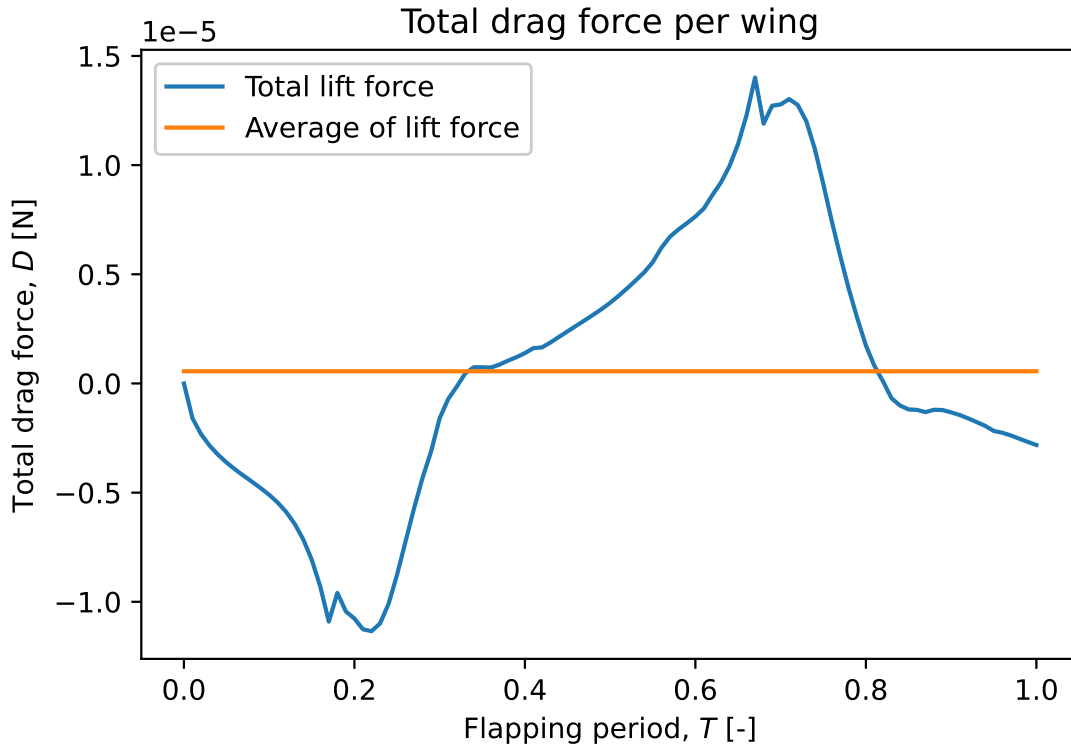
Figure 6.15: Total value of the drag force per one wing, calculated for fruit fly-like vehicle hovering with proposed computational model. Plot includes both total drag force evolution and cycle-averaged drag force value.

6.1.7 Results comparison and conclusions

With the aim of validating proposed flapping wing vehicle computational model, results of the computation (subsection 6.1.6) are compared to the results obtained with benchmarking method (subsection 6.1.5). Fig. 6.16 includes the comparison of lift force values over one flapping period, together with average values of lift force results. It is obvious that, although evolution of lift force over the flapping cycle is not same (probably due to the fact that the benchmarking quasi steady aerodynamic model neglects certain phenomena significant to the force evolution, see subsection 6.1.4), the average values of lift force match almost perfectly.

In the same manner as for lift, Fig. 6.17 includes the comparison of drag force values over one flapping period, together with average values of lift force results. It can again be noticed that the calculated drag force evolution over the flapping period is not same for both methods, average values are almost the same, validating a method in terms of cycle-averaged results.
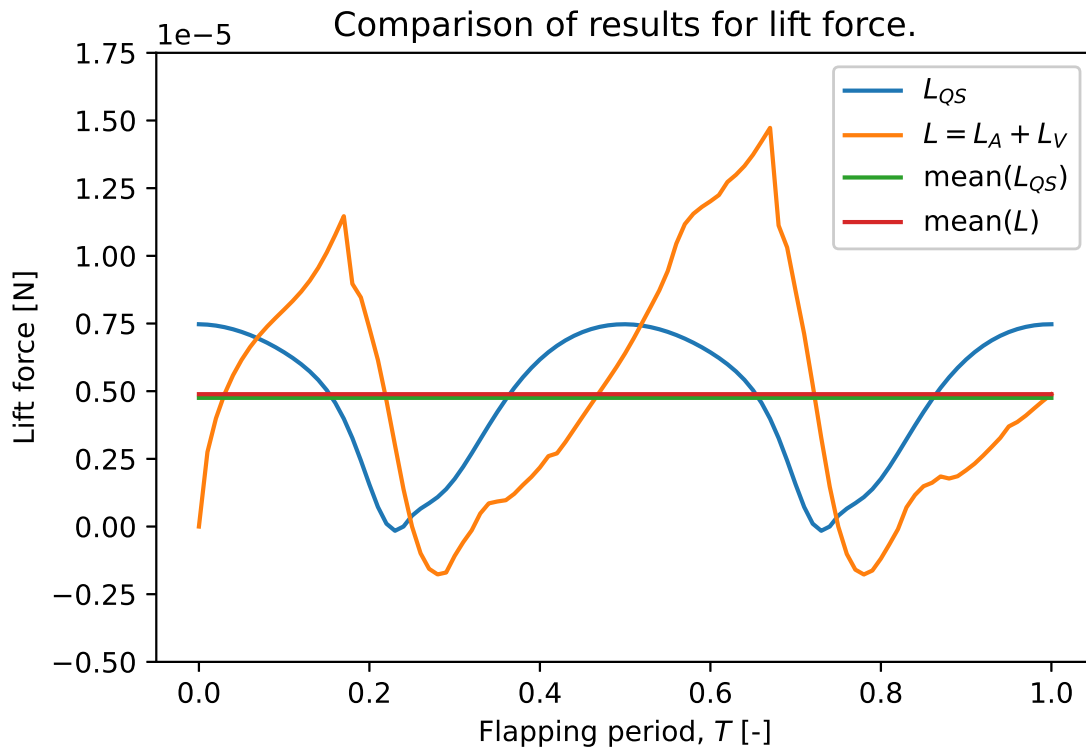
Figure 6.16: Comparison of lift force calculated by proposed approach to the lift force calculated by the benchmarking quasi steady aerodynamic model.
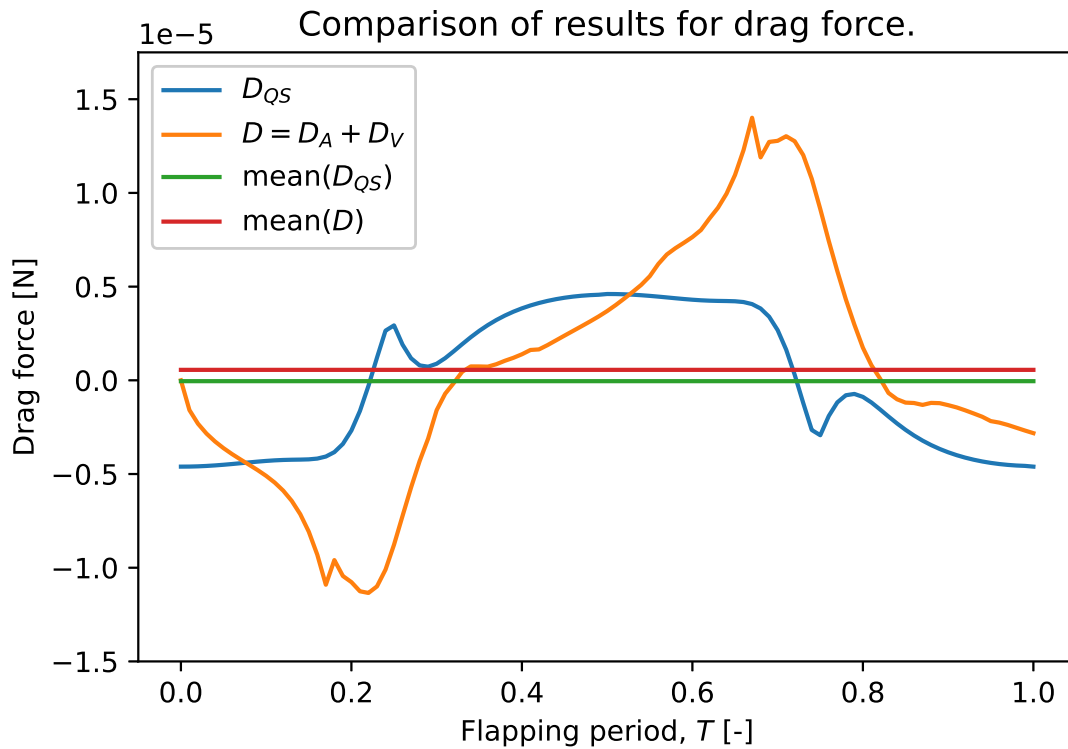

Figure 6.17: Comparison of drag force calculated by proposed approach to the drag force calculated by the benchmarking quasi steady aerodynamic model.

Since the average values of the quasi steady-based aerodynamic models are only reliable values, agreement of calculated cycle-averaged lift and drag forces (almost perfect agreement of lift force in Fig. 6.16 and very good agreement of drag force Fig. 6.17) indicates that the proposed computational model is validated for the numerical example of fruit fly like aerial vehicle hovering.

6.2 Flapping flight in Mars environmental conditions

Advances in the space travel have enabled researchers to not only observe space from a distance, but to also take samples and investigate space objects from vicinity. Recently, Mars has been high on the list of priorities for exploration. Geology of early Mars is well preserved, even for more than 3.5 billion years ago when approximately life on Earth began [83]. To this end, exploring Mars geological record could provide insights in time of life evolution and the possibilities of life starting somewhere else in the solar system.

Reaching Mars is not an insurmountable task anymore, with multiple space agencies demonstrating capabilities of reaching Mars. On the other hand, efficient exploration of Mars by gathering as much data possible imposes a challenge and is in the focus of recent developments. Mars exploration evolved through the stages of using flyby, orbiter, rover [84], and recently also NASA's "Ingenuity" rotorcraft unmanned aerial vehicle, making the first powered flight on another planet [85]. Usual state-of-the-art combination for Mars exploration consisted of rover and orbiter. However, the rover exploration limits due to the rugged and hazardous surface, together with the orbiter limits in image resolution and incapability of taking samples, indicate vertical takeoff and landing aerial vehicle as the natural extension of the "Mars exploration fleet", by providing faster movement, possibilities of reaching areas inaccessible by rovers and also provide greater field of view for steering rover.

Low Martian atmosphere density (about 1 % of atmosphere density on Earth's sea level) renders fixed-wing aircraft insensible because of large flying velocities required for sustaining lift. This indicated rotorcraft as the logical concept for first Mars flight, due to the current technological state-of-the-art, where completely novel flight concepts are not ready for such application. However, novel flight concepts with different type of propulsion are expected to replace rotorcraft in the future, due to the low efficiency of rotors in low Reynolds number conditions, experienced during Mars flight [86]. To this end, insect-type

flapping wings analyzed in the thesis, present themselves as the most promising future concept, because insects utilize this concept to fly efficiently in low Reynolds number regime on Earth for very long time. As an extreme example, alpine bumblebees are capable of flight at very low density (from Earth flight perspective) at an altitude of 9000 m [87]. To this end, this section includes the analysis of the fruit fly-like aerial vehicle flying in Mars environmental conditions.

6.2.1 Kinematics

The wing is modeled as having the same morphology as the fruit fly wing in previous section. However, due to the significantly lower values of atmosphere densities observed on Mars, the required wing is expected to be larger. Wing scaling is performed uniformly, i.e. all wing dimensions are multiplied by the same scaling factor n. Uniform scaling, preserving wing morphology, is required in order to keep using the same fruit fly-based quasi steady aerodynamic model for benchmarking purposes. Wing morphology and scaling is presented for scaling factor $n = 2$ in Fig. 6.18.
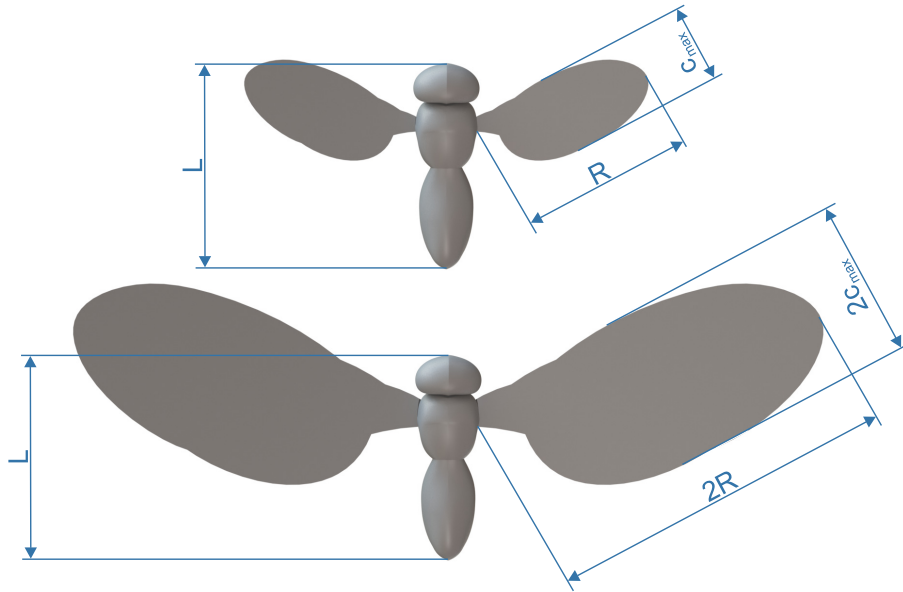

Figure 6.18: Illustration of the fruit fly with standard-sized wings and wings uniformly scaled by $n = 2$.

Wing shape (i.e. scaling factor) and flapping pattern are adopted from [26], where the optimal solution for fruit fly-like vehicle hovering is obtained. As in the previous section, fruit fly is modeled as a main body with two rigid wings attached. Optimal scaling factor is found to be $n = 4.2$, while the stroking and pitching angle functions, characterizing

flapping pattern, are presented in Fig. 6.19 and Fig. 6.20, respectively. The flapping frequency for hovering in Martian environment with these flapping angle functions is equal to $f = 50.9$ Hz.
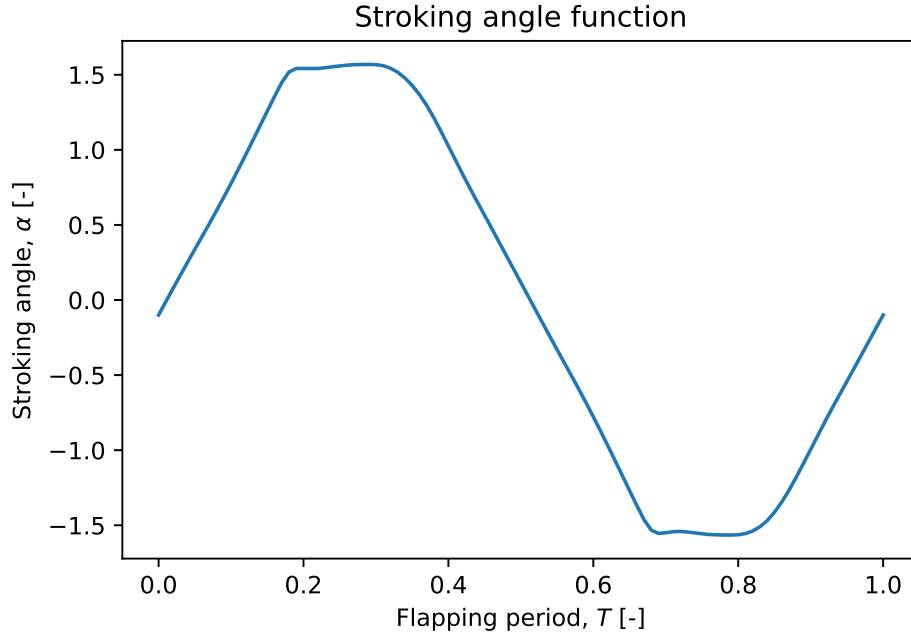

Figure 6.19: Evolution of stroking angle function $\alpha(t)$ over one flapping period for standstill hovering in Mars environmental conditions.
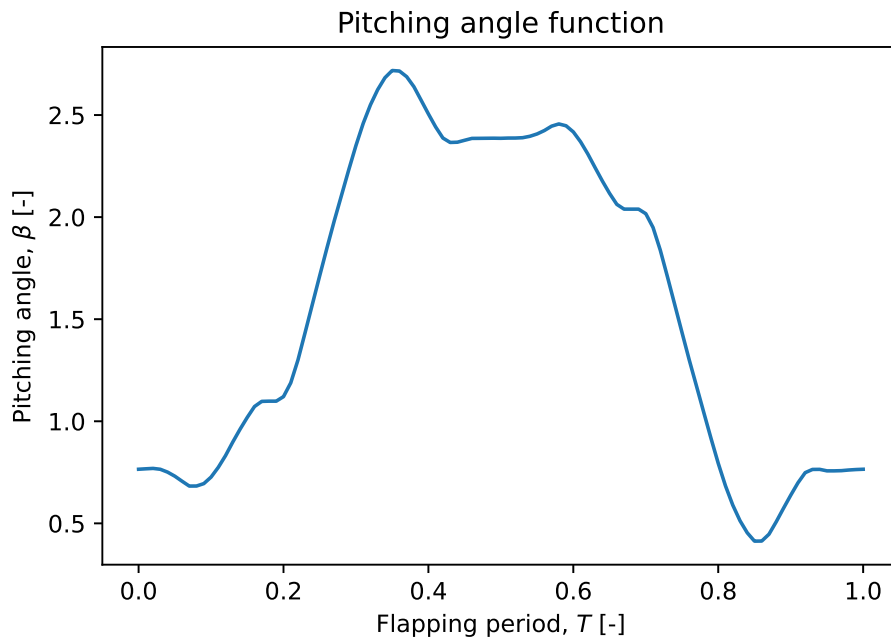

Figure 6.20: Evolution of pitching angle function $\beta(t)$ over one flapping period for standstill hovering in Mars environmental conditions.

Table 6.3
Properties of the fruit fly and Martian atmosphere

Description	Label	Value	Source
Gravitational acceleration $\left[\frac{m}{s^2}\right]$	g_{Mars}	3.72	[88]
Atmospheric density $\left[\frac{kg}{m^3}\right]$	ρ_{Mars}	$1.55 \cdot 10^{-2}$	[88]
Dynamic viscosity $\left[\frac{kg}{ms}\right]$	μ_{Mars}	$1.5 \cdot 10^{-5}$	[88]
Wing length $[m]$	R	$2.5 \cdot 10^{-3} \cdot n$	[72]
Mean chord length $[m]$	$\bar{c}$	$6.68 \cdot 10^{-4} \cdot n$	[72]
Wing thickness $[m]$	b	$2.3 \cdot 10^{-5} \cdot n$	[72]
Wing surface $[m^2]$	S	$0.0167 \cdot 10^{-4} \cdot n^2$	[72]
Body mass $[kg]$	m_b	$0.96 \cdot 10^{-6}$	[70]
Wing mass $[kg]$	m_w	$2.4 \cdot 10^{-9} \cdot n^3$	[71]
Wing inertia matrix $[kg \cdot m^2]$	I_w	$\begin{bmatrix} 2.889 & -8.368 & 0 \\ -8.368 & 48.255 & 0 \\ 0 & 0 & 51.144 \end{bmatrix} \cdot 10^{-16} n^5$	-
Rotational force coefficient	C_R	1.55	[27]

6.2.2 Physical properties

The wing is assumed to be homogeneous, with density calculated from the fruit fly wing mass (already reported in Table 6.3). The properties of a an enlarged flapping wing for Mars environment can now be obtained by scaling the values pertinent to initial wing. Properties of the scaled wing, depending on the scaling factor n, are presented in Table 6.3, together with the sources for obtained data. Only value without source is wing inertia matrix, calculated from CAD model of fruit fly wings with the assumption of uniform density.

As already mentioned, Martian atmosphere density is significantly (almost 100 times) lower than Earth's atmosphere density. However, beneficial for flight performance, gravity is also lower than Earth's (almost three times). These values, together with dynamic viscosity of Martian atmosphere, and sources for all values are given in Table 6.3.

6.2.3 Quasi steady aerodynamic model used for benchmarking

Same quasi steady model introduced in subsection 6.1.4 is again here utilized as a benchmarking method. Although model parameters are fitted and model validated based on experiments conducted on Earth, the application of the model in this case is appropriate in these circumstances. In order to justify this claim it should be noted again that the experiments were performed on a dynamically scaled model of fruit fly-like

wings, by keeping the values of Reynolds number preserved. This has been achieved by utilizing enlarged wings submerged in oil [69]. Thus created model has proven to be reliable for aerodynamic force prediction of both the real life fruit fly wings and the experimental enlarged fruit fly-like wing submerged in oil, as long as Reynolds number value is preserved. Therefore, it can be concluded that the described quasi steady model can be used as a reliable method for aerodynamic load prediction on fruit fly-like wings in Martian atmosphere as long as the Reynolds number is kept in the validated range.

Reynolds number in the case of a insect-type flapping wing vehicles is often given as

$$\mathrm{Re} = \frac{\rho v_{ref} L_{ref}}{\mu}, \tag{6.9}$$

where ρ stands for atmosphere density, v_{ref} represents reference velocity (here taken to be mean wing tip velocity [83]), L_{ref} is the reference length (here equal to the mean chord length $\bar{c}$), while μ represents the value of dynamic viscosity. A range of appropriate values of Reynolds number for this model is taken to be from 100 to 1400, as indicated in [76].

6.2.4 Benchmark results

Quasi steady-based aerodynamic model presented in subsections 6.1.4 and 6.2.3 is applied on the fruit fly-like vehicle flapping with kinematics as introduced in subsection 6.2.1 (flapping angle functions depicted in Fig. 6.19 and Fig. 6.20) to obtain benchmark results for validation of the proposed method in the Mars environment. Evolution of the lift and drag force components over one flapping period for described case are presented in Fig. 6.21 and Fig. 6.22 for all three aerodynamic phenomena (described in subsection 6.1.3) captured by quasi steady aerodynamic model. Plots of the overall lift and drag force evolution over one flapping period are given in Fig. 6.23 and Fig. 6.24, respectively, together with designation of the average lift and drag force values.
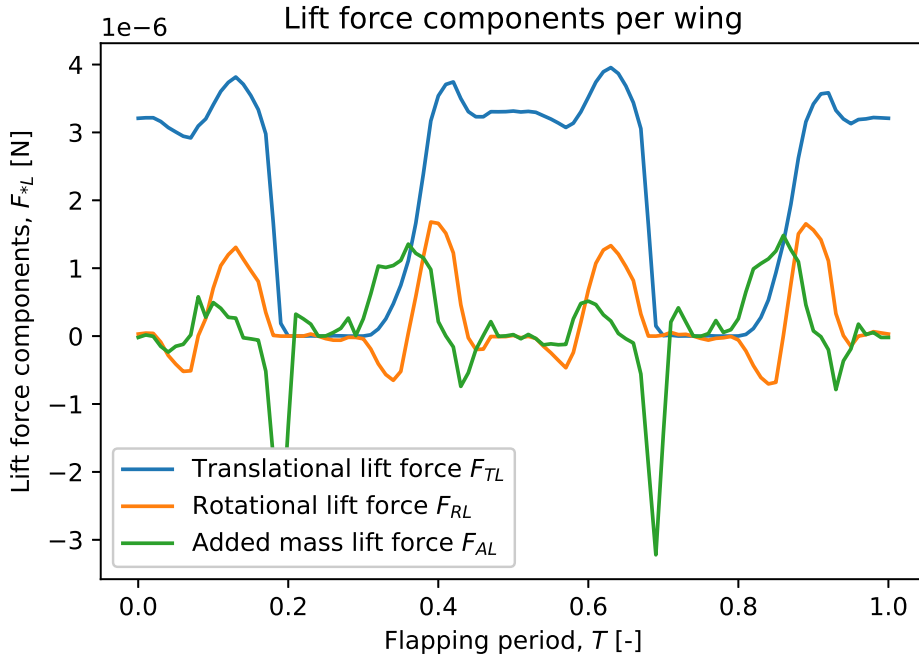
Figure 6.21: Lift force components over one flapping cycle, calculated by quasi steady aerodynamic model for fruit fly like aerial vehicle in Martian atmosphere, flapping with angle functions presented in Fig. 6.19 and Fig. 6.20. Force components values correspond to one wing, while the forces are equal on each wing, due to the symmetrical flapping.

Figure 6.22: Drag force components over one flapping cycle, calculated by quasi steady aerodynamic model for fruit fly like aerial vehicle in Martian atmosphere flapping with angle functions presented in Fig. 6.19 and Fig. 6.20. Force components values correspond to one wing, while the forces are equal on each wing, due to the symmetrical flapping.
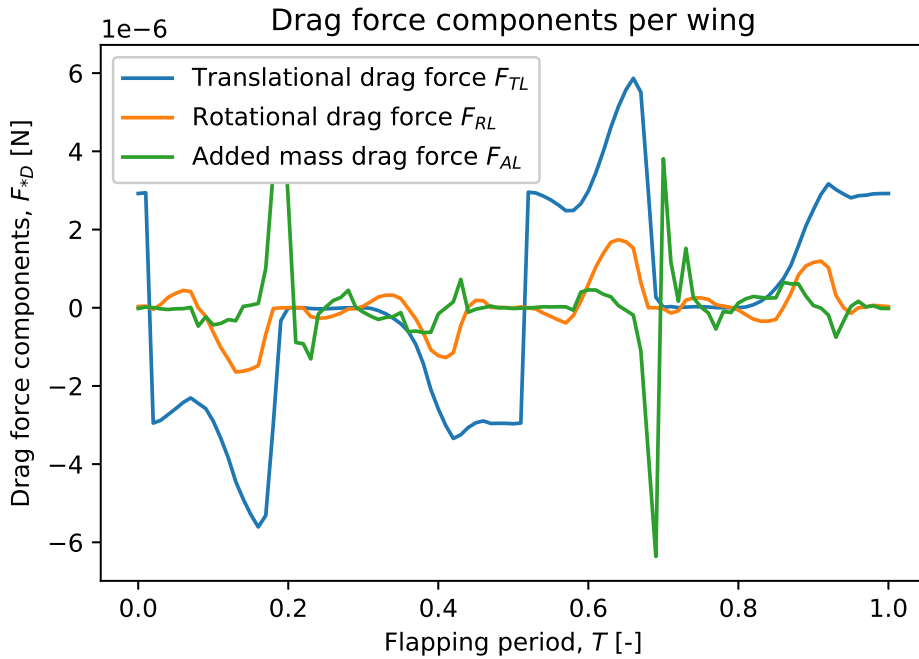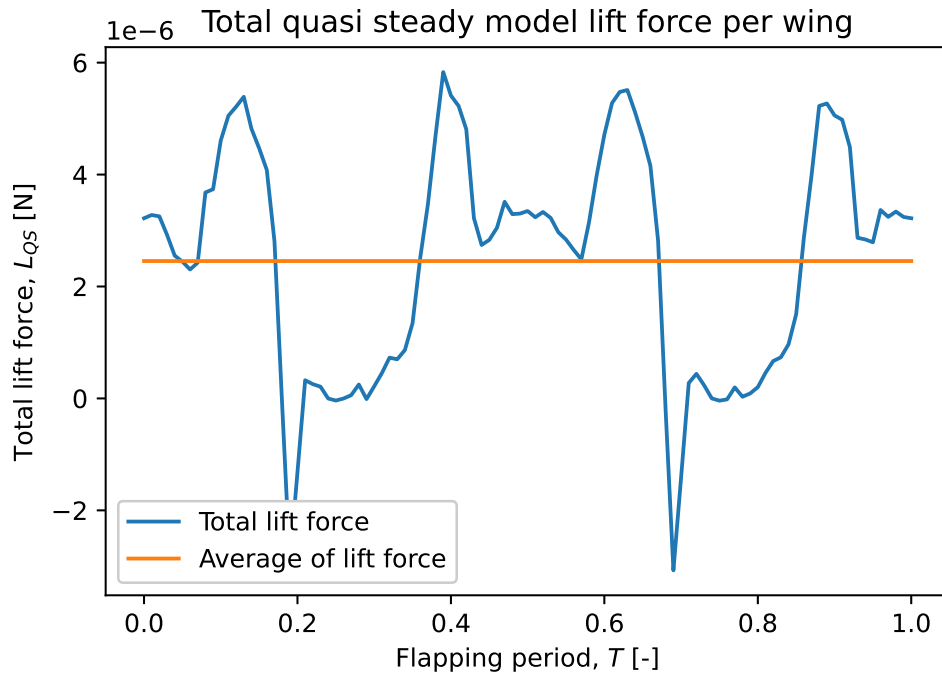
Figure 6.23: Total value of lift force per one wing, calculated for fruit fly-like vehicle hovering on Mars with quasi steady aerodynamic model. Plot includes both total lift force evolution and cycle-averaged lift force value.
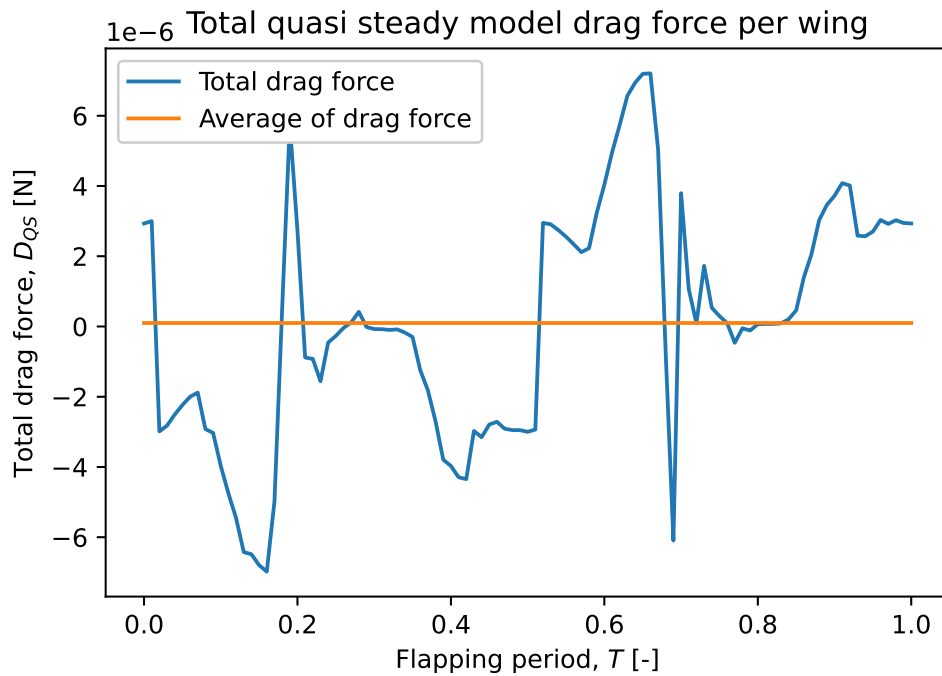

Figure 6.24: Total value of drag force per one wing, calculated for fruit fly-like vehicle hovering on Mars with quasi steady aerodynamic model. Plot includes both total drag force evolution and cycle-averaged drag force value.

6.2.5 Results of the analysis with proposed computational model

As introduced and already applied in subsection 6.1.6, proposed computational model of an insect type flapping wing aerial vehicle consists of two distinct procedures for modeling effects of added inertia (Chapter 4) and vortex wake (Chapter 5), performed in conjunction to model aerodynamics of insect type flapping wing aerial vehicles.

For the purpose of added inertia effects modeling, cross section of the wing is again set to be ellipse, due to the unavailability of better fruit fly wing cross section data. The ellipse semi-major axis is equal to half the chord $\frac{c}{2}$ at the radial position r along the wing, while the semi-minor axis corresponds to the assumed constant wing thickness (table 6.3). Boundary discretization and coordinate systems are equivalent to previous numerical example (subsection 6.1.6).

Kinematics of the flapping is introduced in subsection 6.2.1, while each flapping cycle is again discretized with 100 time steps. Summing the effects of $\boldsymbol{M_F\dot{v}}$ and $\boldsymbol{Q_{AM}}$ in (3.36) results in the overall aerodynamic load due to the added inertia of the surrounding fluid. Resulting force components and torque, all expressed in the body-fixed reference frame (illustrated in Fig. 6.8 as O'), are shown in Fig. 6.25 and Fig. 6.26.
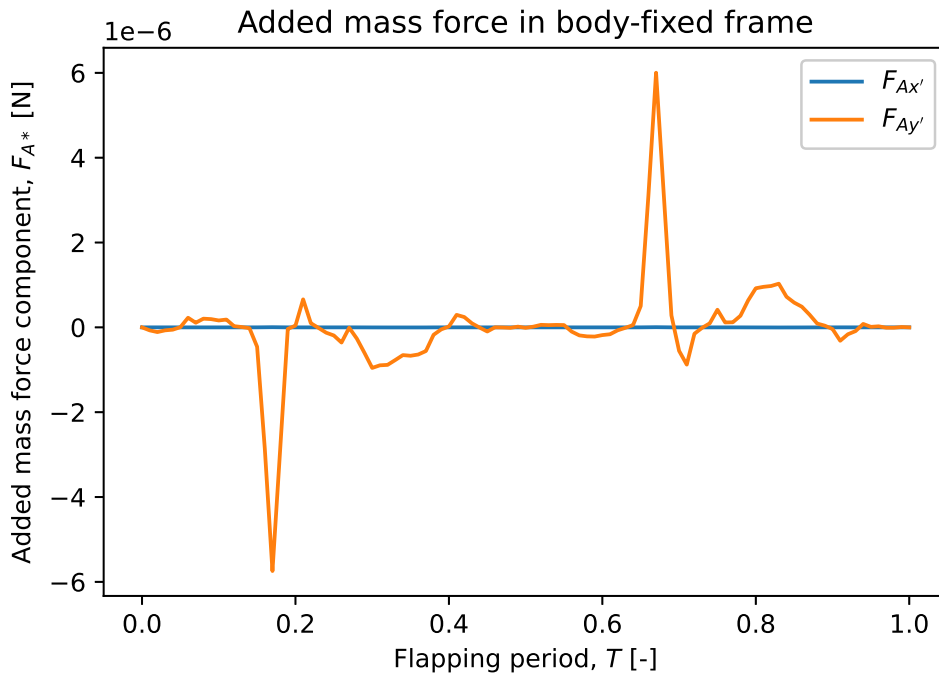

Figure 6.25: Evolution of added mass force components in the body-fixed reference frame (O' in Fig. 6.8) over one flapping cycle in Martian atmosphere.
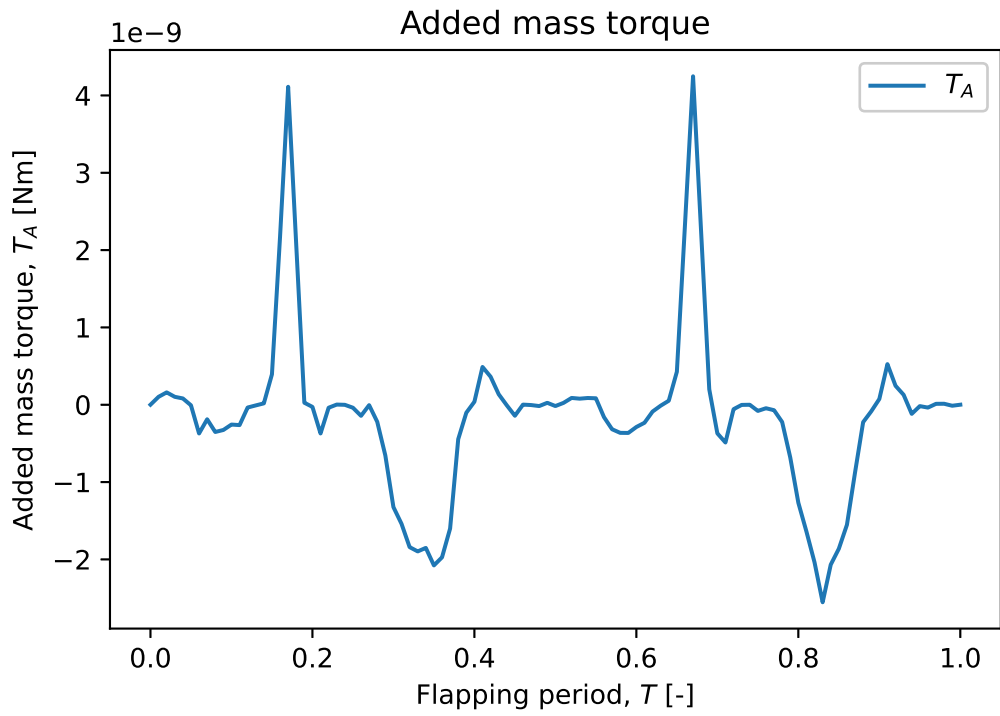
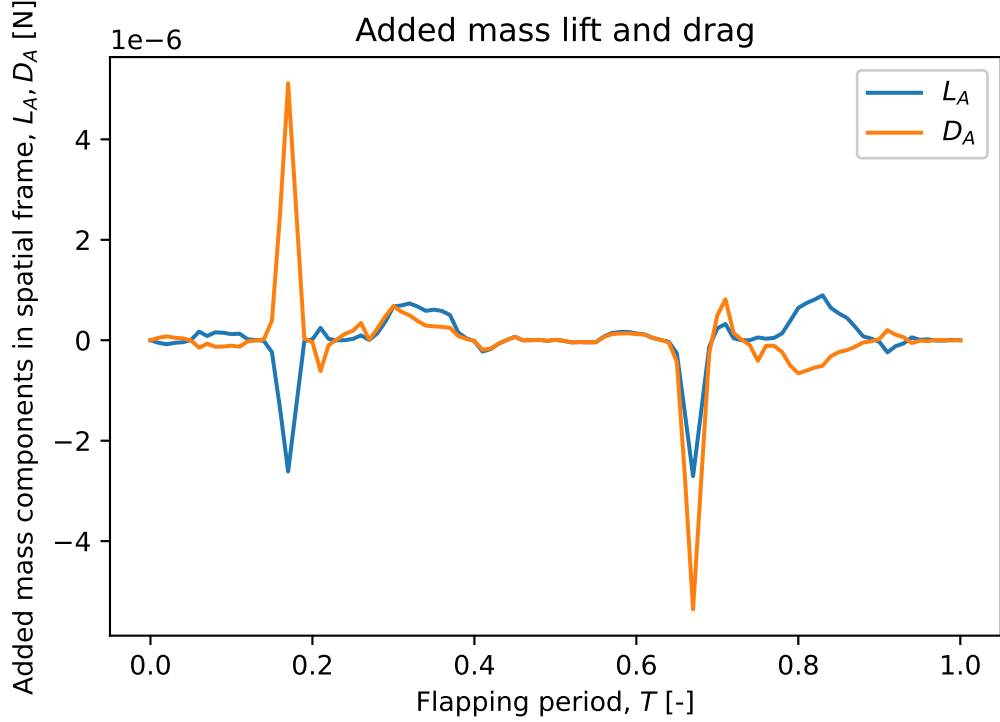**Figure 6.26:** Evolution of added mass torque over one flapping cycle in Martian atmosphere.

Figure 6.27: Added mass lift and drag force components over one flapping cycle in Martian atmosphere.

Similarly as before, added mass in x' direction (presented in Fig. 6.25) is not zero, but approximately three orders of magnitude smaller than the added mass y' components, due to the high ellipse eccentricity (large ratio between semi-major and semi-minor axis). After taking into account the orientation of the flapping wing in each time step, the lift and drag added mass components (added mass forces in x and y direction on Fig. 6.8), can be calculated resulting in plot shown in Fig. 6.27.

Opposed to the symmetrical flapping pattern in previous numerical example (section 6.1), a non-symmetrical flapping pattern found to be optimal for standstill hovering on Mars [26] utilized here produces non-symmetric added inertia lift and drag components (Fig 6.27).

Regarding vorticity effects modeling, despite the fact that the wings have been enlarged by factor $n = 4.2$, airfoil discretization with 10 vortex elements (described in Chapter 5) of equal length was again enough for results convergence. Flapping kinematics introduced in subsection 6.2.1 is again discretized with 100 time steps. Vortex wake generation and evolution for these 100 time steps in Martian atmosphere are illustrated in selected snapshots of wing and vortex wake, at different points in flapping period T, in Fig. 6.28.

| $T = 0.00$ | $T = 0.18$ | $T = 0.24$ |

| $T = 0.53$ | $T = 0.65$ | $T = 0.98$ |
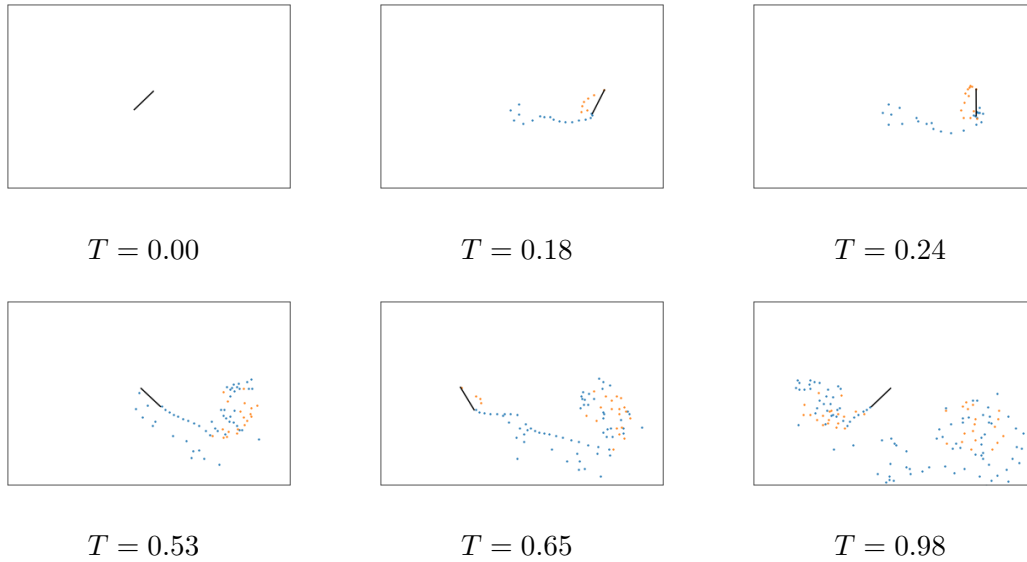
Figure 6.28: Snapshots of wing airfoil and vortex wake at different points in flapping period T, for standstill hovering on Mars. Blue points denote vortices that are shed from trailing edge, while orange points represents vortices shed from wing leading edge.

A vortex wake illustrated in Fig. 6.28 generates a circulation in airfoil-attached vortices, which can be used to calculate lift and drag force, due to the vorticity effects ($\boldsymbol{Q_{vort}}$ in (3.36)). Resulting lift and drag forces, due to vorticity effects in Martial atmosphere, are

presented in Fig. 6.29.
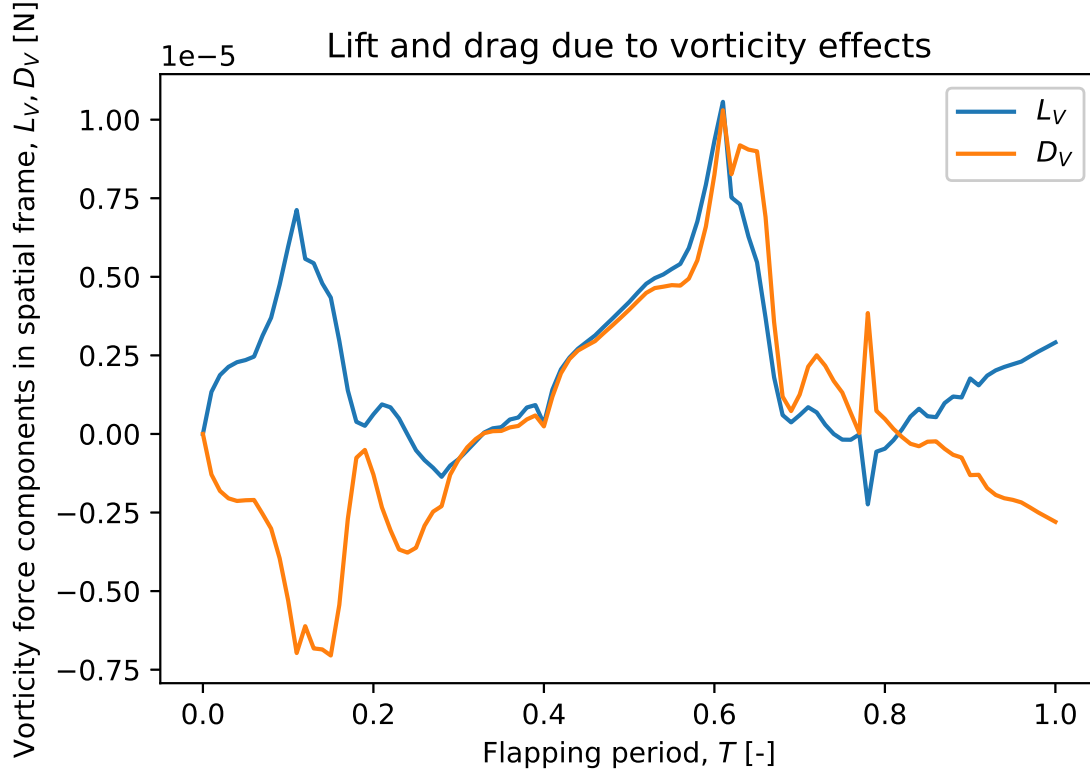
Figure 6.29: Lift and drag force due to vorticity wake effects in Martian atmosphere over one flapping period.

The overall computational procedure again (since the same number of boundary elements and time steps are employed) took approximately 40 ms for modeling of one flapping cycle, now lasting $T = \frac{1}{f} = \frac{1}{50.9} \approx 20$ ms, which is very close to the real time behavior. Values of the total lift and drag force, calculated by the proposed computational model of insect type flapping wing aerial vehicle, can be obtained by summing added mass (Fig. 6.27) and vorticity effects (Fig. 6.29) lift and drag components, resulting with the overall force components evolution presented in Fig. 6.30 and Fig. 6.31.

Figure 6.30: Total value of the lift force per one wing, calculated for fruit fly like vehicle hovering on Mars with proposed computational model. Plot includes both total lift force evolution and cycle-averaged lift force value.
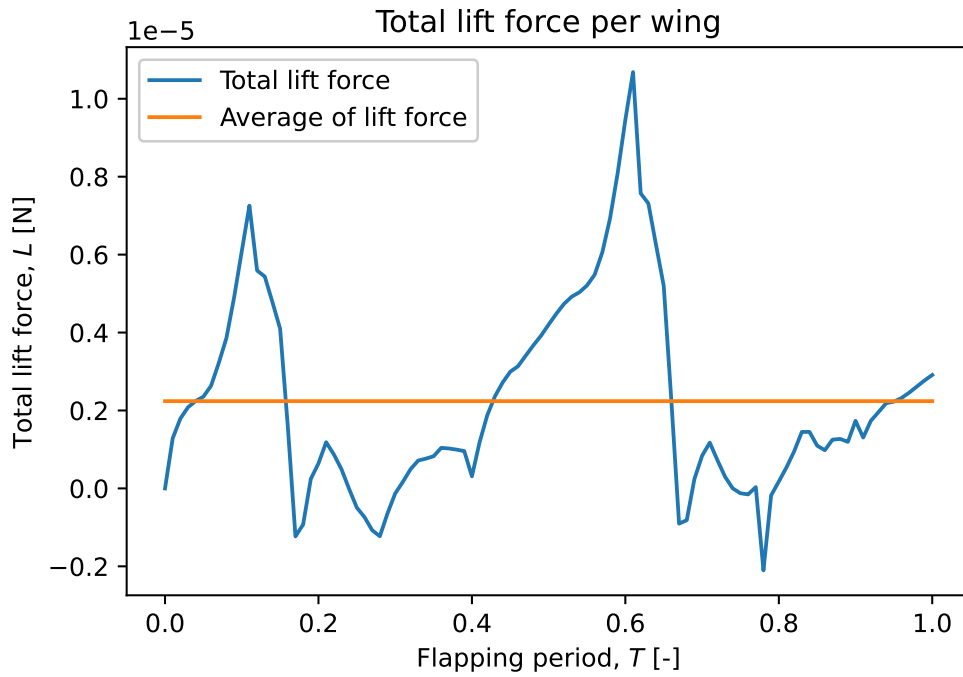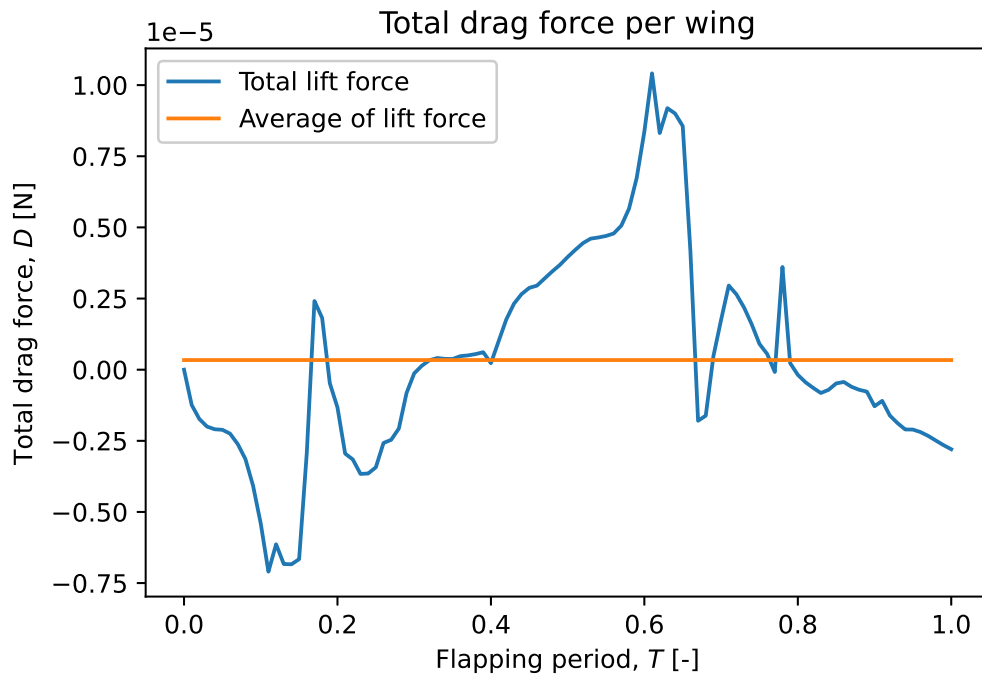

Figure 6.31: Total value of the drag force per one wing, calculated for fruit fly like vehicle hovering on Mars with proposed computational model. Plot includes both total drag force evolution and cycle-averaged drag force value.

6.2.6 Results comparison and conclusions

In the previous example (section 6.1), proposed approach has been validated for the fruit fly hovering on Earth, which included relatively smooth flapping angle functions. Here, on the other hand, standstill hovering of fruit fly-like aerial vehicle (same wing morphology but different size) in Martian environment has been considered. This also included non-smooth flapping angle functions (Fig. 6.19 and Fig. 6.20), obtained in discrete form from the optimization presented in [26]. To validate proposed flapping wing vehicle computational model in this environment, results of the computation (subsection 6.2.5) are compared to the results obtained with benchmarking method (subsection 6.2.4). Fig. 6.32 includes the comparison of lift force values over one flapping period in Martian atmosphere, together with average values of lift force results. It is obvious that, although evolution of lift force over the flapping cycle is not same (again probably due to the fact that the benchmarking quasi steady aerodynamic model neglects certain phenomena significant to the force evolution, see subsection 6.1.4), the average values of lift force match almost perfectly.
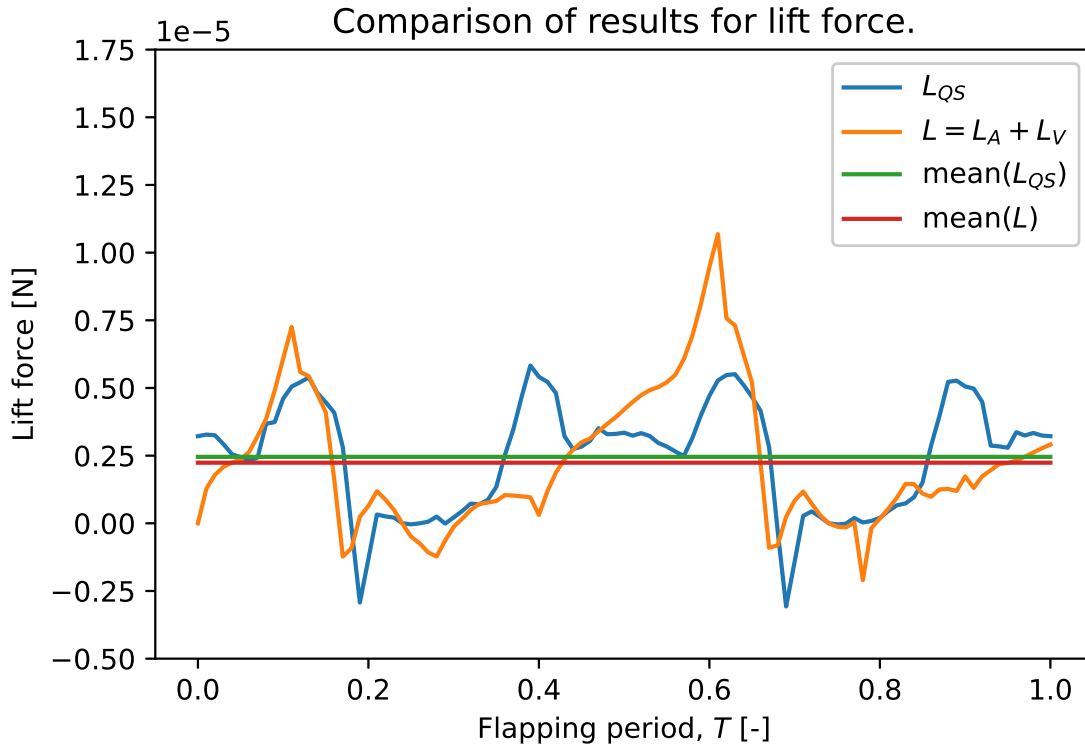

Figure 6.32: Comparison of lift force on flapping wing in Martian atmosphere, calculated by proposed approach to the lift force calculated by the benchmarking quasi steady aerodynamic model.

In the same manner as for lift, Fig. 6.33 includes the comparison of drag force values over one flapping period in Martian atmosphere, together with average values of lift force results. It can again be noticed that, although the calculated drag force evolution over flapping period is not same for both methods, average values match almost perfectly, validating a method in terms of cycle-averaged results.
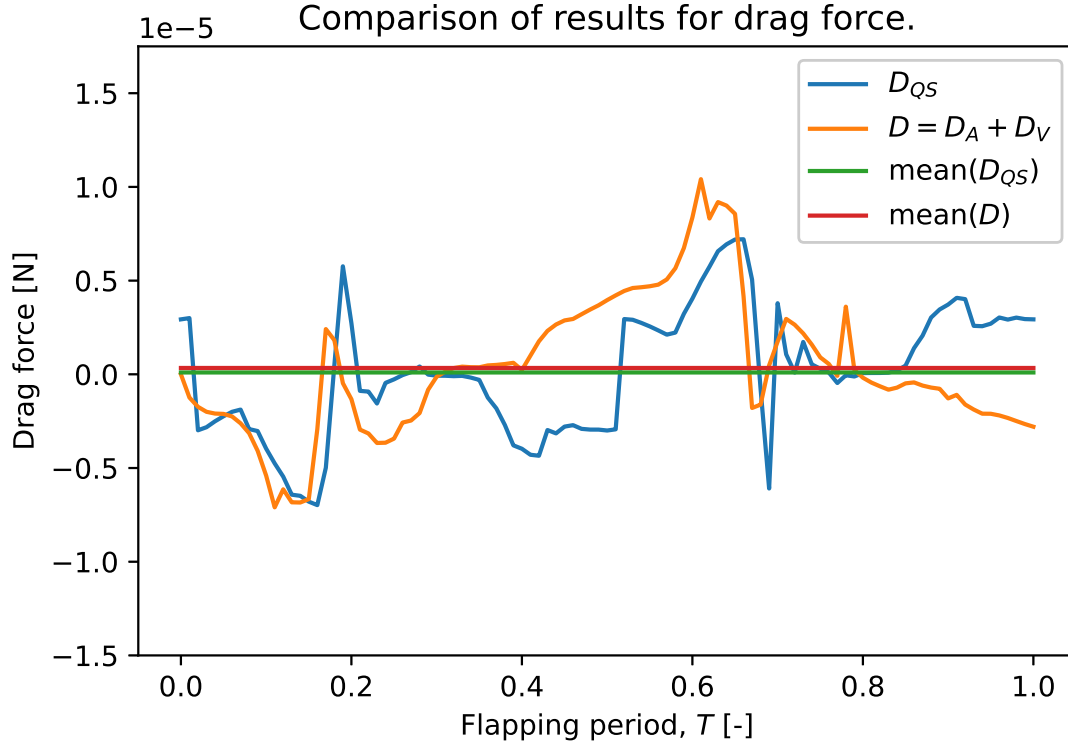
Figure 6.33: Comparison of drag force on flapping wing in Martian atmosphere, calculated by proposed approach to the drag force calculated by the benchmarking quasi steady aerodynamic model.

Since the average values of the quasi steady-based aerodynamic models are only reliable values, agreement of calculated cycle-averaged lift and drag forces (almost perfect agreement of lift force in Fig. 6.32 and drag force Fig. 6.33) indicates that the proposed computational model is validated for the numerical example of fruit fly like aerial vehicle hovering. In addition to this, it is important to again emphasize that due to the high values of flapping frequencies exact evolution of the aerodynamic force over the flapping cycle has negligible influence on the overall accuracy [73], therefore not being in the focus of most insect-type flapping aerodynamics computational models.

CHAPTER 7

Conclusion

Thesis has been focused on development of mid-fidelity computational model for insect-type flapping wing aerial vehicle, capable of reliable aerodynamic load modeling, while being efficient enough to be used within design optimization and optimal control loops. The computational model is founded on the findings that, due to the high flapping frequencies (and consequently high values of Strouhal number) boundary layer modeling can be neglected, despite the low Reynolds number characterizing flow around insect-type flapping wings. This allows the fluid viscosity effects on flapping wings to be modeled by vortex wake.

Helmohltz-Hodge decomposition is utilized to decompose fluid velocity vector field into curl-free and divergence-free parts. Curl-free part of the fluid velocity is then used to model added inertia effects of the fluid, important in the context of insect-type flapping due to the high wing accelerations and complex wing kinematics. On the other hand, divergence-free part is utilized for viscosity effects modeling, based on the vortex wake.

Equations of motion for the flapping wing aerial vehicle, as a coupled multibody-fluid system, are derived in DAE index 1 form. Effects of the curl-free part of fluid velocity vector field (added inertia effects) are modeled in terms of multibody system variables only, after performing symplectic reduction, exploiting "particle relabeling symmetry" property, to reduce out fluid variables. The time-dependent nature of the added inertia matrix is taken into account in deriving equations, leading to the additional "aerodynamic load" term. On the other hand, effects of the divergence-free fluid velocity component arise in the coupled system equations of motion as an external load to the multibody system.

Calculation of added inertia effects is formulated as an Exterior Laplace boundary value problem, with non-penetrability constraints on surfaces. This is done after decomposing the respective part of fluid velocity potential in six (or three in 2D) components for each

rigid body. Resulting boundary value problem is solved by in-house developed collocation boundary element method with analytic solutions for singular integrals, and validated on geometric shapes with analytic added inertia solutions.

Viscosity effects modeling is approached with vortex wake modeling algorithm, based on lumped vortex element method with irrotational point vortices. However, the method is tailored for use in insect-type flapping wing aerodynamics modeling by introducing leading edge vortex shedding, if certain thresholds are satisfied. Aerodynamic load on the aerial vehicle, due to the resulting irrotational point vortex wake, is calculated from kinematics and vortex elements circulation by using Kutta-Joukowski theorem.

The overall insect-type flapping wing computational model is tested on two numerical examples. Both examples are based on fruit fly morphology, due to availability of benchmarking quasi steady aerodynamic models with validated parameters for the flow characterized by certain range of non-dimensional numbers. First example involves fruit fly standstill hovering with smooth flapping angle functions, found in literature. Second example involves fruit fly-like aerial vehicle with uniformly enlarged flapping wing, analyzed for hovering in Mars atmospheric environment. Both numerical examples demonstrated near real time properties of the computational model with high accuracy of load prediction.

Main thesis conclusions can be summarized as:

- Insect-type flapping wing aerodynamics can be accurately and efficiently modeled by computational model based on decomposition of the fluid velocity vector field into curl-free part, modeling added inertia effects, and divergence-free part, describing viscosity effects in terms of irrotational point vortex wake. As previously suggested in literature, it is confirmed that neglecting boundary layer effects does not lead to significant loss in accuracy.

- Proposed computational model has a near real-time computation properties with reliable insect-type flapping wing aerodynamic load prediction, while requiring no parameter fitting based on previous experience or results, as opposed to the often used numerically efficient quasi steady aerodynamic model. This makes the model suitable for use in design optimization and optimal control loops.

- Correct derivation of equations of motions for a coupled multibody-fluid system leads to the additional term in the "aerodynamic load" components due to the

time-dependent nature of the added inertia matrix, opposed to the standard rigid body inertia matrix. This term is often mistakenly overlooked and not included in analysis.

- Added inertia effects, including influence of the coupling between rigid bodies in multibody chain, exact body geometries and time-dependence can be accurately modeled by formulating problem as a set of exterior Laplace boundary value problems. Collocation boundary element method is validated for solving the resulting set of boundary value equations on the simple geometric shapes, for which analytic solution exists.

- Insect-type flapping flight viscosity effects can be reliably and efficiently calculated by proposed irrotational point vortex wake model, based on the conventional unsteady lumped vortex element method, tailored for insect-type flapping flight by adding leading edge vortex shedding and evolution.

- Numerical experiments in the significantly different Earth and Mars atmosphere suggest that the proposed method can be used for flapping flight modeling in unknown environments, without any change in parameters.

7.1 Main scientific contributions and hypothesis confirmation

Main scientific contribution of the research is a novel computational model of an insect-type flapping wing aerial vehicle, based on geometric reductions of the coupled multibody-fluid system on manifolds and Lie groups, supplemented with mechanism for describing significant viscous effects in the form of vortex wake modeling. The computational model enables accurate and reliable calculation of flapping wing aerial vehicle performance, while still being numerically efficient enough to be used in design optimization and optimal control loop. To this end, main scientific contributions can be summarized as:

- Development of a novel computational model for insect-type flapping wing aerial vehicle, capable of reliable and efficient modeling of most important complex aerodynamic phenomena pertinent to insect-type flapping flight physics. Computational model is based on Hamiltonian geometric reductions on fluid-solid coupled system

manifold (Lie group), supplemented with numerical model for describing important viscous effects of flapping wings in ambiental fluid.

- Development and numerical implementation of the model for calculating added inertia effects of insect-type flapping wings submerged in ambiental fluid, based on symplectic reduction of the coupled system and numerical boundary element method.

- Tailoring of the conventional unsteady lumped vortex element method for insect type flapping wing utilization, by developing and implementing numerical model for leading and trailing edge vortex shedding and evolution.

- Synthesis of numerically efficient computational environment which can be used for multiphysical optimization of insect-type flapping wing aerial vehicle in different atmospheric environments, such as in physical environment pertinent to Earth flight, but also in the especially challenging flight conditions pertinent to Martian atmosphere.

Developed computational model properties confirm the hypothesis introduced in section 1.3.

7.2 Outlook and future work

There is no question that the research of the insect-type flapping will continue with the aim of both understanding all the intricate aerodynamic phenomena that insect utilize to achieve great performance capabilities, and also with the aim of manufacturing aerial vehicle utilizing as much of these phenomena as possible. Further development of the computational models for insect-type flapping wings is of great importance for achieving such goals. To this end, for different goals and different research phases, computational models with various levels of accuracy will have its use, from quasi steady models with experimentally fitted parameters, through tailored computational model such as one proposed in the thesis, to conventional computationally expensive volume-discretizing methods.

Proposed model could be improved by considering:

- Reducing computational time of the proposed method by parallelization of appropriate parts of the algorithm, such as collocation boundary element method.

- Improving accuracy of the computational model in certain use cases by introducing vortex dissipation. This may be important for the cases in which vortices evolve near flapping wings for long time, introducing inaccurately large influence on the wings, by the "old" vortices that would have been dissipated in nature due to fluid viscosity.

- Different methods for modeling fluid viscosity effects, such as unsteady vortex lattice method or DUST [89] - a recently introduced particles wake approach.

- Implementation and testing of proposed computational model within design optimization and optimal control loops.

Bibliography

[1] C. P. Ellington, C. van den Berg, A. P. Willmott, and A. L. R. Thomas, "Leading-edge vortices in insect flight," *Nature*, vol. 384, no. 6610, pp. 626–630, 1996.

[2] A. Banazadeh and N. Taymourtash, "Adaptive attitude and position control of an insect-like flapping wing air vehicle," *Nonlinear Dynamics*, vol. 85, no. 1, pp. 47–66, 2016.

[3] N. Phillips, K. Knowles, and R. J. Bomphrey, "Petiolate wings: effects on the leading-edge vortex in flapping flight," *Interface Focus*, vol. 7, no. 1, 2017.

[4] M. R. A. Nabawy and W. J. Crowther, "The role of the leading edge vortex in lift augmentation of steadily revolving wings: a change in perspective," *Journal of The Royal Society Interface*, vol. 14, no. 132, 2017.

[5] Z.-y. Liang, L. Wei, J.-y. Lu, and X.-h. Qin, "Numerical simulation of a two-dimensional flapping wing in advanced mode," *Journal of Hydrodynamics, Ser. B*, vol. 29, no. 6, pp. 1076–1080, 2017.

[6] S. Deng, M. Percin, B. W. van Oudheusden, H. Bijl, B. Remes, and T. Xiao, "Numerical Simulation of a Flexible X-Wing Flapping-Wing Micro Air Vehicle," *AIAA Journal*, vol. 55, no. 7, pp. 2295–2306, 2017.

[7] L. Liu, H. Li, H. Ang, and T. Xiao, "Numerical investigation of flexible flapping wings using computational fluid dynamics/computational structural dynamics method," *Proceedings of the Institution of Mechanical Engineers, Part G: Journal of Aerospace Engineering*, vol. 232, no. 1, pp. 85–95, 2018.

[8] J. Tran, H. Gao, J. Sirohi, and M. Wei, "Reduced-order methodology for prediction of loads generated by a flexible flapping wing," *International Journal of Micro Air Vehicles*, vol. 10, no. 1, pp. 31–41, 2018.

[9] J. Feaster, F. Battaglia, and J. Bayandor, "A computational study on the influence of insect wing geometry on bee flight mechanics," *Biology Open*, vol. 6, no. 12, pp. 1784–1795, 2017.

[10] L. Liu and M. Sun, "The added mass forces in insect flapping wings," *Journal of Theoretical Biology*, vol. 437, pp. 45–50, 2018.

[11] T. Lambert, N. Abdul Razak, and G. Dimitriadis, "Vortex Lattice Simulations of Attached and Separated Flows around Flapping Wings," *Aerospace*, vol. 4, no. 2, p. 22, 2017.

[12] A. T. Nguyen, J.-K. Kim, J.-S. Han, and J.-H. Han, "Extended Unsteady Vortex-Lattice Method for Insect Flapping Wings," *Journal of Aircraft*, vol. 53, no. 6, pp. 1709–1718, 2016.

[13] B. A. Roccia, S. Preidikman, and B. Balachandran, "Computational Dynamics of Flapping Wings in Hover Flight: A Co-Simulation Strategy," *AIAA Journal*, vol. 55, no. 6, pp. 1806–1822, 2017.

[14] D. Garcia, M. Ghommem, N. Collier, B. O. N. Varga, and V. M. Calo, "PyFly: A fast, portable aerodynamics simulator," *Journal of Computational and Applied Mathematics*, vol. 344, pp. 875–903, 2018.

[15] K. Suzuki and M. Yoshino, "Numerical Simulations for Aerodynamic Performance of a Butterfly-Like Flapping Wing-Body Model with Various Wing Planforms," *Communications in Computational Physics*, vol. 23, no. 4, 2018.

[16] D. Chen, D. Kolomenskiy, and H. Liu, "Closed-form solution for the edge vortex of a revolving plate," *Journal of Fluid Mechanics*, vol. 821, pp. 200–218, 2017.

[17] P.-O. Persson, D. J. Willis, and J. Peraire, "Numerical simulation of flapping wings using a panel method and a high-order Navier–Stokes solver," *International Journal for Numerical Methods in Engineering*, vol. 89, no. 10, pp. 1296–1316, 2012.

[18] B. K. Stanford and P. S. Beran, "Analytical Sensitivity Analysis of an Unsteady Vortex-Lattice Method for Flapping-Wing Optimization," *Journal of Aircraft*, vol. 47, no. 2, pp. 647–662, 2010.

[19] M. Ghommem, M. R. Hajj, D. T. Mook, B. K. Stanford, P. S. Beran, R. D. Snyder, and L. T. Watson, "Global optimization of actively morphing flapping wings," *Journal of Fluids and Structures*, vol. 33, pp. 210–228, 2012.

[20] M. Ghommem, N. Collier, A. H. Niemi, and V. M. Calo, "On the shape optimization of flapping wings and their performance analysis," *Aerospace Science and Technology*, vol. 32, no. 1, pp. 274–292, 2014.

[21] E. C. Stewart, M. J. Patil, R. A. Canfield, and R. D. Snyder, "Aeroelastic Shape Optimization of a Flapping Wing," *Journal of Aircraft*, vol. 53, no. 3, pp. 636–650, 2016.

[22] Q. T. Truong, Q. V. Nguyen, V. T. Truong, H. C. Park, D. Y. Byun, and N. S. Goo, "A modified blade element theory for estimation of forces generated by a beetle-mimicking flapping wing system," *Bioinspiration & Biomimetics*, vol. 6, no. 3, 2011.

[23] J. Jeon, H. Cho, Y. Kim, J. Lee, D. Gong, S. Shin, and C. Kim, "Design and analysis of the link mechanism for the flapping wing MAV using flexible multi-body dynamic analysis," *International Journal of Micro Air Vehicles*, vol. 9, no. 4, pp. 253–269, 2017.

[24] J.-S. Choi and G.-J. Park, "Multidisciplinary design optimization of the flapping wing system for forward flight," *International Journal of Micro Air Vehicles*, vol. 9, no. 2, pp. 93–110, 2017.

[25] Z. Terze, V. Pandža, M. Kasalo, and D. Zlatar, "Optimized flapping wing dynamics via DMOC approach," *Nonlinear Dynamics*, vol. 103, no. 1, pp. 399–417, 2021.

[26] Z. Terze, V. Pandža, M. Kasalo, and D. Zlatar, "Discrete mechanics and optimal control optimization of flapping wing dynamics for Mars exploration," *Aerospace Science and Technology*, vol. 106, 2020.

[27] S. P. Sane and M. H. Dickinson, "The aerodynamic effects of wing rotation and a revised quasi-steady model of flapping flight," *Journal of Experimental Biology*, vol. 205, no. 8, pp. 1087–1096, 2002.

[28] S. P. Sane, "The aerodynamics of insect flight," *Journal of Experimental Biology*, vol. 206, no. 23, pp. 4191–4208, 2003.

[29] E. Kanso, J. E. Marsden, C. W. Rowley, and J. B. Melli-Huber, "Locomotion of Articulated Bodies in a Perfect Fluid," *Journal of Nonlinear Science*, vol. 15, no. 4, pp. 255–289, 2005.

[30] P. Tallapragada and S. D. Kelly, "Reduced-order modeling of propulsive vortex shedding from a free pitching hydrofoil with an internal rotor," in *2013 American Control Conference*, pp. 615–620, 2013. ISSN: 2378-5861.

[31] F. Boyer and M. Porez, "Multibody system dynamics for bio-inspired locomotion: from geometric structures to computational aspects," *Bioinspiration & Biomimetics*, vol. 10, no. 2, 2015.

[32] Y. Yongliang, T. Binggang, and M. Huiyang, "An analytic approach to theoretical modeling of highly unsteady viscous flow excited by wing flapping in small insects," *Acta Mechanica Sinica*, vol. 19, no. 6, pp. 508–516, 2003.

[33] H. Goldstein, C. Poole, and J. Safko, *Classical Mechanics*. San Francisco Munich: Pearson, 3rd edition ed., 2001.

[34] J. V. Jose and E. J. Saletan, *Classical Dynamics, A Contemporary Approach*. Cambridge: Cambridge University Press, 1st edition ed., 1998.

[35] B. F. Schutz, *Geometrical Methods of Mathematical Physics*. Cambridge: Cambridge University Press, 1st edition ed., 1980.

[36] Y. Choquet-Bruhat and C. DeWitt-Morette, *Analysis, Manifolds and Physics, Part 1: Basics*. Amsterdam ; New York : New York, N.Y: North Holland, revised edition ed., 1982.

[37] M. Artin, *Algebra*. Boston, MA: Pearson, 2nd edition ed., 2010.

[38] B. C. Hall, *Lie Groups, Lie Algebras, and Representations*. Cham, Switzerland: Springer, Cham, 2nd edition ed., 2015.

[39] J. E. Marsden and T. S. Ratiu, *Introduction to Mechanics and Symmetry: A Basic Exposition of Classical Mechanical Systems.* New York: Springer, 2nd edition ed., 1999.

[40] V. I. Arnold and B. A. Khesin, *Topological Methods in Hydrodynamics.* Berlin, Heidelberg: Springer-Verlag, 1998.

[41] Z. Terze, A. Müller, and D. Zlatar, "Lie-group integration method for constrained multibody systems in state space," *Multibody System Dynamics*, vol. 34, no. 3, pp. 275–305, 2015.

[42] J. Vankerschaver, E. Kanso, and J. E. Marsden, "The geometry and dynamics of interacting rigid bodies and point vortices," *Journal of Geometric Mechanics*, vol. 1, 2009.

[43] L. C. García-Naranjo and J. Vankerschaver, "Nonholonomic LL systems on central extensions and the hydrodynamic Chaplygin sleigh with circulation," *Journal of Geometry and Physics*, vol. 73, pp. 56 – 69, 2013.

[44] Z. Terze, V. Pandža, M. Andrić, and D. Zlatar, "Lie group dynamics of reduced multibody-fluid systems," *Mathematics and Mechanics of Complex Systems*, vol. 9, no. 2, pp. 167–177, 2021.

[45] J. Marsden, G. Misiolek, J.-P. Ortega, M. Perlmutter, and T. Ratiu, *Hamiltonian Reduction by Stages.* Berlin, Heidelberg: Springer-Verlag, 2007.

[46] A. Müller and Z. Terze, "The significance of the configuration space Lie group for the constraint satisfaction in numerical time integration of multibody systems," *Mechanism and Machine Theory*, vol. 82, pp. 173–202, 2014.

[47] H. Munthe-Kaas, "Runge-Kutta methods on Lie groups," *BIT Numerical Mathematics*, vol. 38, no. 1, pp. 92–111, 1998.

[48] P. E. Nikravesh, *Computer-Aided Analysis of Mechanical Systems.* Englewood Cliffs, N.J: Prentice Hall, 1988.

[49] E. J. Haug, *Computer Aided Kinematics and Dynamics of Mechanical Systems: Basic Methods.* Boston: Pearson College Div, 1989.

[50] W. Schiehlen, ed., *Multibody Systems Handbook.* Berlin, Heidelberg: Springer, 1990.

[51] B. Leimkuhler and S. Reich, *Simulating Hamiltonian Dynamics.* Cambridge, UK ; New York: Cambridge University Press, 1st edition ed., 2005.

[52] P. Betsch and P. Steinmann, "Constrained integration of rigid body dynamics," *Computer Methods in Applied Mechanics and Engineering*, vol. 191, no. 3, pp. 467–488, 2001.

[53] E. Hairer, C. Lubich, and G. Wanner, *Geometric Numerical Integration: Structure-Preserving Algorithms for Ordinary Differential Equations.* Heidelberg ; New York: Springer, 2nd ed. ed., 2006.

[54] A. Morawiec, ed., *Orientations and Rotations.* Berlin, Heidelberg: Springer, 2004.

[55] E. Celledoni and B. Owren, "Lie group methods for rigid body dynamics and time integration on manifolds," *Computer Methods in Applied Mechanics and Engineering*, vol. 192, no. 3, pp. 421–438, 2003.

[56] A. Iserles, H. Z. Munthe-Kaas, S. P. Nørsett, and A. Zanna, "Lie-group methods," *Acta Numerica*, vol. 9, pp. 215–365, 2000.

[57] J. Park and W.-K. Chung, "Geometric integration on Euclidean group with application to articulated multibody systems," *IEEE Transactions on Robotics*, vol. 21, no. 5, pp. 850–863, 2005. Conference Name: IEEE Transactions on Robotics.

[58] Z. Terze, A. Müller, and D. Zlatar, "An Angular Momentum and Energy Conserving Lie-Group Integration Scheme for Rigid Body Rotational Dynamics Originating From Störmer–Verlet Algorithm," *Journal of Computational and Nonlinear Dynamics*, vol. 10, Apr. 2015.

[59] N. E. Leonard, "Stability of a bottom-heavy underwater vehicle," *Automatica*, vol. 33, no. 3, pp. 331 – 346, 1997.

[60] H. Lamb, *Hydrodynamics.* Cambridge: Cambridge University Press, 6th edition ed., 1932.

[61] A. Sutradhar, G. Paulino, and L. J. Gray, *Symmetric Galerkin Boundary Element Method.* Berlin, Heidelberg: Springer-Verlag, 2008.

[62] W. A. Strauss, *Partial Differential Equations: An Introduction.* New York: Wiley, 2nd edition ed., 2007.

[63] J. N. Newman, *Marine Hydrodynamics.* Cambridge, MA, USA: MIT Press, 40th anniversary edition ed., 2018.

[64] C. E. Brennen, *Internet book on fluid dynamics.* Internet book: Dankat Publishing, 2016.

[65] J. Katz and A. Plotkin, *Low-Speed Aerodynamics.* Cambridge Aerospace Series, Cambridge University Press, 2 ed., 2001.

[66] J. D. Anderson, *Fundamentals of Aerodynamics, 6.ed.* McGraw-Hill Education, 2017.

[67] P. Hammer, A. Altman, and F. Eastep, "Validation of a Discrete Vortex Method for Low Reynolds Number Unsteady Flows," *AIAA Journal*, vol. 52, no. 3, pp. 643–649, 2014.

[68] J. Vankerschaver, E. Kanso, and J. E. Marsden, "The dynamics of a rigid body in potential flow with circulation," *Regular and Chaotic Dynamics*, vol. 15, pp. 606–629, 2010.

[69] M. H. Dickinson, F.-O. Lehmann, and S. P. Sane, "Wing Rotation and the Aerodynamic Basis of Insect Flight," *Science*, vol. 284, no. 5422, pp. 1954–1960, 1999.

[70] S. N. Fry, R. Sayaman, and M. H. Dickinson, "The aerodynamics of hovering flight in Drosophila," *Journal of Experimental Biology*, vol. 208, no. 12, pp. 2303–2318, 2005.

[71] M. Sun and J. Tang, "Lift and power requirements of hovering flight in Drosophila virilis," *Journal of Experimental Biology*, vol. 205, no. 16, pp. 2413–2427, 2002.

[72] S. P. Sane and M. H. Dickinson, "The control of flight force by a flapping wing: lift and drag production," *Journal of Experimental Biology*, vol. 204, no. 15, pp. 2607–2626, 2001.

[73] H. E. Taha, M. R. Hajj, and A. H. Nayfeh, "Flight dynamics and control of flapping-wing MAVs: a review," *Nonlinear Dynamics*, vol. 70, no. 2, pp. 907–939, 2012.

[74] G. J. Berman and Z. J. Wang, "Energy-minimizing kinematics in hovering insect flight," *Journal of Fluid Mechanics*, vol. 582, pp. 153–168, 2007.

[75] D. D. Chin and D. Lentink, "Flapping wing aerodynamics: from insects to vertebrates," *Journal of Experimental Biology*, vol. 219, no. 7, pp. 920–932, 2016.

[76] D. Lentink and M. H. Dickinson, "Rotational accelerations stabilize leading edge vortices on revolving fly wings," *Journal of Experimental Biology*, vol. 212, no. 16, pp. 2705–2719, 2009.

[77] M. H. Dickinson and K. G. Gotz, "Unstedy aerodynamic performance of model wings at low Reynolds numbers," *Journal of Experimental Biology*, vol. 174, no. 1, pp. 45–64, 1993.

[78] F.-O. Lehmann, "The mechanisms of lift enhancement in insect flight," *Naturwissenschaften*, vol. 91, no. 3, pp. 101–122, 2004.

[79] J. M. Birch and M. H. Dickinson, "The influence of wing–wake interactions on the production of aerodynamic forces in flapping flight," *Journal of Experimental Biology*, vol. 206, no. 13, pp. 2257–2272, 2003.

[80] T. Weis-Fogh, "Quick Estimates of Flight Fitness in Hovering Animals, Including Novel Mechanisms for Lift Production," *Journal of Experimental Biology*, vol. 59, no. 1, pp. 169–230, 1973.

[81] F.-O. Lehmann, S. P. Sane, and M. Dickinson, "The aerodynamic effects of wing–wing interaction in flapping insect wings," *Journal of Experimental Biology*, vol. 208, no. 16, pp. 3075–3092, 2005.

[82] D. Doman, M. Oppenheimer, and D. Sigthorsson, "Dynamics and Control of a Minimally Actuated Biomimetic Vehicle: Part I - Aerodynamic Model," in *AIAA Guidance, Navigation, and Control Conference*, Guidance, Navigation, and Control and Co-located Conferences, 2009.

[83] H. Liu, H. Aono, and H. Tanaka, "Bioinspired Air Vehicles Designed for Mars Exploration," *Acta Futura*, no. 06, pp. 81–95, 2013.

[84] R. Shrestha, M. Benedict, V. Hrishikeshavan, and I. Chopra, "Hover Performance of a Small-Scale Helicopter Rotor for Flying on Mars," *Journal of Aircraft*, vol. 53, no. 4, pp. 1160–1167, 2016.

[85] A. Witze, "Lift off! First flight on Mars launches new way to explore worlds," *Nature*, vol. 592, no. 7856, pp. 668–669, 2021.

[86] L. Zheng, T. Hedrick, and R. Mittal, "A comparative study of the hovering efficiency of flapping and revolving wings," *Bioinspiration & Biomimetics*, vol. 8, no. 3, 2013.

[87] M. E. Dillon and R. Dudley, "Surpassing Mt. Everest: extreme flight performance of alpine bumble-bees," *Biology Letters*, vol. 10, no. 2, 2014.

[88] J. E. Bluman, J. A. Pohly, M. K. Sridhar, C.-k. Kang, D. B. Landrum, F. Fahimi, and H. Aono, "Achieving bioinspired flapping wing hovering flight solutions on Mars via wing scaling," *Bioinspiration & Biomimetics*, vol. 13, no. 4, 2018.

[89] M. Tugnoli, D. Montagnani, M. Syal, G. Droandi, and A. Zanotti, "Mid-fidelity approach to aerodynamic simulations of unconventional VTOL aircraft configurations," *Aerospace Science and Technology*, vol. 115, 2021.

Curriculum Vitae

Viktor Pandža was born in Split on 18 December 1991. In 2010 he enrolled at the Faculty of Mechanical Engineering and Naval Architecture where he completed both undergraduate and graduate studies with highest honor achieving cummulative grade point average 5.0. He received numerous awards including Dean's and Rector's awards, two faculty medals, two Davorin Bazjanac awards and INETEC Award. After graduation, he started working as a Research Assistant in the research group at Chair of Flight Vehicle Dynamics, Faculty of Mechanical Engineering and Naval Architecture. His research interests are focused on multibody system dynamics including development and implementation of computational models for complex mechanical systems. He published five articles in leading international scientific journals (listed below) as well as a number of publications in scientific conference proceedings.

MOST RELEVANT PUBLICATIONS

1. Z. Terze, V. Pandža, M. Andrić, D. Zlatar, "Lie group dynamics of reduced multibody-fluid systems," *Mathematics and Mechanics of Complex Systems*, vol. 9, no. 2, 2021.

2. Z. Terze, V. Pandža, M. Kasalo, D. Zlatar, "Optimized flapping wing dynamics via DMOC approach," *Nonlinear Dynamics*, vol. 103, no. 1, 2021.

3. Z. Terze, V. Pandža, M. Kasalo, D. Zlatar, "Discrete mechanics and optimal control optimization of flapping wing dynamics for Mars exploration," *Aerospace Science and Technology*, vol. 106, 2020.

4. Z. Terze, D. Zlatar, V. Pandža, "Aircraft attitude reconstruction via novel quaternion-integration procedure," *Aerospace Science and Technology*, vol. 97, 2020.

5. Z. Terze, D. Zlatar, M. Vrdoljak, V. Pandža, "Lie Group Forward Dynamics of Fixed-Wing Aircraft With Singularity-Free Attitude Reconstruction on SO (3)," *Journal of Computational and Nonlinear Dynamics*, vol. 12, no. 2, 2017.